

Μεταπτυχιακή Διατριβή

**ΙΟΝΤΙΚΗ ΕΜΦΥΤΕΥΣΗ ΜΕΓΑΛΗΣ ΡΟΗΣ-ΧΑΜΗΛΗΣ
ΕΝΕΡΓΕΙΑΣ ΜΕ ΧΡΗΣΗ ΠΛΑΣΜΑΤΟΣ ΑΠΟΔΟΜΗΣΗΣ ΜΕ
LASER**

Μαρία Σπυριδάκη

Επιβλέπων Καθηγητής
Παναγιώτης Τζανετάκης

Τμήμα Φυσικής, Πανεπιστήμιο Κρήτης
Μεταπτυχιακό Πρόγραμμα Μικροηλεκτρονικής-Οπτοηλεκτρονικής

Master Thesis

**LASER ABLATION PLASMAS AS A SOURCE OF IONS FOR LOW
ENERGY-HIGH FLUX IMPLANTATION**

Maria Spiridaki

Supervisor

Panagiotis Tzanetakis

Physics Department University of Crete
Graduate Program of Microelectronics-Optoelectronics

Ευχαριστίες

Θα ήθελα να ευχαριστήσω θερμά τον επιβλέποντα καθηγητή κ. Παναγιώτη Τζανετάκη για την πολύτιμη βοήθεια και καθοδήγηση του καθ'όλη τη διάρκεια της εργασίας αυτής, καθώς επίσης και για τις πολύ επικοδομητικές και ενδιαφέρουσες συζητήσεις που είχαμε από την ξεκίνημα αυτής της εργασίας.

Τα πείραματα πραγματοποιήθηκαν στα εργαστήρια της ομάδας Laser του Ινστιτούτου Ηλεκτρονικής Δομής και Λέιζερ (Ι.Η.Δ.Λ.) του Ι.Τ.Ε. Ιδιαίτερα θα ήθελα να ευχαριστήσω την Δρ. Ιωάννα Ζεργιώτη για τη βοήθεια και το ενδιαφέρον που έδειξε. Ακόμα για όλη τη βοήθεια που μου προσέφερε θα ήθελα να ευχαριστήσω τον Αποστόλη Εγγλέζη.

Ακόμα ευχαριστώ πολύ τους Δρ. Μανόλη Σπανάκη και Δρ. Μανόλη Στρατάκη για όλη τους τη βοήθεια και τη στήριξη. Επίσης τον καθηγητή κ. Γιάννη Φραγκιαδάκη τον ευχαριστώ για τη βοήθεια και το ενδιαφέρον του.

Σε θέματα οπτικής ιόντων σημαντική υπήρξε η βοήθεια του καθηγητή κ. Θεόδωρου Τζούρου καθώς και του Δρ. Μανόλη Μπενή. Και τους δύο τους ευχαριστώ πολύ.

Θα ήθελα ακόμα να ευχαριστήσω την ομάδα Μικροηλεκτρονικής του Ι.Η.Δ.Λ. και ιδιαίτερα την ομάδα Processing για τη βοήθεια στις μετρήσεις προφίλομετρίας.

Τέλος θα ήθελα να ευχαριστήσω θερμά τον Αργύρη Κασσωτάκη και το Μάκη Κουτάντο για την κατασκευή όλων των πειραματικών διατάξεων που χρησιμοποιήθηκαν σε αυτή την εργασία.

Contents

Ευχαριστίες	i
Contents	iii
Summary	v
Introduction.....	1
Chapter 1: Pulsed Laser Ablation	
1.1 The laser ablation process	3
1.2 Material removal	4
1.3 Laser-Vapor Interaction	6
1.4 Plasma expansion.....	8
1.5 Kinetic energies of the ejected species	11
1.6 Electron Temperature.....	12
1.7 Ionization fraction.....	14
Chapter 2: Basic Plasma Properties	
2.1 The Saha equation.....	15
2.2 Temperature	16
2.3 Debye Shielding.....	16
2.4 Plasma Frequency	18
2.5 Sheaths	18
2.6 Langmuir Probes.....	21
2.7 Magnetic Field	24
Chapter 3: Ion Implantation	
3.1 High Flux ion sources	29
3.2 Laser Ion Source	31
3.3 Plasma Immersion Ion Implantation.....	32
3.4 Ablation Plasma Ion Implantation	35
Chapter 4: Plasma Guiding with Electrostatic Fields	
4.1 Outline of the operating principle	37
4.2 Experimental conditions	38
4.2.1 Back-reflection	
Experimental set-up	38
Measurements	40

VR>0, a=11mm	40
VR>0, a=5mm	43
VR<0, a=5mm	45
Discussion	48
4.2.2 45o Angle-reflection	
Experimental set-up	53
Measurements	54
Effect of secondary electron emission	54
Effect of plate voltage	58
Effect of detector voltage	59
Total positive charge	61
Discussion	63
4.2.3 10o Angle-reflection	
Experimental set-up	64
Measurements	65
Positive cone bias	66
Negative cone bias	68
Discussion	69
Chapter 5: Magnetic Plasma Guiding	
5.1 Experimental	71
Experimental set-up	71
Measurements	73
Positive cone-voltage	75
Negative cone-voltage	78
Discussion	81
Conclusion	83
Appendix	
A.1 Duoplasmatron	85
A.2 Duopigatron	86
A.3 Hot cathode electron impact ion source	86
References	89

SUMMARY

The purpose of the work presented here was the development of an ion source for low energy high flux ion implantation, based on laser ablation. Low energy stands for ion energies ranging from sub-keV up to some keV, while the term high flux refers to achieving ion doses of the order of $10^{16} \text{ ions} / \text{cm}^2$ in some minutes.

The ions are ejected from the ablated target with large initial velocities in a solid angle of the order of π sterads about the normal to the target surface. The forward velocities have a broad distribution with most probable values corresponding to kinetic energy of the order of 150 eV for ns pulse lasers, much larger than the thermal velocities in the plasma. These facts lead to a rapid expansion of the laser ablation plasma, which has dimensions loosely comparable to the distance of its central region from the target. The electron cloud follows the, so called, ion matrix of the plasma with random thermal velocities of the order of 10^6 m/sec , much larger than those of the ions because of the large mass difference. Quasi neutrality is maintained at any time and the electron cloud density closely matches that of the ion matrix. A thin sheath of less than a mm is formed at the plasma outskirts. When the plasma is not in contact with a conducting surface, the sheath contains a negative charge density (electrons) in the outer layer and a positive charge density (ion matrix depleted from electrons) in the inner space charge layer. When the plasma is in contact with electrodes a sheath forms between the neutral plasma and the electrode surface. The polarity, size, voltage drop and current densities of this anode/cathode sheath depend on many parameters discussed in detail in the following chapters.

The plasma density evolves from values characteristic of condensed matter just above the ablation spot to approximately 10^{12} cm^{-3} at a distance between 10 to 20 cm from the target. All set-ups of the experiments reported here were positioned in this distance range. The high plasma density and the resulting effective shielding of external fields leave two main alternatives in trying to separate the ions from the rest

of the ablated matter and direct them towards the implantation target with as high flux as possible. These are:

1. Extract the ions from the plasma and attempt to focus them on the implantation target while directing them away from the rectilinear and diverging trajectories of the neutrals.
2. Guide the plasma away from the neutral's path and use the, so called, plasma immersion ion implantation during which the quasi neutral plasma reaches within tens of hundreds of microns from the implantation target surface. The ions are then projected into the target by a pulse of electric field in the cathode sheath.

We have devoted a significant amount of experimental work on the first alternative and found that it may not be employed conveniently for low energy ion implantation without sacrificing a large percentage of the ions produced by laser ablation.

In the implementation of the second alternative, we have used both electric and magnetic fields to guide the plasma towards the implantation target while preventing all neutral matter in the ablation plume from reaching it. We have also attempted and succeeded to increase significantly the density of ion trajectories in the plane of the implantation target. In doing so we have taken advantage of the broad initial ion velocity distribution of laser ablation plasmas. The width of the distribution of ion arrival times at the implantation target is orders of magnitude larger than the laser pulse duration. As a consequence, the average ion flux away from the ablation target can be made as high as it is near it while the corresponding plasma densities are vastly different. The efficiency of the sources designed and tested is defined by the ratio of ions reaching the implantation target surface to the total number of ions entering the magnetic field. Our latest setup tested achieved almost 40%, neutral free, efficiency. Furthermore, we have the experience and the measurement data necessary to significantly improve further the technique we have developed by a complete redesign of the experimental setup.

INTRODUCTION

Ion implantation is routinely used for introducing specific elements into solids. The dose of ions required is moderate whenever the desired atomic concentration of the element introduced in the solid is small. This is the case for example in dopant implantation in microelectronics. The energy of the ion beam determines the depth of penetration inside the target. After entering the solid, ions lose their energy in a cascade of collisions with lattice atoms, thus producing defects in the lattice. In order to eliminate the defects created by the energetic ions, the implanted solid may be annealed at elevated temperature. Defect annealing may be achieved without appreciable diffusion of the implanted atoms.

Much larger ion doses are required when the concentration of the implanted element in the solid phase is high. A typical example is the alloying with specific elements of metallic surfaces in order to obtain a desired property like hardness, heat resistance etc. A second example is the formation by annealing of nanocrystals of an element, which is introduced in the host material by ion implantation. In order to keep the implantation time short, high flux sources are necessary for high dose implantations.

Commercial ion implanters can achieve high ion fluxes of medium and high energy ion beams. However the flux is drastically decreased when ion beams of energies in the sub-keV and keV range are required, due to space charge effects that arise when the ion velocity is decreased. On the other, low energy ion implantation finds many applications in microelectronics and optoelectronics. Due to the shallow implantation

depth, it is a promising technique for the fabrication of nanocrystals embedded in thin films, such as the gate oxides of MOS transistors and for the fabrication of single electron transistors [I.1, I.2 and references therein]. The former find applications in nanocrystals based memories [I.3], while the later are candidates as elements for low power high density integrated circuits. Another application of low energy ion implantation is in the introduction of high concentration of magnetic elements in nonmagnetic semiconductors. This opens up the possibility of using a variety of magnetic phenomena, not present in conventional nonmagnetic semiconductors, in optical and electrical devices [I.4].

There are two techniques with the potential of implanting high doses of solid-element ions, with ion currents ranging up to tens of mA's. These are the metal vacuum vapor arc (MEVVA) and the laser ablation. The former can produce ions of conducting solids, while the later can produce ions from any solid material.

In this project we employed the second technique for the development of a high-flux, low energy ion source. The ions emitted are part of a plasma plume, which is formed when the intensity of the laser beam incident on the ablation target exceeds some threshold value, which depends on the target material and the laser characteristics. There are many advantages in using laser ablation as the source of ions. First of all it is a process applicable to all materials and hence ions of any solid element can be produced. Also highly charged ions can be produced at high laser intensities. Besides the applicability to all materials, laser ablation has the advantage of being a very clean technique. This means that the composition of the plume depends only on the composition of the target and the cleanness of the vacuum chamber, since laser treatment does not introduce any impurities. Finally, the ionisation degree of the plume, which is crucial in achieving a high ion flux, can reach high values.

Our work progressed by an iterative feedback process, alternating the design of an intermediate setup based on previous measurements, aiming at the optimization of the technique. In this optimization the understanding of the properties of the plasma plume is of critical importance. For this reason we include in the first three chapters a background on laser ablation, plasma properties and ion implantation, necessary in understanding the design of the set-ups used as well as our measurements and their analysis.

The larger part of our experiments, detailed in Chapters 4 and 5, concerns the guiding of the plasma away from the neutral's path, towards the detector, where the ions are extracted from the plasma using electrostatic fields. For guiding the plasma we have used both electric and magnetic fields and succeeded to increase significantly the density of ion trajectories in the plane of the implantation target.

CHAPTER I

PULSED LASER ABLATION

1.1 The laser ablation process

Soon after their introduction it was recognized that high-powered pulsed lasers could be used for studying the interaction of intense electromagnetic fields with solid matter [1.1]. The dominant mechanisms involved in such processes and the formation of a hot plasma from the irradiated surface, when the energy density of the pulse exceeds some threshold value, were found to depend on laser parameters, such as the fluence, the wavelength, the pulse duration, the spot size as well as on the material being irradiated. The term pulsed laser ablation (PLA) has been used to describe this process. In the last two decades, pulsed laser deposition (PLD), a method, based on PLA, has been developed for the growth of thin films and has attracted much interest due to its successful application to a wide range of materials [1.2]. Recently PLA has been used for surface patterning [1.3], a process that involves writing on a surface with the use of laser pulses. This can be performed either by direct focusing of the laser light on the substrate, or with the use of a mask. Other applications of PLA, due to the formation of a hot and dense plasma, are in ablation plasma ion implantation (APII) [1.4] and for the development of laser ion sources for thermonuclear fusion and ion implantation [1.5, 1.6, 1.7]. In the following we will refer to some theoretical models and experimental findings concerning the main processes that take place during PLA.

When laser radiation is absorbed in the surface region of a solid target, the electromagnetic energy is converted into electronic excitation in the form of plasmons, unbound electrons and, in the case of insulators excitons. The electric field amplitude, E , of the electromagnetic wave is given by

$$E = \sqrt{\frac{2\Phi}{cn\epsilon_0}}$$

where Φ is the power density, c is the velocity of light, n is the refractive index and ϵ_0 is the dielectric constant in vacuum. For a material having $n = 2$ and being radiated by a pulse containing $2 \times 10^8 \text{ W/cm}^2$ power density, the electric field amplitude is $2.7 \times 10^5 \text{ V/cm}$, which is sufficient to cause dielectric breakdown and plasma formation.

The laser ablation process can be divided in three regimes [1.8]. The first regime is the interaction of the incoming laser beam with the target, resulting in evaporation of material from the target. A second regime is the interaction of the evaporated material with the laser beam, leading to plasma formation. This last regime requires that the laser fluence be above a threshold value, such that a dense vapor is formed above the target. The third regime involves an anisotropic adiabatic expansion of the plasma, giving rise to the characteristic forward-directed nature of the PLD. Actually heating of the vapor and expansion take place simultaneously [1.9], leading to a complicated interaction of the expanding plasma with the laser beam. However, treating these processes separately is equivalent to assuming that the deposited laser energy is first converted to internal energy of the target and the vapor and, subsequently, it partially decays to the kinetic energy of the ablated particles.

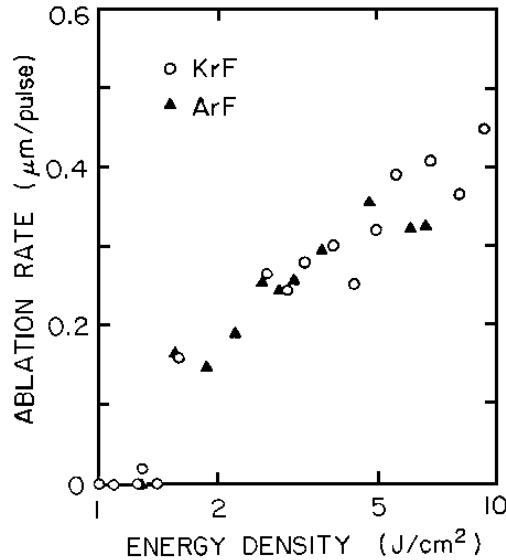
1.2 Material removal

Material removal is controlled by the rate of thermal conduction through the lattice. Given that the time for electron-lattice coupling is of the order of $\sim 10 \text{ ps}$, heat diffusion is not important when the laser pulse length is less than this value. Thus in the case of femtosecond and picosecond laser ablation, the lattice temperature can be neglected in comparison to the electron temperature (to a first approximation) and in this case evaporation is considered as a direct solid-vapor transition [1.10]. In the case where the laser pulse length is longer than this value [1.11], the excited electrons transfer their energy to the lattice within a few picoseconds and heating begins within the optical absorption depth of the material α^{-1} , α being the optical absorption

coefficient. If the thermal diffusion length, which is given by $l_T = 2\sqrt{D\tau}$, D being the thermal diffusion constant, is smaller than α^{-1} , then the material will be heated down to α^{-1} , independently of how long the pulse is. This results in a logarithmic dependence of the evaporation depth with the pulse energy and is the case involving polymers and insulators, where thermal diffusivity and absorption coefficient are small. In the opposite case, where l_T is longer than α^{-1} energy balance considerations can be used to calculate the amount of material evaporated per pulse. The resultant evaporated thickness, Δx_t , is

$$\Delta x_t = \frac{(1-R)(E - E_{th})}{(\Delta H + \rho C_p \Delta T)}$$

where R is the target reflectivity, E is the incident laser energy density, ρ , C_p , ΔT and ΔH are the mass density, heat capacity, temperature rise and the volume latent heat of the material. E_{th} is the threshold energy, which represents the minimum energy above which appreciable evaporation occurs. The above relation predicts a linear increase of the evaporated thickness with the laser fluence, which is typically observed for lower fluences [1.12]. A nonlinear behavior however can be observed, especially at high laser fluences, which is attributed to changes in material



parameters with temperature and to laser beam absorption by the vapor cloud [13]. Finally, this relation is applicable to metallic targets, which have high absorption coefficient.

In the case of silicon irradiated with KrF (248nm) and ArF (193nm) laser pulses [1.14], the vaporization rate versus the logarithm of the laser fluence is shown below in Fig. 1. 1

Fig. 1. 1: Ablation rate for Si versus the logarithm of the fluence (from [1.14]).

Above the ablation threshold of $1.45 J / cm^2$, where the vaporization rate reaches an ablation value of $0.2 \mu m$ per pulse, the ablation rate was found to increase sublinearly with increasing fluence. For copper, [1.15], using a frequency doubled Nd-YAG laser ($\lambda = 532 nm$) and $6 ns$ pulse length, the ablation rate was $6 nm$ per pulse, at $2 J / cm^2$. Finally, measured values of the ablation depth of iron ablated using a KrF excimer laser ($\tau_p = 26 ns$) reach $8 nm$ per pulse at a fluence of about $5 J / cm^2$ [1.16].

In the case of an aluminium target ablated using a frequency-tripled Nd:YAG ($\lambda = 355 nm$) with pulse duration $\tau_p = 6 ns$, theoretical model predictions [1.17] for the variation of the ablation depth with the laser fluence give depth ranging from 10^{-6} to $5 \times 10^2 nm$, when the fluence is varied from $2 - 28 J / cm^2$. It is also observed that at lower fluences (up to about $6 J / cm^2$) there is a very strong increase in the ablation depth, while at higher fluences a saturation value is reached.

1.3 Laser-Vapor Interaction

Depending on the laser fluence, the laser-solid interaction can be divided into two regimes. At low laser fluence the produced vapor behaves like an optically thin medium, permitting the rest of the laser pulse (the part that follows the vapor formation) to pass with nearly no attenuation through the vapor. At higher laser fluence, the temperature of the vapor is high enough that atomic excitation and ionization become important, and the vapor begins to absorb the laser light thus shielding the target. This leads to vapor breakdown and plasma formation.

The main mechanisms [1.18, 1.19] active in laser induced plasma formation are inverse bremsstrahlung, (IB) and photoionization, (PI). Also electron impact, (EI), excitation and ionization can be responsible for an effective enhancement of the

excited and ionized species, due to the fact that the time constants involved are typically of the order of tenths of ns, which are comparable with the pulse duration.

The IB involves the absorption of photons by free electrons, which gain energy from the laser beam during collisions with neutral and ionized atoms, thus promoting vapor ionization and excitation through electron collisions with excited and ground state neutrals. IB due to electron-neutral interaction is much smaller than that due to electron-ion interaction, however in weakly ionized vapor the former could be important. In the case of electron-ion interaction the IB absorption coefficient, α_{IB} , is [1.9]

$$\alpha_{IB} = \frac{4}{3} \left(\frac{2\pi}{3kT_e} \right)^{\frac{1}{2}} \frac{Z^2 e^6}{hcm_e^{3/2} \nu^3} N_i N_e \left[1 - e^{-\frac{h\nu}{kT_e}} \right]$$

where T_e is the electron temperature, Ze is the ion charge, ν is the laser frequency and N_i , N_e are the number densities of ions and electrons respectively. From the above expression it can be seen that IB is more efficient in the infrared and visible spectral range than in the UV.

The absorption coefficient of direct photoionization (PI), α_{PI} , of excited atoms in the vapor is [1.9](in cm^{-1})

$$\alpha_{PI} = \sum_n 2.9 \times 10^{-17} \frac{(\varepsilon_n)^{5/2}}{(h\nu)^3} N_n$$

where the summation is performed over the energy levels for which the $h\nu > \varepsilon_n$ condition holds, ε_n is the ionization energy of the excited state n and N_n is the excited state n number density (in cm^{-3}). $h\nu$ and ε_n are expressed in eV .

When the energy of the photons is comparable with the ionization energy of the excited atoms, which is typical in UV laser ablation of metals, the photoionization cross section can be of the order of $10^{-17} cm^2$. This makes very possible the photoionization of an excited atom thus increasing the ionization of the vapor. The degree of ionization can be further increased by EI. At this point, with increased ion and electron densities, the probability of photon absorption by IB can be important. However for the increased electron and ion densities to contribute to IB, the recombination time constants should be comparable or longer than the laser pulse

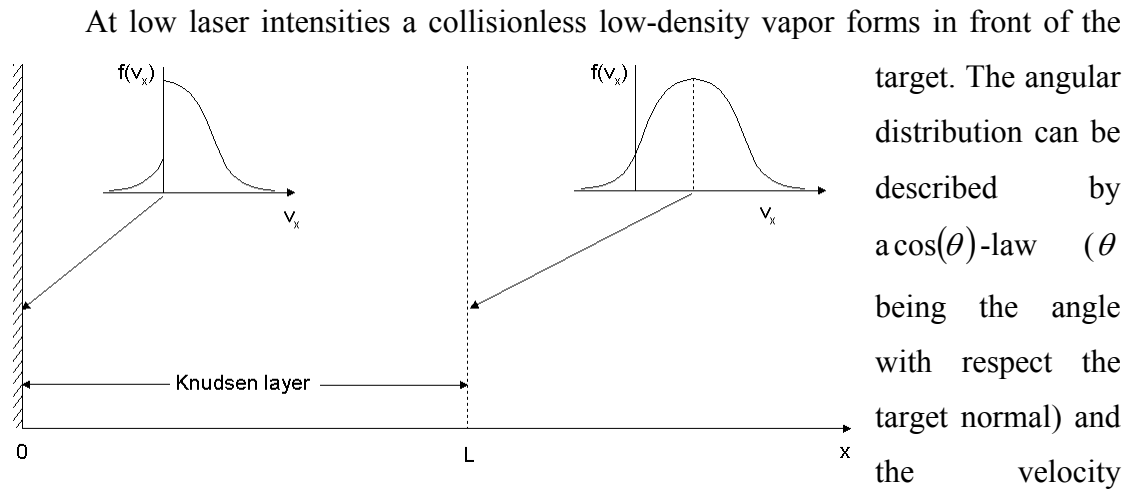
duration. The rate of recombination is estimated by considering the relaxation times of three-body recombination, (TBR), and photorecombination, (PHR), which are [1.9]

$$\tau_{TBR} = 1.1 \times 10^{26} Z^{-3} T_e^{9/2} N_e^{-2}$$

$$\tau_{PHR} = 3.7 \times 10^{12} Z^{-2} T_e^{3/4} N_e^{-1}$$

where T_e , N_e are expressed in eV and cm^{-3} respectively. In TBR recombination of electrons with ions takes place primarily by three body collisions with an electron usually acting as the third body that receives the potential energy released on capture. A neutral atom can serve as the third body however this process is of importance in extremely low ionization degrees, less than $10^{-7} - 10^{-10}$. In PHR the capture of free electrons by ions results in the emission of photons. For typical initial plasma values of electron density and temperature, TBR is important at the initial stages, until the plasma density falls below $10^{17} cm^{-3}$, where τ_{TBR} becomes of the order of $1\mu s$. This means that as the plume expands the degree of ionization remains practically unchanged. However at larger distances PHR takes place, causing a further partial re-equilibrium in the expanding plume. From the above relations it can be seen that the vapor/plasma temperature affects all the ionization and recombination mechanisms and thus the final ionization degree in the plasma, after expansion. So the rate of energy transfer from the electrons to the massive particles is important in the sense that it determines the vapor/plasma temperature. For $N_e \approx 10^{18} - 10^{20} cm^{-3}$ and $T_e \approx 1 - 5eV$ the heat transfer relaxation time is almost always less than $1ns$ [1.9]. This means that the electron and heavy particle temperatures can be assumed to be approximately equal. This is true in a time interval close and after the end of the pulse; theoretical models [1.19] indicate that during the pulse and in the case where the vapor is absorbing the laser energy, the electron temperature is higher, but there is an effective heat transfer to the massive particles. This last model predicts that, in the case of aluminium, by the end of the laser pulse ($6ns$, $350nm$, $1GW/cm^2$) the electron and the massive particle temperature reaches values of the order of $2eV$, while the electron, neutral and excited neutral number densities reach values of the order of 10^{20} , 5×10^{19} and $2 \times 10^{18} cm^{-3}$, respectively.

1.4 Plasma expansion



distribution of the expanding vapor atoms has the form of a half-range Maxwellian velocity distribution (half in the sense that the velocities along the perpendicular axis to target surface take only positive values) [1.20, 1.21].

Increasing the laser intensity results in increased vapor density near the surface, which causes collisions to take place within a layer, called the Knudsen layer [1.20, 1.21, 1.22], adjacent to the surface. The Knudsen layer is a regime that is characterized by a change of the velocity distribution of the evaporated atoms from a non-equilibrium distribution, at the surface, into a full-range Maxwellian incorporating a center-of-mass velocity and having a lower, than the surface, temperature at the edge of the layer, Fig. 1. 2.

Fig. 1. 2: The change in the velocity distribution from a non-equilibrium at the surface to a Maxwellian after passing through the Knudsen layer [1.22].

Calculations of plasma expansion include both hydrodynamical models [1.23, 1.8] and Monte Carlo simulations [1.24]. The former approach is justified when the gas density is high enough so that the number of collisions is sufficient for hydrodynamics to apply. The necessary number of collisions was found to be only 3 to 5 collisions per particle [1.25], so this approach is applicable to cases where more

than one monolayer is evaporated on a time scale of tens of ns or less. It is found [1.23] that the velocity distribution of the particles can be described by the so-called elliptical velocity distribution, used in the description of the molecular jets. In spherical coordinates this is

$$f(v, \theta, \varphi) = \frac{v^2}{c_0} e^{\left[-\frac{mv^2 \sin^2 \theta}{2kT_{xy}} - \frac{m(v \cos \theta - v_{CM})^2}{2kT_z} \right]} \quad (1.1)$$

where

$$T_{xy}^{-1} = \frac{\sin^2 \varphi}{T_x} + \frac{\cos^2 \varphi}{T_y}$$

is the temperature perpendicular to the jet axis (transversal temperature), T_z is the longitudinal temperature and v_{CM} is the center of mass velocity (also called stream velocity) and c_0 is a normalization constant. The elliptical temperatures, T_x , T_y , T_z , are related to the local temperature after equilibrium, T_0 , which is used in the general form of the Maxwell-Boltzmann distribution. In the case of a target consisting of atoms having specific heat ratio $\gamma = C_p/C_v = \frac{5}{3}$ (C_p, C_v are the specific heats at constant pressure and constant volume respectively), the elliptical temperatures are related to T_0 via $T_x + T_y + T_z = 3T_0$ [1.23]. By fitting experimental time-of-flight (TOF) distributions using the eq.(1.1), T_z was found to be larger than T_{xy} and both were independent of the mass of the ejected species [1.23]. The difference between the temperatures was explained by the fact that in the case of a circular spot the ratio T_x/T_z was found to be

$$\frac{T_x}{T_z} = \left(\frac{Z_0}{X_0} \right)^{1.2}$$

where X_0 , Z_0 are the dimensions of the gas cloud at the beginning of the expansion.

The hydrodynamic approach also shows that the expansion of the vapor formed by a laser spot having different lateral dimensions goes faster along the axis that the spot was initially shorter [1.26, 1.8]. This explains the rotation effects observed experimentally [1.11, 1.26, 1.27, 1.28].

In the presence of collisions the angular distribution of the ablated material changes to a forward peaked distribution described by

$$I(\theta) = A \cos^p(\theta)$$

(1.2)

where the exponent p can take a wide range of values, greater than unity, depending on the target material and the laser parameters. However for a given target material it is mainly affected by the laser spot size.

The forward peaked nature of the laser ablation plasmas can be measured using either film-based methods or probe-based methods [1.29]. The former involve measuring the thickness variation on a substrate placed at some distance parallel to the target, while the later measure the source angular distribution directly. This can be accomplished with an array of Langmuir probes or charge collectors that are mounted at different positions [1.30, 1.31], or with just a single one that can be moved at different positions [1.32, 1.33]. Also optical methods, as with use of a charged coupled device camera [1.27], have been used to measure the overall luminescence of the resulting plume in three dimensions as it moved away from the target.

The factors influencing the angular distribution of the injected material are the laser spot dimensions, the wavelength of the laser, the presence of ambient gas, the plume composition and the target to substrate distance [1.29]. As spot dimensions are increased the film thickness profile becomes more peaked (larger values of p). Also to more peaked distribution leads the use of lasers emitting in the ultraviolet and visible part of spectrum rather than in the infrared. On the contrary, in the presence of ambient gas collisions among the particles of the plume with the background atoms tends to broaden the angular distribution, provided that the collector is placed at distances more than some mean free paths from the target. Ions and neutrals contained in the plume are found to have different angular distributions. For instance, in the case of Y-Ba-Cu-O and polyimide ions were found to be more peaked than neutrals, while in the case of Si [1.34, 1.35], Cu [1.34], $\text{Nd}_{1.85}\text{Ce}_{0.15}\text{CuO}_4$ [1.35] ions were found to have almost isotropic expansion, in contrary to the neutrals. Film-based measurements indicate a dependence of the angular distribution on the distance of the substrate with respect to the target and specifically for C and Ge the distribution was found to becoming more peaked far from the target. It is suggested that this effect is more possible to be caused by substrate-induced perturbations of the intrinsic angular

distribution, rather than by a still-evolving distribution. Also charge collected signals were found to change from one-peaked to two-peaked by inserting in the path of the plume grid screens placed at different distances from the target and it was attributed, too, to the interaction of the particles that are scattered from the grid with the incident flow [1.36].

1.5 Kinetic energies of the ejected species

One of the reasons that support the use of PLD as a technique for the deposition of thin films as compared to other physical vapor deposition (PVD) techniques is the substantial kinetic energy of the ablated species, which was shown to improve the density and the structure of the growing film. For the neutral atoms and the small polyatomic molecules the measured kinetic energies range from a few eV [1.37] up to a few tens of eV [1.35, 1.1]. In the case of the ions present in the plume the measured energies lie in a wider range, depending on many factors such as the material, the wavelength and especially on the fluence. In the case of aluminum ablated using the second ($\lambda = 532nm$) and the third ($\lambda = 355nm$) harmonic of a Nd:YAG laser and by measuring time-of-flight (TOF) distributions of positive ions, most probable kinetic energies ranging from 10 to $200eV$, for the $532nm$, and from 6 to $100eV$, for the $355nm$, when the fluence was varied in the range $1-60J/cm^2$, were measured [1.38]. It was observed that at moderate energy densities increasing the fluence resulted in increased kinetic energy, while at higher fluences a plateau was reached. This behavior was attributed to strong absorption and partial or total reflection of the laser light by the hot plasma produced by the leading edge of the laser pulse at higher fluences.

In [1.39] kinetic energy distributions of Cu, Ge and Si, using ArF and KrF excimer lasers, for solid and liquid (Ge, Si) targets, were measured, by employing a TOF spectrometer equipped with a Faraday cup (FC) ion current detector and an electrostatic grid. Most probable kinetic energies in the range of $100-130eV$, for Cu^+ and $200-300eV$, for Cu^{2+} , were measured, in the fluence range of $3-6.6J/cm^2$. In the case of Ge ion energies between $60eV$ and $100eV$ were reported for singly charged ions and $180-260eV$ for doubly charged ones. The ion energies measured using solid targets were found, in most cases, to exceed those

obtained from liquid targets, without this being generally true. Most probable kinetic energies ranging from $65 - 80\text{eV}$ for Si^+ , in the fluence region of $2.7 - 6.3\text{J}/\text{cm}^2$ were also measured and doubly charged ions, detected using the ArF laser, were found to have about the double energy, compared to singly charged ones. From the above measurements the energy gain was found to be proportional to the ions charge and ions with different mass (Si, Ge) showed similar kinetic energy distributions. The similarity of kinetic energy distributions of ions emitted from laser induced plasmas, regardless the ions mass was also observed in [1.35]. Similar velocities were also measured in the case of copper ablated with KrF laser using a negatively biased ion probe [1.32]. For silver ablated by 355nm , 6ns laser pulses at a fluence of $0.8\text{J}/\text{cm}^2$ ion energies in the range of 40eV were measured [1.30]. A comparison of Ti ablation using two different lasers, a TEA- CO_2 , $\lambda = 10.6\mu\text{m}$, $\tau_p = 180\text{ns}$, and an excimer, $\lambda = 308\text{nm}$, $\tau_p = 50\text{ns}$, yielded higher main ion energies in the case of the TEA- CO_2 (200eV) versus the excimer (60eV), which was attributed to the more efficient IB absorption for the infrared wavelengths by the plasma [1.40].

1.6 Electron Temperature

By measuring the voltage V_T induced by excimer (KrF) laser ablation between a copper target and the ground for various load resistances, the electron temperature was calculated using the following relation [1.32]

$$i_T = i_0 e^{\frac{q(U-V_T)}{kT_e}}$$

where i_T is the target current, U is the plasma work function and i_0 is a constant. Using the above relation, which is derived for a Maxwellian electron energy distribution, T_e can be calculated from a plot of V_T against $\ln i_T$. Under a fluence of $6.7\text{J}/\text{cm}^2$ the electron temperature was found to be 7eV .

Using dye laser resonance absorption photography the initial temperature, before expansion, of an Al plume, formed by excimer laser ablation, was estimated from measurements of the velocity of the fastest particles. This velocity, v_m , is related to the temperature through the relation

$$v_m = \frac{2v_0}{(\gamma - 1)}$$

where $v_0 = \sqrt{\gamma kT/m}$ is the initial sound speed. The temperature was found to be in the range of $1 - 2eV$ for fluence equal to $2.6J/cm^2$ [1.41].

In [1.42] a Langmuir probe was used to measure the I-V characteristics of a copper plasma formed under KrF excimer laser ablation at a fluence of about $2.5J/cm^2$. Since a simple Langmuir probe theory assumes that the plasma is quiescent and homogeneous, this theory is applicable at the late stages of the laser ablation, when the fast component of the expanding plume will have bypassed the probe. By positioning the probe at 20 and 40mm from the target and restricting the analysis to times longer than $5\mu s$ the calculated electron temperature was found to be about $0.7eV$, at 20mm and $5\mu s$, and $0.4eV$ at 40mm and $5\mu s$. Also the plasma potential was calculated to be less than $1.5V$ and position and time dependent. Finally the electron density was found to become smaller than $2 \times 10^{18} m^{-3}$ for the distances and the times involved.

In [1.33] laser ablation of copper was performed using a KrF excimer laser. A Langmuir probe was also employed and the electron temperature was calculated from the natural logarithm of the peak electron current versus probe voltage. The temperature was found to be in the range of $1.5eV$ at $10.7cm$ from the target and only weakly fluence dependent for the range of $5 - 8J/cm^2$. At the same distance the peak ion density was found to be in the range of $1 - 5 \times 10^{12} ions/cm^3$ and approximately proportional to the square root of the fluence. This value was obtained from the slope of the square of the peak ion current versus the negative probe voltage.

1.7 Ionization fraction

Reported values concerning the ionization degree in PLD beams lie in a wide range. As mentioned in sec.1.2 the ionization degree is very sensitive to plasma temperature. Dieleman et. al. [1.34] performed measurements in near threshold ablation of Cu, using $30ns$ KrF laser pulses, and they reported ion fraction equal to 2×10^{-8} . Equally low ion fractions were measured in the case of Si. They determined the number of atoms removed per pulse by examination of the etched crater created at the target by the laser. In [1.43] the ion to atom ratio, α , was measured by dividing

the total number of ions reaching a FC located at the end of a TOF flight tube, to the total number of atoms entering the flight tube. The number of atoms was determined by the thickness of films deposited close to the entrance of the flight tube collimator. Ion recombination inside the flight tube could be neglected due to the low electron density there. For solid Si target α was found to 12% and for a liquid target 8%. When the ablated target volume was used to determine the total number of atoms, α was decreased to 3% for solid Si. Those values were measured using a KrF laser (25ns) at $8J/cm^2$. Even higher values are reported in [1.15] where a negatively biased grid was used to decrease the ion component arriving at a quartz crystal thickness monitor. Using a frequency doubled Nd-YAG laser (6ns) at a fluence of $1.9J/cm^2$, and applying a voltage of $-250V$ to the grid, the deposition rate was reduced to 30% of the zero-voltage value.

CHAPTER 2

BASIC PLASMA PROPERTIES

A plasma is a quasi neutral gas of charged and neutral particles that exhibit collective behavior [2.1]. Quasi neutrality ensures that the ion density, n_i , and the electron density, n_e , are almost equal (to better than one part in 10^6), thus they are referred to as the plasma density, n . If an electric potential is created somewhere in the plasma, then the electrons, which are close, will be rearranged so as to shield the potential, thus preventing it from disrupting the uniformity of the rest of the plasma. Collective behavior means that the motion of particles depends not only on local conditions, but on the state of the plasma in remote regions as well. This can be understood in the following way: when moving around, the charged particles, give rise to local concentrations of charge, thus creating electric fields; also their motion generates currents and hence magnetic fields that affect the motion of the other particles.

In the following we will refer to some basic plasma properties and to a relatively simple and widespread diagnostic tool used in plasmas, the Langmuir probe.

1.8 The Saha equation

The Saha equation predicts that the ion density in a gas at thermal equilibrium is given by

$$\frac{n_i}{n_n} \cong 2.4 \times 10^{21} \frac{T^{\frac{3}{2}}}{n_i} e^{-\frac{U_i}{kT}} \quad (2.1)$$

where n_i , n_n are ion and the neutral atom densities (in m^{-3}), T is the temperature and U_i is the first ionization potential of the atoms constituting the gas. At low

temperatures the ionization degree is very small, but when the temperature is raised to the point where U_i is a few times kT , the ionization degree rises abruptly and the gas is in a plasma state. However the ionization degree is not the factor that determines if an ionized gas can be called a plasma, as we will see in the following. Further increase in the temperature can lead to $n_n < n_i$ where the plasma becomes fully ionized.

1.9 Temperature

In a plasma there can be several temperatures at the same time. For instance, if the plasma consists of electrons and ions there can be two different temperatures, the electron temperature and the ion temperature. This happens because ions and electrons can be in their own thermal equilibrium, which is established through collisions among like-particles, but it will take some time for the two temperatures to become equal, through ion-electron collisions, and the plasma may not last that long.

1.10 Debye Shielding

If a charge, Q , is placed in a plasma the potential it creates falls off much faster than the potential the same charge would create if it was placed in vacuum. Supposing that the charge is positive, then the electrons, which are close, will be attracted by it and will move towards the charge. Thus a layer of negative charge will form around the charge, preventing its potential from penetrating into the plasma. The thickness of this shielding distance, called the Debye length, λ_D , can be derived using Poisson's equation and assuming that ions do not move, but electrons adopt a thermal equilibrium distribution with density given by

$$n_e = ne^{eV/kT_e} \quad (2.2)$$

where n , is the density far from the perturbing charge, T_e is the electron temperature and k , is the Boltzmann's constant. Poisson's equation can then be written as

$$\nabla^2 V = -\frac{\rho}{\epsilon_0} = -\frac{e}{\epsilon_0}(n_i - n_e) = -\frac{en}{\epsilon_0}(1 - e^{eV/kT_e})$$

In the region where $eV \ll kT_e$, the exponential term can be approximated as $1 + eV/kT_e$, and the above equation becomes

$$\nabla^2 V = \frac{e^2 n}{\epsilon_0 kT_e} V = \frac{1}{\lambda_D^2} V$$

where

$$\lambda_D = \left(\frac{\epsilon_0 kT_e}{e^2 n} \right)^{1/2} \quad (2.3)$$

is the Debye length. In the region close to the charge no simplification is possible because eV/kT_e may be large. However this region does not contribute much to the thickness of the shielding distance since the potential falls very rapidly there. With the boundary condition $V = 0$, when $r \rightarrow \infty$, the solution to the above equation is

$$V = \frac{Q}{4\pi\epsilon_0 r} e^{-r/\lambda_D}$$

The perturbing effects of the charge will thus penetrate into the plasma a distance of a few Debye lengths. In case the perturbation caused in the ion density was taken into account, a similar treatment would lead to a Debye length given by

$$\lambda_D = \left(\frac{\epsilon_0 kT_e T_i}{e^2 n(T_e + T_i)} \right)^{1/2}$$

T_i being the temperature of the ions.

For most laboratory plasmas the Debye length is very short; for instance for 1eV electron temperature and density of $10^{17} m^{-3}$ the Debye length is of the order of $20 \mu m$.

Inside the Debye length the quasi neutrality condition does hold, as opposed to the bulk of the plasma, the reason for this being that charges of one sign are accelerated by the potential while those of the opposite are repelled.

The idea of the Debye length provides a criterion for whether a collection of charged particles should be treated as a plasma, or as a gas of charged particles. For shielding to be meaningful, the dimensions of the system should be large compared to λ_D . Additionally, the number of particles in the Debye sphere should be large, that is if

$N_D = \frac{4}{3}\pi\lambda_D^3 n \gg 1$. If these two inequalities are satisfied and if the frequency of typical plasma oscillations is larger than the mean time between collisions with neutral atoms, then this collection corresponds to a plasma. The last condition ensures that electromagnetic forces rather than ordinary hydrodynamic forces control the particle motion.

1.11 Plasma Frequency

As already mentioned, any slight distortion of the plasma from conditions of electrical neutrality gives rise to large restoring forces. Imagine a group of electrons in a two-component plasma that are displaced slightly from their equilibrium position. Those electrons will experience a force that tends to return them to their initial position. Returning there, they will have a kinetic energy equal to the potential energy of their initial displacement, so they will continue past this position, until they reconvert their kinetic energy to potential energy. This periodic motion, known as plasma oscillation, has a characteristic frequency, the plasma frequency, which is

$$\omega_p = \left(\frac{ne^2}{\epsilon_0 m_e} \right)^{1/2} \quad (2.4)$$

where m_e is the electron mass.

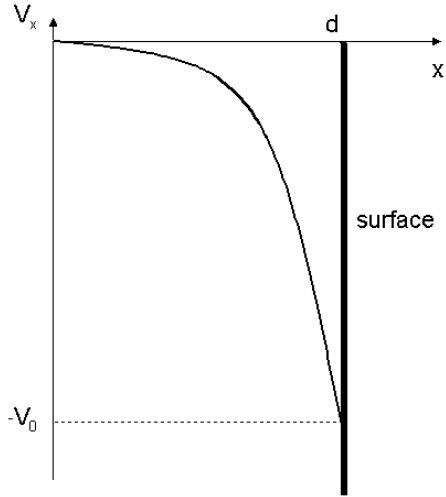
1.12 Sheaths

A situation, of great interest in which charge neutrality does not hold is in the region of contact between a plasma and a solid surface. Imagine a floating electrode immersed in a stationary plasma. Initially the electron flux to the electrode is considerably higher than the ion flux, due to the difference in electron and ion mass. Therefore the electrode quickly acquires a negative potential. Due to Debye shielding, this potential variation will be confined in layer of a few Debye lengths thick. This layer is called the sheath and its function is to create the potential barrier so that the more mobile species are confined electrostatically. The height of this barrier, called

the floating potential, is self-adjusted, so that the electron flux to the surface is balanced by the ion flux and the net current to the surface vanishes.

Consider the case that a negative voltage is applied at a surface in contact with the plasma. The surface repels electrons and attracts ions so a region of positive space charge surrounds it. The potential drop between the surface and the plasma is mostly confined in the sheath, Fig.2. 1.

To find the sheath thickness and the ion current to the surface, the ions are assumed to



enter the sheath having a drift velocity u_0 . At position x inside the sheath conservation of energy requires that

$$\frac{1}{2} m_i u_i(x)^2 = \frac{1}{2} m_i u_0^2 - eV(x) \Rightarrow u_i(x) = \left(u_0^2 - \frac{2e}{m_i} V(x) \right)^{\frac{1}{2}}$$

Fig.2. 1: Sheath formation at a negatively biased surface

In the vicinity of the sheath the rate at which ions enter the sheath equals the rate at which ions leave the plasma, so, from continuity equation, the ion density at position x , inside the sheath, can be obtained as a function of the sheath potential

$$n_i(x)u_i(x) = nu_0 \Rightarrow n_i(x) = n \frac{I}{\left(1 - \frac{2e}{m_i u_0^2} V(x)\right)^{\frac{1}{2}}}$$

where n is the ion density at the sheath edge.

The electron density everywhere, assuming that all electrons are reflected before they reach the surface, is given by eq.2.2

$$n_e(x) = ne^{eV(x)/kT_e}$$

Poisson's equation is then written as

$$\nabla^2 V(x) = -\frac{e}{\epsilon_0} (n_i(x) - n_e(x)) = -\frac{en}{\epsilon_0} \left[\left(1 - \frac{2e}{m_i u_0^2} V(x)\right)^{-\frac{1}{2}} - e^{\frac{eV(x)}{kT_e}} \right]$$

Multiplying by $\frac{dV}{dx}$ and integrating from $x = 0$ to x yields

$$\frac{1}{2} (V'^2(x) - V'^2(0)) = \frac{nm_i u_0^2}{\epsilon_0} \left[\left(1 - \frac{2e}{m_i u_0^2} V(x)\right)^{\frac{1}{2}} - 1 \right] + \frac{nkT_e}{\epsilon_0} \left[e^{\frac{eV(x)}{kT_e}} - 1 \right]$$

In the above expression $V(0)$ was taken to be equal to zero. By taking $V'(0) = 0$, i.e. that the electric field in the plasma is zero, and performing a second integration, $V(x)$ could be obtained. Independently of what the result is, the right hand side should be positive for all x . This leads to

$$\frac{nm_i u_0^2}{\epsilon_0} \left[\left(1 - \frac{2e}{m_i u_0^2} V(x)\right)^{\frac{1}{2}} - 1 \right] + \frac{nkT_e}{\epsilon_0} \left[e^{\frac{eV(x)}{kT_e}} - 1 \right] > 0$$

Near the sheath edge this expression could be approximated using the Taylor expansion, leading to

$$\frac{nm_i u_0^2}{\epsilon_0} \left(1 - \frac{e}{m_i u_0^2} V(x) - \frac{1}{2} \left(\frac{e}{m_i u_0^2} \right)^2 V^2(x) - 1 \right) + \frac{nkT_e}{\epsilon_0} \left(1 + \frac{eV(x)}{kT_e} + \frac{1}{2} \left(\frac{e}{kT_e} \right)^2 V^2(x) - 1 \right) > 0$$

$$\Rightarrow \frac{I}{kT_e} > \frac{I}{m_i u_0^2} \Rightarrow u_0 > \sqrt{\frac{kT_e}{m_i}} \quad (2.5)$$

The same inequality would be obtained if the potential at the sheath edge had not been taken equal to zero but equal to a small value V_s .

This condition is known as the Bohm condition and establishes the result that there is a minimum ion velocity the ions have when entering the sheath. For the ions to have this velocity, there must exist a finite electric field in the plasma. However the approximation mentioned above that $V'(0) = 0$ is made possible by the fact that the scale of the sheath region is much smaller than the scale of the main plasma region where ions are accelerated.

Since the electron density falls exponentially in the sheath it could be neglected. This approximation is valid for a sufficiently negative surface. With this approximation the Poisson equation near the wall is written

$$\nabla^2 V(x) = -\frac{en}{\epsilon_0} \left(\frac{m_i u_0^2}{-2eV(x)} \right)^{\frac{1}{2}}$$

Multiplying by $\frac{dV}{dx}$ and integrating from $x = 0$ to x leads to

$$V'^2(x) - V'^2(0) = \frac{4en}{\epsilon_0} \left(\frac{m_i u_0^2}{2e} \right)^{\frac{1}{2}} \left(\sqrt{-V(x)} - \sqrt{-V(0)} \right)$$

Where we take as $x = 0$ the position we start to neglect the electron density. Redefining the zero of the potential so that $V(0) = 0$ and neglecting $V'(0)$, the above equation becomes

$$V'^2(x) = \frac{4en}{\epsilon_0} \left(\frac{m_i u_0^2}{2e} \right)^{\frac{1}{2}} \sqrt{-V(x)}$$

Integrating for a second time from $x = 0$ to d

$$|V_0|^{\frac{3}{4}} = \frac{3}{4} \left[\frac{4en}{\epsilon_0} \left(\frac{m_i u_0^2}{2e} \right)^{\frac{1}{2}} \right]^{\frac{1}{2}} d$$

The ion current to the surface is

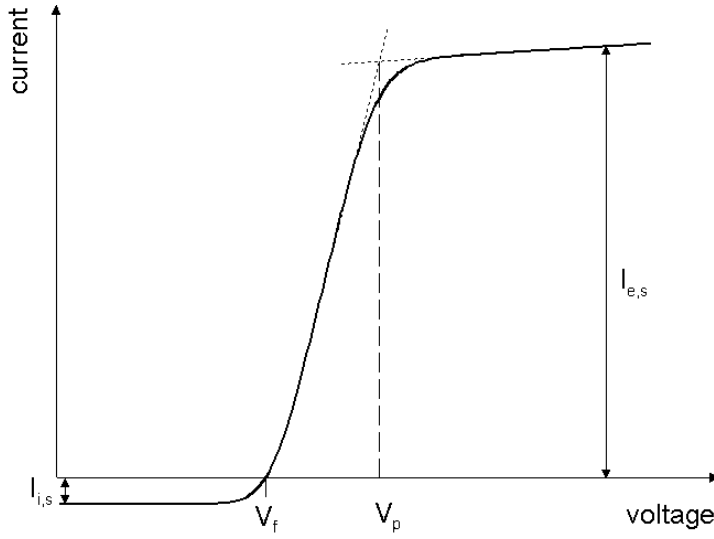
$$J = enu_0 = \frac{4}{9} \left(\frac{2e}{m_i} \right)^{\frac{1}{2}} \frac{\epsilon_0 |V_0|^{\frac{3}{2}}}{d^2} \quad (2.6)$$

The above equation is the Child-Langmuir law for space-charge limited current in a plane diode. To find the thickness, d , of the sheath this equation can be used if the current is known.

1.13 Langmuir Probes

One the simplest ways to measure some of the plasma parameters such as the electron temperature and the plasma density is with the use of a Langmuir probe immersed in the plasma [2.2]. A typical Langmuir probe has a tip, which can be a small diameter wire, or a small sphere, or disc, which is exposed to the plasma and collects ions or electrons. The probe is biased relatively to the plasma and the collected current is measured as a function of the applied voltage, yielding the current-voltage (I-V) characteristic, Fig.2. 2. The conventional current, I , is defined as positive for flow from the electrode into the plasma, thus it is equivalent as regarding the electron current as positive for flow from the plasma towards the electrode. The voltage applied to the probe is measured relative to a reference, which could be the chamber walls containing the plasma, or the anode or cathode for a discharge produced plasma.

Fig.2. 2: Typical Langmuir probe I - V characteristic.



The current collected by the probe is zero when the probe is biased at the floating potential V_f . If the probe is biased more negative than the V_f , then more ions than electrons will reach the probe, thus the current drawn by the

probe is negative. If the potential of the probe is decreased further, then all the electrons will be repelled and the current collected by the probe will reach a nearly constant value, called the ion saturation current, $I_{i,s}$. In the case where the probe is biased more positive than the floating potential, then more electrons are collected and the probe current is positive. Increasing further the potential of the probe results in increasing the current, until the probe voltage equals the plasma potential V_p . At this voltage both electrons and ions reach the probe unimpeded, but due to the fact that electrons move faster than ions, more electrons collide with the probe resulting in a positive current. If the probe voltage is sufficiently positive, then all the ions will be repelled and the current of the probe reaches a saturation value, the electron saturation current, $I_{e,s}$. In practice the current does not actually saturate either at large negative or positive voltages, but rather continues to increase slowly. This could be attributed to an increasing sheath thickness, which results in an increased collection area.

The ion saturation current [2.3] can be calculated using

$$I_{i,s} = en_s A_s u_0$$

where u_0 is the velocity at the sheath edge, $u_0 = \sqrt{\frac{kT_e}{m_i}}$, A_s is the surface of the

sheath and n_s is the ion density at the sheath edge. The ion density can be calculated

from the electron density, by setting the potential at the sheath edge, V_s , equal to the value necessary to accelerate the ions to u_0 . That is

$$V_s = -\frac{1}{2} \frac{kT_e}{e}$$

The ion density, then, is

$$n_s = ne^{-\frac{e}{kT_e} \frac{1}{2} \frac{kT_e}{e}} = ne^{-\frac{1}{2}}$$

Using the above expressions in the equation for the ion saturation current, gives

$$I_{i,s} = 0.61enA_s \sqrt{\frac{kT_e}{m_i}}$$

(2.7)

From this equation the plasma density can be obtained, provided that the electron temperature is known and that the sheath dimensions are small compared to the probe dimensions, so that the sheath surface can be taken equal to the probe surface.

The more useful part of the characteristic is near the floating potential where the current is small. By operating the probe there, large electron saturation currents that may affect the probe or the plasma are avoided.

The electron current to the probe can be taken equal to the thermal equilibrium value since more electrons are repelled. That is the random current crossing the sheath boundary reduced by the Boltzmann factor

$$I_e = \frac{1}{4} A_s n \bar{u}_e e^{\frac{eV}{kT_e}}$$

where \bar{u}_e is the mean electron speed.

The total current is given by adding the electron current to the ion current, which is assumed to be equal to the saturation value.

$$I = I_e + I_{i,s} = \frac{1}{4} A_s n \bar{u}_e e^{\frac{eV}{kT_e}} + 0.61enA_s \sqrt{\frac{kT_e}{m_i}}$$

By taking the derivative with respect to the voltage, leads to

$$\frac{dI}{dV} = \frac{e}{kT_e} (I - I_{i,s}) + \frac{dI_{i,s}}{dV}$$

the only dependence the ion saturation current has on the probe voltage is through the change in the sheath surface. This change is small when compared to $\frac{dI}{dV}$ so it can be neglected. Thus the electron temperature can be obtained from the expression

$$T_e = \frac{e}{k} \frac{(I - I_{i,s})}{\frac{dI}{dV}}$$

Then the plasma density can be calculated, using the expression for the ion saturation current eq.(2.7), and subsequently the Debye length can be deduced.

The above analysis is applicable under special conditions involving the plasma and the probe. These conditions are that the plasma is nonmoving, that the probe is nonemitting and that the probe dimensions are larger than sheath thickness, so that the sheath can be treated as having plane symmetry. Also, collisions were ignored, that means that for a spherical probe, the radius should be smaller than mean free path.

1.14 Magnetic Field

When a charged particle enters a region of constant and uniform magnetic field it will start to gyrate around the field lines. The projection of its orbit in the plane perpendicular to the magnetic field will be a circular gyration at the cyclotron frequency

$$\omega_c = \frac{|q|B}{m} \quad (2.8)$$

where q is the particle charge and with radius

$$r_L = \frac{v_{\perp}}{\omega_c} = \frac{mv_{\perp}}{|q|B} \quad (2.9)$$

which is called the Larmor radius. In the above equation v_{\perp} denotes the speed in the plane perpendicular to the magnetic field. If the particle has a component of velocity in the direction of the magnetic field its trajectory will be a helix with its axis parallel to the magnetic field and its radius equal to r_L . The center of the circle is called the guiding center.

The particle motion generates a magnetic field having an opposite direction to that externally imposed. Thus in a plasma particles tend to reduce the external magnetic field, so plasmas are diamagnetic.

In case a constant and uniform electric field is also present the equation of motion is

$$m \frac{d\vec{v}}{dt} = q(\vec{E} + \vec{v} \times \vec{B})$$

\vec{v} being the particle velocity.

In the axis parallel to the magnetic field the particle motion will be a straightforward acceleration. In the plane perpendicular to \vec{B} the orbit is a circular motion, as in the case where the electric field was absent, having also superimposed a drift of the guiding center given by

$$\vec{v}_E = \frac{\vec{E} \times \vec{B}}{B^2}$$

This drift velocity is independent of q, m and v_{\perp} which means that an electron and an ion guiding centers drift towards the same direction and with the same speed.

If instead of the electric field another force, \vec{F} , is present then the motion is the same as before with the guiding center drift given by

$$\vec{v}_F = \frac{\vec{F} \times \vec{B}}{qB^2}$$

which has opposite directions for ions and electrons if the force is independent of the particle charge.

Nonuniformities in the magnetic and the electric fields complicate the problem of obtaining expressions that describe the motion of particles. The particle's orbit is always the circular Larmor motion around the magnetic field lines plus a superimposed drift of the guiding center, which depends on the type of the inhomogeneity involved. For instance in the case that there exists a gradient in magnetic field lines density, $\vec{\nabla}B$, in the direction perpendicular to the magnetic field and assuming that the Larmor radius is much smaller than the scale length of $\vec{\nabla}B$, then the guiding center drift is given by

$$\vec{v}_{\nabla B} = \pm \frac{1}{2} v_{\perp} r_L \frac{\vec{\nabla} \times \vec{\nabla} B}{B^2}$$

where \pm stands for the sign of the charge.

Up to now we saw how external electromagnetic fields affect single particle motion. When it comes to plasma's response in such fields, where a large number of particles has to be considered the usual approach, to simplify the problem, is to treat the plasma as a fluid composed of two or more interpenetrating fluids. This approach can explain the majority of plasma phenomena. The plasma is assumed to consist of ions and electrons and that both consist of two conducting fluids, which are coupled by Maxwell's equations and through momentum transfer collisions. The charge and current densities are

$$\sigma = n_i q_i + n_e q_e$$

$$\vec{j} = n_i q_i \vec{v}_i + n_e q_e \vec{v}_e$$

where $\vec{v}_{i,e}$ is in this case the fluid velocity. The Maxwell's equations are then written as

$$\vec{\nabla} \cdot \vec{E} = \frac{1}{\epsilon_0} (n_i q_i + n_e q_e)$$

$$\vec{\nabla} \times \vec{E} = -\dot{\vec{B}}$$

$$\vec{\nabla} \cdot \vec{B} = 0$$

$$\vec{\nabla} \times \vec{B} = \mu_0 (n_i q_i \vec{v}_i + n_e q_e \vec{v}_e + \epsilon_0 \dot{\vec{E}})$$

where the vacuum equations are used, however σ and \vec{j} include all the charges and currents, both external and internal. The fluid equation of motion for the ions is

$$m_i n_i \frac{d\vec{v}_i}{dt} = q_i n_i (\vec{E} + \vec{v}_i \times \vec{B}) - \vec{\nabla} p_i - \vec{\nabla} \cdot \vec{\pi}_i + \vec{P}_{ie}$$

where p_i is the isotropic part of the stress tensor and $\vec{\pi}_i$ is the anisotropic viscosity tensor. \vec{P}_{ie} represents the friction between the two fluids and can be written in terms of the collision frequency as

$$\vec{P}_{ie} = m_i n_i (\vec{v}_i - \vec{v}_e) \nu_{ie}$$

ν_{ie} being the ion electron collision frequency. A similar equation holds for electrons.

Also the equation of continuity

$$\frac{\partial n_j}{\partial t} + \vec{\nabla} \cdot (n_j \vec{v}_j) = 0 \quad j = i, e$$

and the thermodynamic equation of state relating p_j to n_j

$$p_j = C_j n_j^{\gamma_j} \quad j = i, e$$

where γ_j is the specific heats ratio.

Solving the above equations yields the values of density, pressure and velocity (3 components) for each species and the magnetic and electric fields vectors.

When a neutral component exists, such as in partially ionized plasmas, then this fluid is coupled to ions and electrons through momentum transfer collisions.

From the fluid equation of motion it can be shown that the effect of the magnetic field is to reduce the diffusion of particles across the magnetic field. This can be shown easily in the case of weakly ionized plasma. Consider a plasma in a magnetic field. The particles will move in the parallel direction by mobility and diffusion, unaffected by the presence of the magnetic field. If there were no collisions the particles would not diffuse at all in the perpendicular direction. However in the presence of collisions the particles through successive collisions and by a random-walk process diffuse to the wall. Using the equation of fluid motion assuming an isothermal plasma ($\gamma_j = 1$) and neglecting the term $\vec{\nabla} \cdot \vec{\pi}_i$, since like-particle collisions, which do not give much rise to diffusion are contained in this term, gives

$$mn \frac{d\vec{v}_\perp}{dt} = qn(\vec{E} + \vec{v}_\perp \times \vec{B}) - kT\vec{\nabla}n + mn\nu\vec{v}_\perp$$

where collisions with neutrals are only considered and \vec{v}_\perp denotes the perpendicular velocity. Assuming that the collision frequency is large enough, so that the time derivative term is negligible and solving the system of the two equations for the transverse components of the velocity, gives

$$\vec{v}_\perp = \pm \mu_\perp \vec{E} - D_\perp \frac{\vec{\nabla}n}{n} + \frac{\vec{v}_E + \vec{v}_D}{1 + (\nu/\omega_c)^2}$$

where μ_\perp, D_\perp are the perpendicular mobility and diffusion coefficient, defined as

$$\mu_\perp = \frac{\mu}{1 + \omega_c^2/\nu^2} = \frac{|q|/m\nu}{1 + \omega_c^2/\nu^2}$$

$$D_\perp = \frac{D}{1 + \omega_c^2/\nu^2} = \frac{kT/m\nu}{1 + \omega_c^2/\nu^2}$$

and \vec{v}_E, \vec{v}_D are the $\vec{E} \times \vec{B}$ and the diamagnetic drifts. The latter comes from density gradients, to which this drift is perpendicular and the former is perpendicular to potential gradients. From the above equations it can be seen that the effect of

collisions with neutrals is to reduce these drifts and increase the diffusion and the mobility across the magnetic field. On the other increasing the magnetic field, meaning increasing the ratio ω_c/ν , tends to decrease diffusion and mobility in the perpendicular direction.

As already mentioned plasmas are diamagnetic, which means that they tend to reduce the external magnetic field in their interior. To what extent this happens is determined by the β factor, which is defined as the ratio of the particle pressure to the magnetic field pressure

$$\beta \equiv \frac{\sum nkT}{B^2/2\mu_0}$$

When β is low, lower than 10^{-3} , then the magnetic field is not reduced by the plasma. When $\beta = 1$, then the plasma generates an exactly opposite magnetic field leading thus to two regions, one with magnetic field and no plasma and one with plasma and no magnetic field.

CHAPTER 3

ION IMPLANTATION

3.1 High Flux ion sources

Ion and electron beams are being used in a range of processes for the fabrication and diagnostics of microelectronic devices and circuits. Ion sources are employed, besides ion implantation [3.1] in many other fields including particle accelerators, mass separators and mass spectrometers. Due to the wide range of applications there is a variety of ion source designs [3.2] with different properties depending on the species of the ions needed, the beam current, the optical properties of the beam, the power consumption and other factors. Here we will refer to four representative ion source designs, which are capable of generating high ion concentrations, that of the duoplasmatron, the duopigatron, the hot cathode electron impact ion source and the metal vapor vacuum arc ion source (MEVVA).

The duoplasmatron [3.3], consists of a cathode, an intermediate electrode, an anode and the extracting electrode [Appendix I]. Also an inhomogeneous magnetic field is used, which is concentrated near the anode. The ions are extracted through a small aperture in the anode. The high density at the anode creates problems at the extraction and the following ion optics, so an expansion cup is often used after the extraction electrode, to reduce the divergence angle of the extracted beam. There are many parameters that must be set to optimum values for achieving the desirable ion beam characteristics; these include the arc current, the arc voltage, the pressure of the gas, the extraction voltage. Very important are the dimensions of the anode and the intermediate electrode, the distance between them, since it affects the geometry of the magnetic field, and the elements used for their construction, both must be made partly of a magnetic material. Also cooling is required for them, due to the high power flux.

Typical values for the extracted current are $10-100mA$, for arc currents varying between 10 and $100A$, arc voltages 100 to $200V$, extracting voltages 10 to $50kV$ and maximum magnetic field 2 to $7kG$. Operating pressure is in the range of $0.5-8\cdot 10^{-2}mmHg$, off this region the discharge becomes unstable. Typical anode openings are of the order 0.5 to $1.5mm$ diameter.

To further increase the ion current some modifications can be made to the previous geometry [3.4, 3.3], leading to an ion source geometry known as the duopigatron [Appendix I]. These modifications include opening of the anode and of the extraction electrode aperture. The extraction electrode, in this case, acts as a secondary cathode and is maintained at cathode potential. Using this configuration causes the electrons to oscillate between the cathode and the anticathode increasing in this way the ionization efficiency and consequently the extracted current. Currents obtained are in the range of $300mA$ to $1A$.

An important class of ion sources makes use of a hot thermionic cathode as the electron source in an electron impact-type ion source [3.5]. Again a magnetic field is used to prevent electrons from going directly to the anode [Appendix I]. Instead they follow helical trajectories around the magnetic field lines ionizing more efficiently the gas atoms. As a result the plasma, which fills the entire chamber, is continuously supplied with electrons and ions.

By changing the configuration of the magnetic field the profile of the extracted current can be varied. For instance if a uniform plasma density is desired at the extraction end to produce a large area beam, a divergent field with higher magnetic line concentration at the cathode is needed.

For the three different types of ion sources mentioned, the ratio of the arc current to the extracted ion current and the power utilization (arc power per A of ion current) is about $150:1$ and $30kW/A$ respectively for the duoplasmatron, $20:1$ and $2kW/A$ for the duopigatron and $6:1$ and $250W/A$ for the hot cathode electron impact ion source [3.3].

The major problems associated with hot cathode ion sources are cathode's short lifetime, complicated design and power consumption. For these reasons cold cathode ion sources are also employed. The choice is always a contradiction of the requirements concerning the ion beam with respect to design difficulties and power consumption.

When ion beams of solid-state elements are required, the source's design has to be modified and two problems have to be coped with. These involve the vaporization of the element at an appropriate pressure and the ionization of the vapor. The vaporization of the elements can be done either with an evaporator oven, mounted inside or outside the ionization chamber, or with electron or ion bombardment of the solid. Many designs utilizing different techniques of vaporization and ionization and applicable to different requirements involving ion species, ion current, design complication and power consumption have been developed [3.2].

Another type ion source for the production of high current ion beams from any solid electrically conducting material was developed by Brown et. al. [3.6]. In this source an arc is established between a cathode and an anode. Typically the arc current is of a few hundred amperes and the arc drop is $15 - 100V$. The basic characteristic of this type of discharge is the formation of "cathode spots", which are minute regions of intense current concentration, on the cathode surface where the cathode material is vaporized and ionized. Thus a dense plasma of cathode material is formed which plumes away from the cathode towards the anode. From a central hole located in the anode a portion of the plasma passes into a field-free region and the ion component is extracted using a system of multiaperture extraction grids. The addition of a magnetic field near the anode increases the fraction of the plasma through the anode hole. Total beam currents up to $1A$ were reported for lithium, uranium and tantalum, but also extracted beams of boron, carbon, aluminum, silicon, titanium, iron, niobium, lanthanum, gold and lead were extracted.

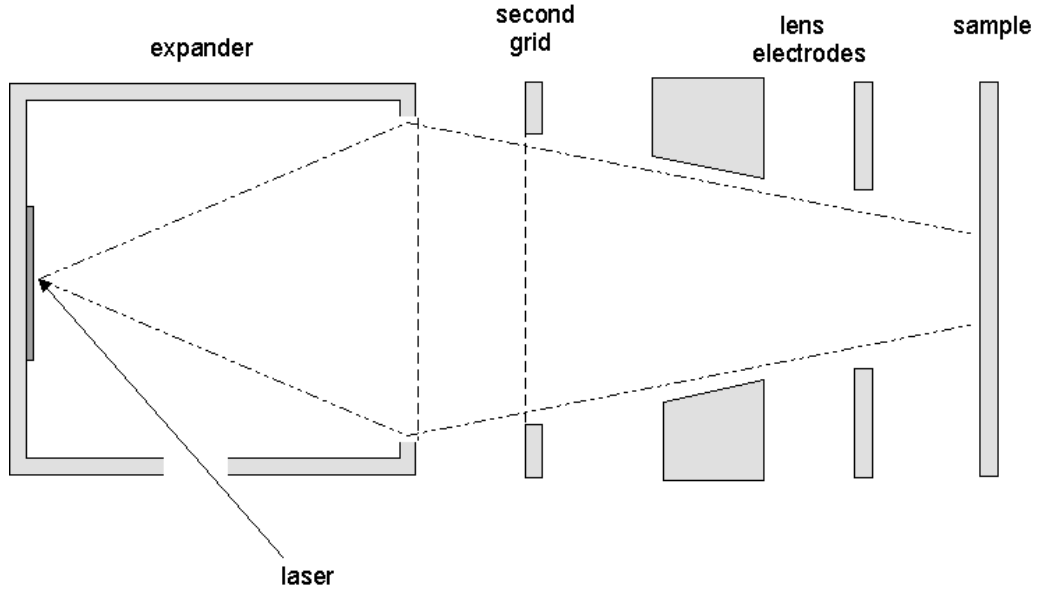
As mentioned before ions are extracted by applying a high voltage at the extracting electrode. Therefore ions have a relatively large energy (in the keV range). If ion beams of low energy are required then an electrostatic lens system to decrease the ion energy should be employed [3.7].

3.2 Laser Ion Source

A different type of ion source using the ions from laser ablation plasma is shown below, Fig.3. 1, [3.8]. This ion source is capable of operating in two different modes, providing either a fairly uniform large area beam (beam homogeneity within 5% over

an area of 3cm^2), or a focused ion beam for high dose implantation ($10^{17}\text{cm}^{-2}\text{sec}^{-1}$).

The target is placed inside an expander kept at high potential up to 30kV. Ions



are extracted from the opposite side of the expander, which is covered with a grid and are subsequently accelerated by a second grid. When a large area beam is required the sample to be implanted can either replace the second grid [3.8], or can be placed behind it [1.7].

To achieve focusing of the beam a single lens is used. The first electrode of the lens is the flat grid, while the central electrode is kept at the same potential as the expander. For the high dose implantation mode the sample is placed after the lens.

Fig.3. 1: Laser ion source for ion implantation employing two modes of operation, large area beam or focused beam.

In the case of the large area beam, with the sample replacing the second grid and at 100Hz laser repetition frequency, ion current pulses having duration of $\sim 5\mu\text{sec}$ and average current of $5\mu\text{A}$, for 20mm beam diameter were measured. In the other case, with the sample placed behind the second grid the time-average ion current was measured 90-100 μA . In the focused ion beam mode, at 25kV accelerating voltage, the ion beam spot diameter was 0.8mm and the maximum current was a few A/cm^2 .

With this apparatus however simultaneous ion implantation and neutral atom deposition cannot be avoided.

3.3 Plasma Immersion Ion Implantation

Plasma source ion implantation (PSII) [3.9], or plasma immersion ion implantation (PIII) [3.10], is a surface modification technique designed to provide inexpensive, high-throughput ion implantation. In PIII the specimens are surrounded by a plasma and are pulse biased to high negative voltage resulting in a sheath formation around the samples, ion's acceleration through the sheath and consequent implantation into the target. Because of the absence of ion optics and mass selection, PIII can achieve very high doses (as high as $10^{16} \text{ cm}^{-2} \text{ s}^{-1}$). It is also a non line-of-sight process, as opposed to conventional beamline implantation. This means that non-planar targets can be implanted more effectively since the electric field, which accelerates the ions, is normal to the target's surface thus eliminating the incidence of ions at glancing angles and the subsequent sputtering of previously implanted material. Some other advantages include the instrumentation, which is relatively simple and inexpensive, and the range of the implantation energy that can vary from 10 to 10^5 eV . A disadvantage of this process is that ion energy and species cannot be selected as in magnetically filtered beamline implantation since the negative voltage attracts all positively charged ions present.

As was already mentioned, the target to be implanted is immersed in plasma and a large negative voltage pulse is applied to it. On the timescale of the inverse electron plasma frequency, ω_{pe}^{-1} , the electrons are pushed away, leaving behind a region containing only ions, Fig.3. 2b. Ions due to heavier mass are motionless on this time scale. This region of ion space charge is known as the ion matrix sheath. On the longer timescale of the inverse ion plasma frequency, ω_{pi}^{-1} , the ions are accelerated towards the target, where they are implanted. The loss of ions from the sheath means that the target's voltage is not shielded and the plasma electrons will recede even further, Fig.3. 2c, causing the sheath edge to expand. This sheath expansion causes the exposure of more ions, which are then implanted. Finally the electron and ion profiles relax to establish a steady-state Child-Langmuir sheath.

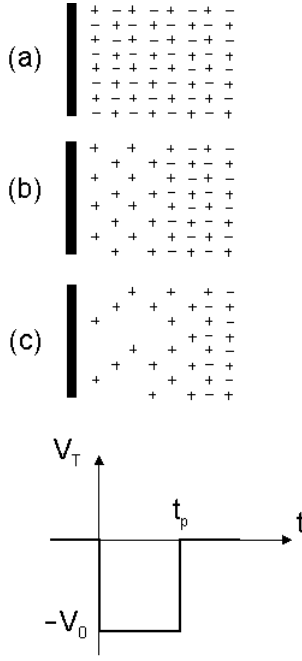


Fig.3. 2: Plasma immersion ion implantation. (a) Neutral plasma before the voltage is applied, (b) electron's recession immediately (ω_{pe}^{-1}) after the application of the voltage (c) sheath's expansion.

By solving the Poisson's equation expressions for the sheath thickness, s_0 , and the potential profile for planar, cylindrical

and spherical targets can be derived [3.11]. The boundary conditions for solving the Poisson's equation are that the potential at the electrode position, $x = 0$, is equal to $-V_0$ and that the electric field and the potential vanish at the sheath edge $x = s_0$. Assuming that the electron's motion is instantaneous, the ion density is uniform and does not change during the sheath formation, the applied voltage $V_0 \gg kT_e/e$, where T_e is the electron temperature and that the applied pulse has no rise and fall time the following results are obtained for a planar target

$$s_0 = \sqrt{\frac{2\varepsilon_0 V_0}{en_i}}$$

(3.1)

$$V(x) = -\frac{en_i}{2\varepsilon_0}(x^2 - 2s_0x) - V_0$$

To determine the time-varying ion current, the total dose and the energy distribution of the implanted ions, analytical models have been developed [3.12, 3.13]. These models assume that the ion flow is collisionless, the electron motion inertialess, that during and after matrix sheath formation a quasistatic Child law sheath forms and that during the motion of an ion across the sheath the only change in the electric field is due to the velocity of the moving sheath. The expanding sheath thickness is obtained to be

$$s(t) = s_0 \left(\frac{2}{3} \omega_{pi} t + 1 \right)^{1/3}$$

where ω_{pi} is the ion plasma frequency. And the total ion current [3.10]

$$j_i(t) = \frac{4}{9} \epsilon_0 \sqrt{\frac{2e}{m}} V_0^{3/2} \left(\frac{I}{s(t)^2} + \frac{s_0^2}{s(t)^4} \right)$$

The ion dose per pulse is obtained by integrating the ion current over the pulse width

$$d = \int_0^{t_p} j_i(t) dt$$

Due to secondary electron emission during the implantation of ions, the total current density j_t is the sum of the two terms (ion and secondary electron current density)

$$j_t = (1 + \gamma_i) j_i$$

3.4 Ablation Plasma Ion Implantation

A modification of PIII is ablation plasma ion implantation (APII) [3.14]. In APII a laser ablates a solid target and the generated plasma plume is the source of ions. APII has the advantages of PIII with the difference that there is no need for any gaseous precursor to be ionized to serve as the source of ions. Moreover any solid material may be ablated to form the ion source.

A one-dimensional theory describing the implantation of ions from the ion matrix sheath in an ablation plasma plume that is approaching a negatively biased substrate has been developed [3.14]. This model borrows the main features of PIII meaning that electrons are ignored and ion current density is evaluated with the electric field having the initial profile that developed during the ion matrix sheath formation.

APII was used for iron implantation into silicon, by Qi et.al., [1.4], using high voltage pulses of $10kV$ and pulse duration of $10\mu s$. TEM data revealed the presence of a damage layer, which is believed to be the result of collisional cascades, at $7.6nm$ below the original surface of silicon. Iron implantation was also demonstrated with measurements from x-ray photoelectron spectroscopy. However with this technique neutral atoms, contained in the plasma plume, are also deposited on the substrate. This constitutes a problem if deposition of an extra layer is not desirable.

CHAPTER 4

PLASMA GUIDING WITH ELECTROSTATIC FIELDS

4.1 Outline of the operating principle

All setups described in the present and in the following chapter concern the second of the two main alternatives mentioned in the introduction, namely the guiding of the plasma in a way enabling both charged-neutral separation and high average ion fluxes at the implantation target.

The basic operating principle of the sources that we have developed and tested is referred to in the following as plasma funneling. The fast moving LA plasma is forced into the entrance of a metallic “funnel”. If ions can be reflected at surface of the funnel instead of falling onto it, they will reach the narrow exit opening of the funnel and their average flux will increase inversely proportional to the square of the cone diameter.

In the description of the experiments we use in the following a Cartesian axis system with its origin on the laser spot on the ablation target and axis z perpendicular to the targets’ surface.

We have considered two possibilities of preventing neutral matter (neutral atoms, small clusters of atoms and molten droplets originating from the ablation crater of the target) from reaching the exit orifice of the funnel. The first is tilting the axis of symmetry of the funnel with respect to the z -axis in a way to avoid optical contact between the target and the exit orifice. The second is blocking

optical contact between the laser spot and the exit orifice of the funnel with the help of a small diameter disk inserted near the entrance orifice and centered on the axis of symmetry of the cone.

These options are further discussed in the following.

The set-ups we have used in our experiments fall into two categories.

1. Auxiliary, test set-ups intended for the quantitative measurement of the relevant laser ablation plasma properties. These are: (a) the back-reflection set-up, described in section 4.2.1 and (b) the 45° angle-reflection set-up, which is presented in section 4.2.2.
2. Complete source designs of variable complexity.

4.2 Experimental conditions

Our experiments were performed in a vacuum chamber pumped by a mechanical and a diffusion pump. Polycrystalline silicon (99% purity) was used as the target material and was placed on a rotating holder in order to avoid making deep craters on the target.

The laser used was an excimer XeCl ($\lambda = 308nm$) laser with pulse duration $32nsec$ operating at a frequency of $2Hz$. The laser beam was focused on the target using a $50cm$ focal length lens placed outside the vacuum chamber, in such a way that the angle of incidence with respect to the target normal was 26° and the laser spot on the target was $3.8mm \times 0.8mm$ measured after one pulse.

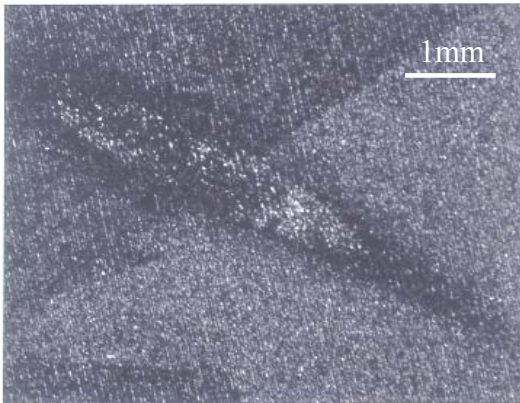


Fig. 4. 1: Laser spot on the target after 1 pulse.

4.2.1 Back-reflection

Experimental set-up

We have used the set-up depicted in Fig. 4. 2 in order to check how efficiently the ions can be separated from the rest of the plasma using electrostatic fields and at the same time measure some of the plasma properties. This set-up consists of a reflector and a detector. When the plume arrives at the reflector a part of it is reflected and a fraction of it reaches the detector. By changing the reflector voltage the reflector and detector current and the arrival time of the charges at the detector are expected to change.

The reflector was placed above the target, at 11cm . It consists of a circular plate, held at a positive or negative potential depending on whether ions or electrons are to be repelled, inside a cup kept at ground potential. The entrance of the cup, in front of the plate, is covered with a grid of 40% transparency. The entrance diameter was 68mm , while the distance, a , between the grid and the plate, could be adjusted from 1 to 11mm . The ability to change a , provided the additional option of exploring the effect of the electric field on the reflection of the charged species. The detector was mounted at the same height as the ablation target. The detector was identical to the reflector except for the fixed distance between the plate and the grid at 5mm . To suppress secondary electron emission, when heavy particles impinge on the plate, the detector plate was kept at $+27\text{V}$ with respect to the cup, which was at ground potential. The distance between the center of the detector and the laser spot was about 95mm .

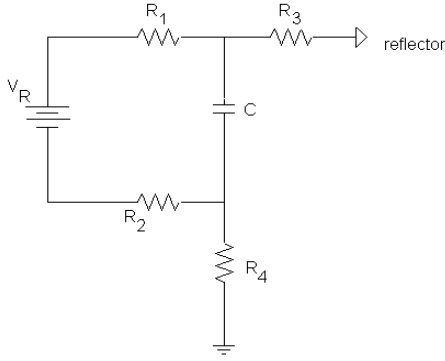
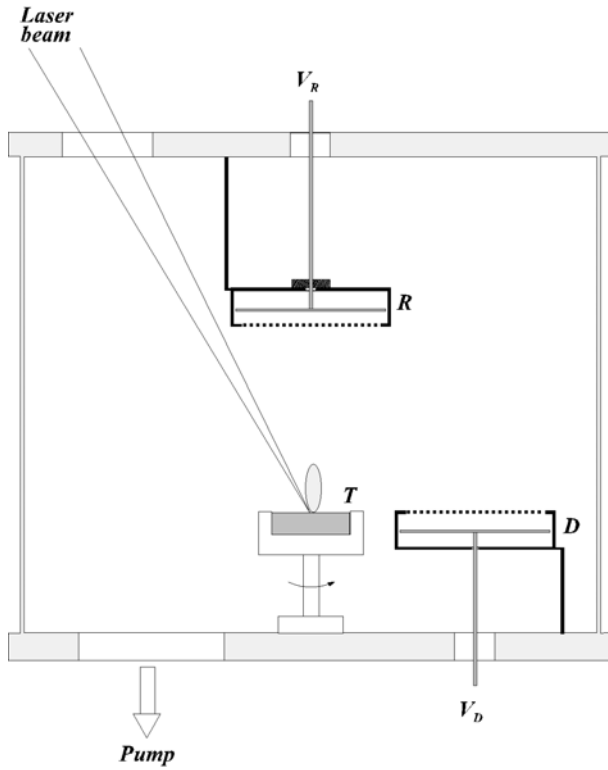


Fig. 4. 2: The experimental setup described in text. R is the reflector, D the detector and T the target.

To apply the voltage V_R on the reflector plate and to measure the collected current the following circuit was used. All current measurements were performed with sense resistors. The values of the resistors were



chosen so that the voltage drop developed on them, when the plume was present, was much lower than the bias voltage, but high enough to be measured with a 1:10 oscilloscope probe. The voltage drop on R_3 was differentially measured, while for the corresponding voltage drop on R_4 single ended measurement was performed. We verified that equal currents were measured on both resistors and for this reason, single ended measurements were performed thereafter.

Fig. 4. 3: Reflector bias and current measurement circuit. $R_1=500\Omega$, $R_2=1000\Omega$, $R_3=R_4=1\Omega$, $C=150\mu F$.

A capacitor with low equivalent series resistance (ESR) was used in order to stabilize the voltage during the arrival of the plume. To eliminate the effect the fluctuations of the laser pulse energy had on the measured waveforms, a sufficient number of voltage waveforms, usually fifty, were averaged at the oscilloscope and the resulting waveform was stored.

At the detector three batteries of $9V$ were used in series with a $1k\Omega$ resistor to the ground, for the current measurement. Again, the waveforms measured were the average of a sufficient number of successive waveforms.

Measurements

$$V_R > 0, a = 11mm$$

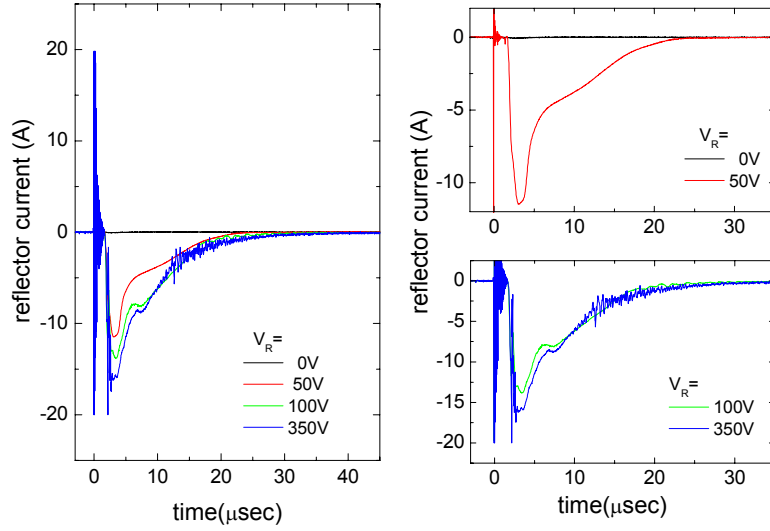
Having the distance a set at $11mm$, the reflector and the corresponding detector signals were measured for different voltages V_R . The different signals are shown below in Fig. 4. 4 and Fig. 4. 5, for the reflector and the detector, respectively. These signals were obtained under working pressure of $2.5 \times 10^{-5} mbar$ and at a fluence of $4.8 J / cm^2$.

The reflector signal is negative since it collects electrons, whereas the detector, which collects a part of the reflected ions, exhibits a positive signal. At $V_R \cong 0V$ the reflector's signal is zero, indicating that the plasma has total charge close zero, as expected. At small negative values of V_R the signal shows a strong increase with the voltage, while at higher voltages it continues increasing, however at a smaller rate. At the same time a second peak centered around $8\mu sec$ is distinguished. When the voltage is raised above $250V$ the possibility of discharge formation is increased and

that was the reason why the last trace of Fig. 4. 4 is the average of only 3 pulses, in contrary to the others, which contain 50 waveforms averaged (W.A.).

Fig. 4. 4: The graph on the left shows the reflector signals measured for different values of V_R . The graphs on the right are magnifications of the graph on the left showing the region of interest. a was set at 11mm. W.A.=50 for 0, 50, 100V and 3 for 350V.

The detector, on the other hand, at zero V_R , exhibits a negative signal, consisting of two peaks. The first peak, which appears at flight times less than $1\mu sec$, after the laser pulse and remains even for $V_R = 350V$ could be due to photoelectrons and secondary electrons ejected from the chamber walls. The second peak, centered at



about $2\mu sec$, vanishes for small values of V_R indicating that it consists of secondary electrons ejected from the reflector's plate during the arrival of heavy particles contained in the plume. For flight times longer than $5\mu sec$ at the detector arrives a part of the reflected ions. This signal shifts to shorter flight times as V_R is increased due to the acceleration of the ions by an increasing potential. Taking the difference between the arrival time of the first ions at the detector and the arrival time of the plume at the reflector yields the time the reflected ions travel to reach the detector. From this flight time, ion energies slightly lower than the applied reflector voltage are calculated, e.g. $80eV$ for $V_R = 100V$, under the assumption of singly charged Si ions. The detector signal exhibits two peaks separated by a time interval, which shortens at higher reflecting voltages.

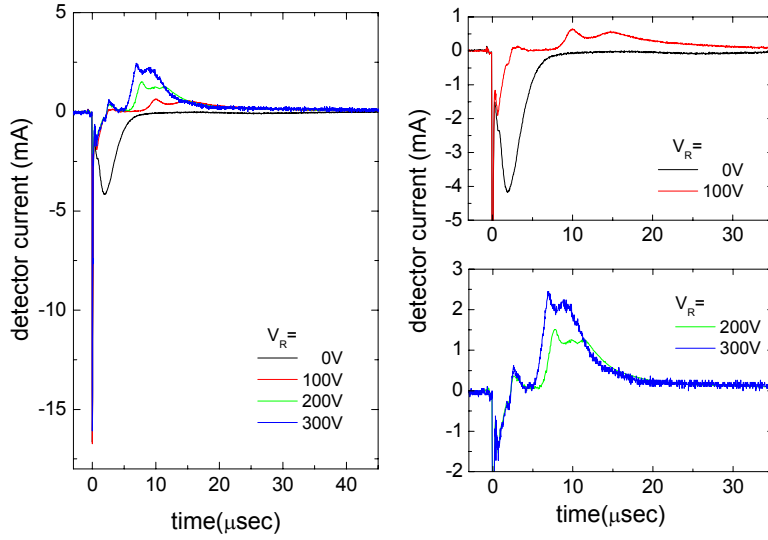


Fig. 4. 5: Detector signals measured for different values of V_R . $W.A.=50$ for 0, 100, 200V and 3 for 300V.

Integrating the current signals, we obtain the number of charges, $N_{i,e}$,

collected at the corresponding electrode as

$$\int Idt = N_{i,e}q$$

For the detector's charge we integrate the signal for flight times longer than $4\mu sec$, while for the reflector's for $1.6\mu sec$. The results are shown in Fig. 4. 6. From these graphs two observations are made: the total charge measured at the reflector increases rapidly at small values of the reflector voltage and tends to saturate for voltages higher than $200V$, and the total charge measured at the detector is about three to four orders of magnitude lower than that measured at the reflector at the same V_R . We will come back to these results in the discussion of part 4.2.1.

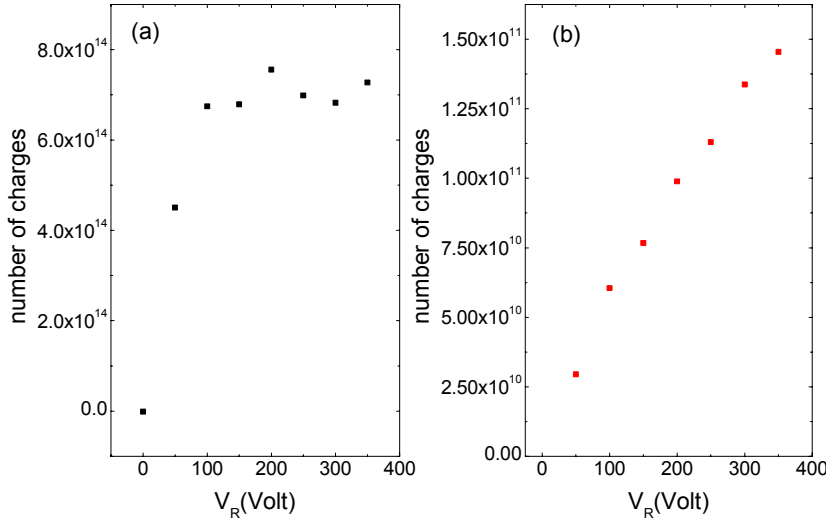


Fig. 4. 6: Number of charges obtained by integrating the signals of Fig. 4. 4 and Fig. 4. 5 respectively. (a) is the reflector's charge and (b) is the charge collected by the detector.

$$V_R > 0, a = 5 \text{ mm}$$

By reducing the grid-reflector distance, a , the reflecting electric field increases. In order to see the influence of the electric field on the reflection of ions, we performed the same measurements with a set at 5 mm . These are shown in Fig. 4. 7 and Fig. 4. 8, below, and where obtained with vacuum chamber pressure approximately $3 \times 10^{-5} \text{ mbar}$ and at the same laser fluence as the previous measurements.

The comparison of $I(t)$ for the two different values of a , Fig. 4. 9, shows that the shape of the reflector and the detector signals, does not change upon increasing a , however the increase of a corresponds to a slight increase in the detector signal and a bigger increase in the reflector signal. This can also be seen from the plots of the collected charge at the detector and the reflector versus the reflector's voltage, shown, for comparison, in the same graph, Fig. 4. 10, for the two values of a .

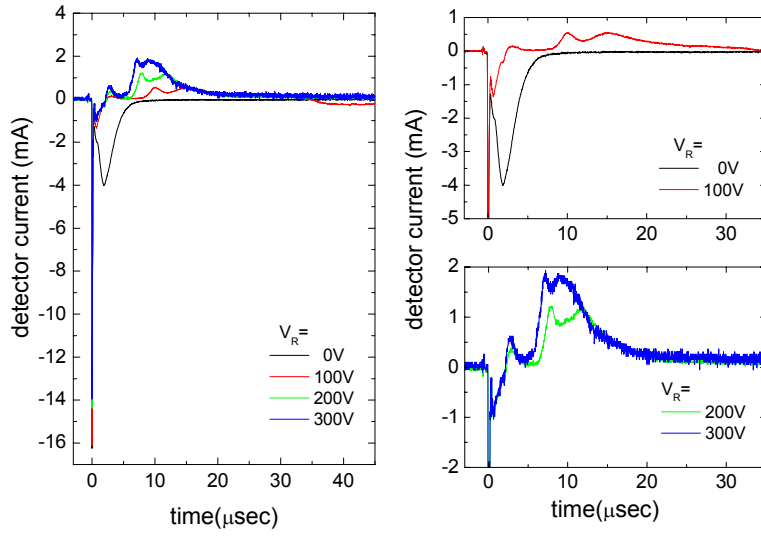


Fig. 4. 7: Reflector signal measured for different values of V_R α was set at 5mm. $W.A.=50$ for 0, 25, 50, 100V and $W.A.=10$ for 300V.

Fig. 4. 8: Detector signals with $\alpha=5$ mm. $W.A.=50$ for 0, 100V, $W.A.=10$ for 200V and $W.A.=3$ for 300V.

Fig. 4. 9: Detector and reflector signals for $V_R=250$ V. The black line is for $\alpha=11$ mm and the magenta for $\alpha=5$ mm. $W.A.=10$.

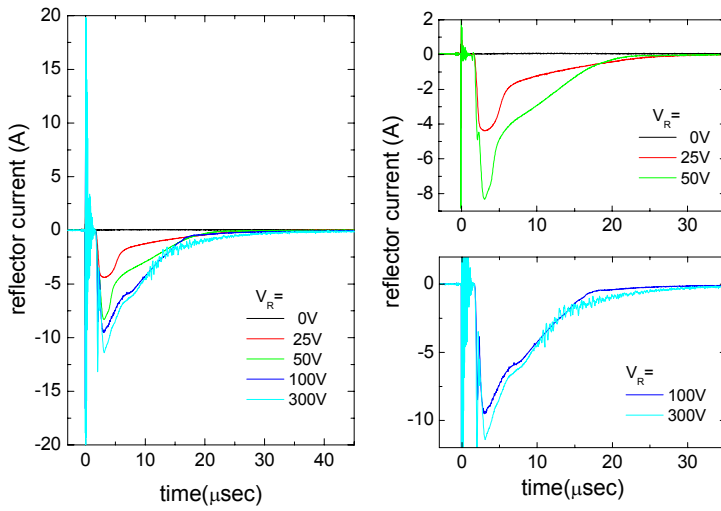


Fig. 4. 10: Comparison between the collected charge for the two different values of a . Open symbols: $a=5\text{mm}$, solid symbols: $a=11\text{mm}$. (a) number of charges collected by the reflector and (b) corresponding number of charges arriving at the detector.

The number of charges collected by the reflector increases very rapidly at small voltages and for voltages higher than $V_R = 150\text{V}$ it continues increasing however, at a smaller rate. The number of ions collected by the detector, on the other, does not exhibit any tendency for saturation. This means that even the highest reflector voltage employed were not high enough to reflect the major part of the ions. In case the major part of the ions was reflected, then the slope in Fig. 4. 10 would decrease above a certain value of V_R .

$$V_R < 0, a = 5\text{mm}$$

We examine here the electrode currents obtained with negative reflector bias. These measurements have a dual purpose:

1. to study the reflection of plasma electrons and
2. to measure the total positive charge (ion charge) collected by the reflector

In Fig. 4. 11 the measured reflector waveforms are shown. The fluence was the same as in the previous two cases $4.8\text{J}/\text{cm}^2$. From these measurements it can be seen that the reflector signal increases very slowly after $V_R = -25\text{V}$. This is expected since electrons that are repelled, have considerably lower energies than the ions and small voltages are capable of repelling the electrons. Given that the target reflector distance is 11cm the arrival time of the ions can be transformed to velocity and to energy. The corresponding waveforms are shown in Fig. 4. 12 below and represent ion current versus



ion velocity and energy. The range of these values is typical in laser ablation [1.15, 1.32].

The detector signal, Fig. 4. 13, exhibits two negative peaks, one at $\sim 2.5\mu sec$, which increases very slowly with the reflecting voltage and a second one, much broader than the first and centered at $\sim 25\mu sec$. This time is very large to be the arrival time of reflected electrons, given that the plume's arrival time at the reflector is about $\sim 1.8\mu sec$, as obtained from the reflector signals, and the detector-reflector distance is of the order of $\sim 150mm$. We suspected that the second peak corresponds to negative ions. In order to verify this hypothesis, the voltage V_R was held at $-200V$ and the pressure of the vacuum chamber was varied. At each pressure the detector signal was obtained as the average of 20 successive pulses, Fig. 4. 14. The second peak showed a strong dependence on the chamber pressure, so it could be attributed to negative ions of small energies, as manifested by the late arrival time at the detector. These ions must be formed by collisions of the reflected electrons with residual gas atoms in the vacuum chamber.

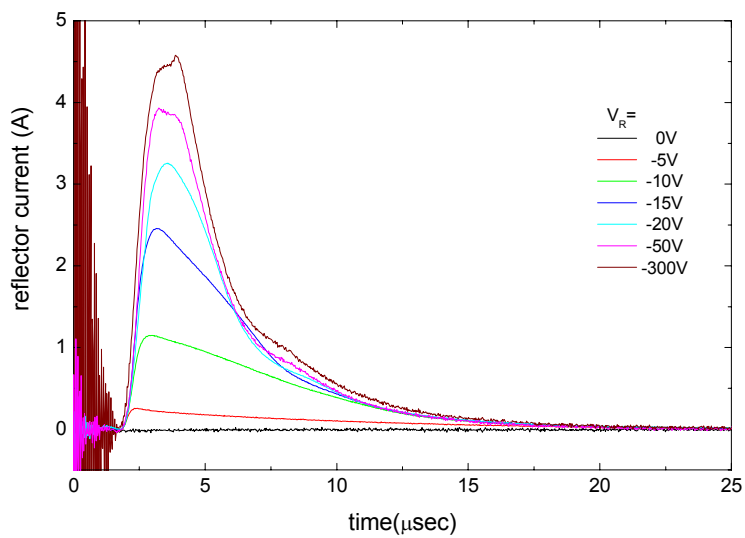


Fig. 4. 11:
Reflector
waveforms
measured with
negative
reflector bias.
 $W.A.=50$

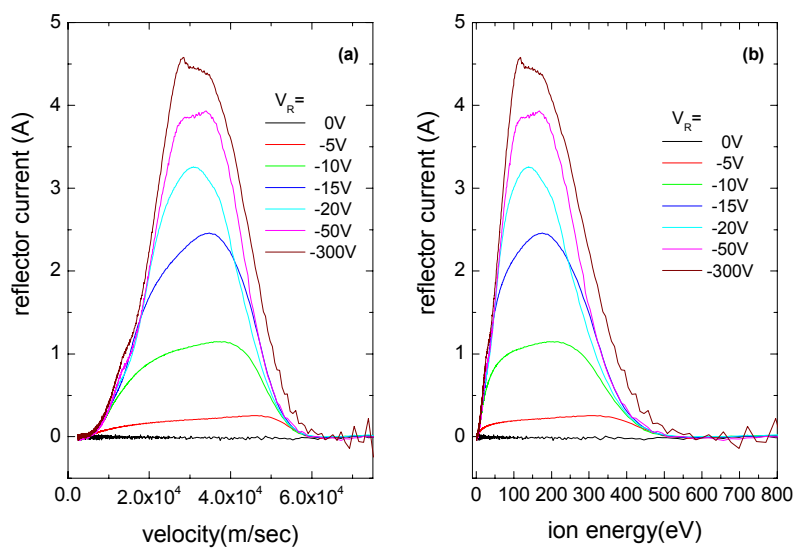


Fig. 4. 12:
Reflector
current versus
ion velocity (a)
and ion
energy(b).

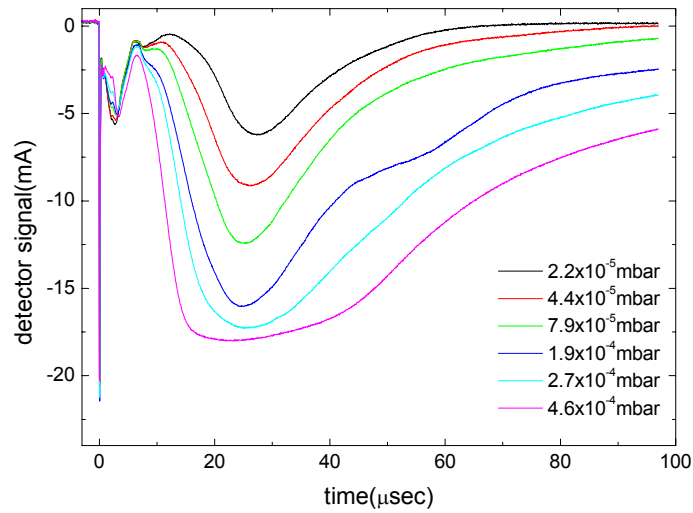


Fig. 4. 13: Detector current measured with negative reflector bias.

Fig. 4. 14: Detector signal obtained with different vacuum chamber pressure values. $V_R = -200V$.

Finally, in Fig. 4. 15 a plot of the total positive charge reaching the reflector versus the reflector voltage is shown. The maximum number of charges collected at the reflector is about 1×10^{14} charges / pulse, a value smaller than 7×10^{14} charges / pulse measured when the reflector was positively biased. The total detector charge could not be calculated since the contribution from the second peak could not be diminished. However based on the measurements of Fig. 4. 13 the number of charges giving rise to the first peak cannot exceed

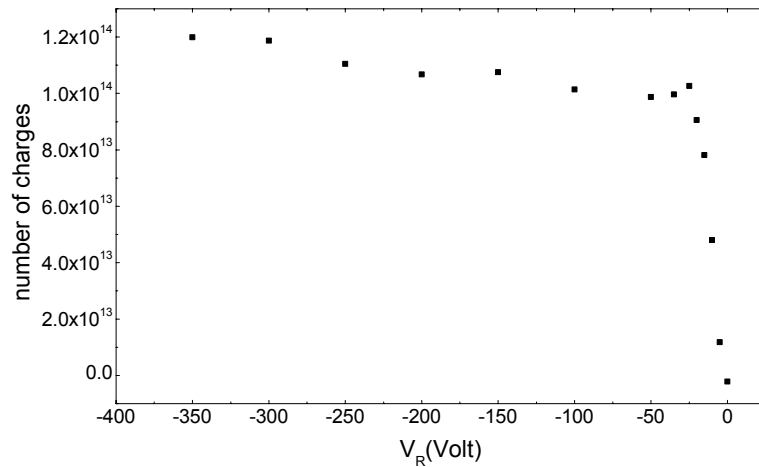
$$2 \times 10^{11} \text{ charges / pulse} .$$

Fig. 4. 15: Total positive charge measured at the reflector.

Discussion

Two key findings in the experiments presented in this section are the difference in the total charge measured at the reflector under positive and negative bias and the little dependence of the electrode currents on the grid reflector separation. Both led us to propose the following explanation that has been supported by our findings with different electrode arrangements presented in the previous sections of this chapter.

The electric field, which is present in the reflector in the absence of space charges, depends on the applied voltage and on the separation a between the reflector plate and the entrance grid. This field is approximately uniform and the potential varies more or less linearly between the two electrodes.

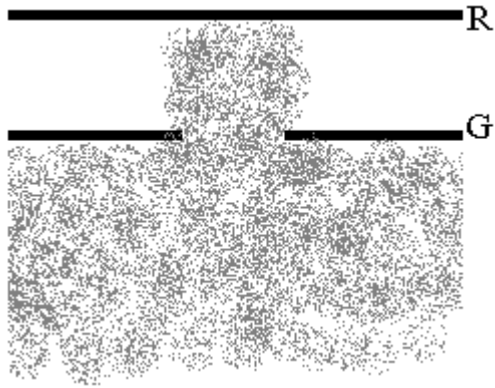


On the other hand, when dense plasma penetrates

into the space between the grid and the reflector plate, the potential difference is confined to a much thinner region; a sheath only a few microns thick, at the plasma/reflector interface, is formed. PLA plasma density at the reflector is high enough to assure that, with the exception of the thin sheaths at its limits, the plasma plume is equipotential. The reflection of ions, having kinetic energies lower than the reflector potential, which was documented by our measurements, happens in the plasma/reflector interface.

A most important question rises now. What is the potential of the core of the plasma plume, the plasma potential V_p ? Let us examine this question with the help of the electrode arrangement shown in Fig. 4. 16 which is equivalent to the reflector-cup assembly with simpler geometry. We assume that ions with large kinetic energy travel upwards and, in the absence of potential difference between the two electrodes, fall onto the first surface they encounter. A number of ions reaches the upper plate through the opening in the lower one. We can safely assume that the electron density and current to the electrodes are continuously adjusted, with time constants of the order of magnitude $1/\omega_{pe}$, much faster than the time scales of our experiments, in order to maintain the quasineutrality of the plasma plume. Let us note here that given the charge density of the PLA plume and the order of magnitude of the

capacitances involved, quasineutrality must be maintained to better than 10^{-6} in our experiments. As a general rule, when plasma is in contact with equipotential electrodes, sheaths, adjacent to the surfaces will be formed, to reduce the flow of the



highly mobile electrons so as to match that of the ions, thus maintaining quasineutrality. The plasma potential has then a positive value depending on the electron

temperature. In PLA plasma it amount to some Volts. If the plasma is in contact with two electrodes one will act as the ‘cathode’ and attract ions. Electrons will flow to the other, the ‘anode’ and two different sheaths will be established, the ‘cathode’ and the ‘anode’ sheath. Because of the much higher mobility of the electrons the potential drop in the ‘anode’ sheath will be much lower than that in the ‘cathode’ sheath if their surface areas are similar [4.1]. If this is the case, the plasma potential is much closer to that of the ‘anode’.

Fig. 4. 16: Two grounded plate arrangement

Given that quasineutrality must be maintained, the current to all electrodes in contact with the plasma must add to zero at any time. When the electrode bias is sufficient, the positive and negative carriers will be collected at different electrodes and the total charge measured is equal to that originally present in the plasma, provided that no secondary electron emission happens either on electrode surface or in the gas phase. Measurements presented in the following show that secondary electron contribution in the charges we have measured does not exceed $\sim 20\%$.

Let us now come to the large difference observed between the total electron and ion charges collected at the reflector with positive or negative bias respectively. The large translational velocities of the ions moving away from the ablation target are the key to the interpretation of this effect. We consider again the electrodes of Fig. 4. 16. Electrode G and the ablation target are maintained at ground potential. In order to better illustrate charge collection in the two polarities we consider the following bias values for V_R and assume specific values for the plasma potential based on the arguments presented above.

1. $V_R = 0V$

All electrodes are at ground potential. The plasma potential, $V_p \sim 2V$ required to keep quasineutrality by impeding electron flow to the electrodes until it matches that of the ions. No measurable net current, since for every ion arriving at an electrode an electron arrives as well.

2. $V_R = -100V$

Electrode G at $0V$ is the ‘anode’ and R is the ‘cathode’. The plasma potential is very close to the ‘anode’, which has the larger plasma/electrode contact area. Very low

barrier for ions forms in front of G. All ions with higher kinetic energies will not be prevented from falling onto G. The barrier for electrons is effective in front of R so electrons cannot reach R and all ions directed towards R, through the opening of G, will be collected. The net charge to both electrodes will correspond to the fraction of ions in the plasma directed towards the opening of G.

$$3. V_R = +100V$$

Electrode R is the ‘anode’ and G at $0V$ is the ‘cathode’. The plasma potential is of the order of $V_p \sim 20V$. We assume a much smaller contact area of the plasma with the anode than with the cathode, otherwise V_p would be closer to V_R . The barrier for ions at the anode sheath is $\sim 80V$ and all ions with kinetic energy below $\sim 80eV$ will be back reflected by R. The barrier for electrons at the front surface of G is $\sim 20V$, so no electron has enough energy to cross this barrier. As ions fall onto the front surface of G, an equal number of electrons will flow through the plasma to R. The motion of electrons in the equipotential core of the plasma is due to diffusion only and is very fast as their random thermal velocities are much higher than the ion velocities. All ions directed towards G, with the exception of the opening, will be collected by G. All electrons in the plasma will be collected by R, maybe with the exception of some dragged by the back reflected ions, if the charge of the latter is sufficient. If the entire plasma plume encounters G, the positive plasma charge is collected by G and a corresponding negative charge by R. Corrections to the previous statement come from secondary electron emission, back reflected charges and probably very low density parts of the PLA plasma for which the basic assumptions of the above reasoning may not hold.

In the light of the above considerations, the ratio of saturated total charge measured with negative and positive reflector bias should be equal to the ratio of surfaces of the reflector and of the surrounding cup, which are in contact with the PLA plasma. As the latter is difficult to estimate, we only give here a lower limit of 2.5, for the ratio of the total negative to the total positive charge, which is the inverse of the grid transmission coefficient.

The second observation concerns the total charge collected by the detector. The number of ions obtained by integration of the detector signals, Fig. 4. 10, is consistent with the number of ions reflected assuming that they are specular reflected. The number of ions reflected, when the reflector is biased at a high positive voltage, equals the number of ions collected by the reflector when it is negatively biased. This gives about 1×10^{14} ions reflected. Taking the reflector grid transparency into account yields 4×10^{13} ions exiting the reflector grid. Given the distance between the centers of the reflector and the detector, which is 95mm , and assuming specular reflection the ratio of the ions reaching the detector to the number of ions reflected equals 1.7×10^{-3} (the reflector and detector grid transparencies were taken into account). This yields about 1.7×10^{11} ions arriving at the detector, a value close to the 1.3×10^{11} ions measured experimentally with $a = 5\text{mm}$.

To determine the ionization fraction in the plume a silicon film on glass was deposited at a fluence of $4.9 J / cm^2$. The holder for the deposition was placed $12.5 cm$ above the target. In front of the glass a mask consisting of an array of $5 mm$ diameter openings was placed. In this way the steps at the edges of the deposited film could be measured to give the film thickness and thus the deposition rate. In Fig. 4. 17 a photograph of the deposited film, taken with a Nomarski microscope, is shown. The deposited film has high density of droplets on the surface.

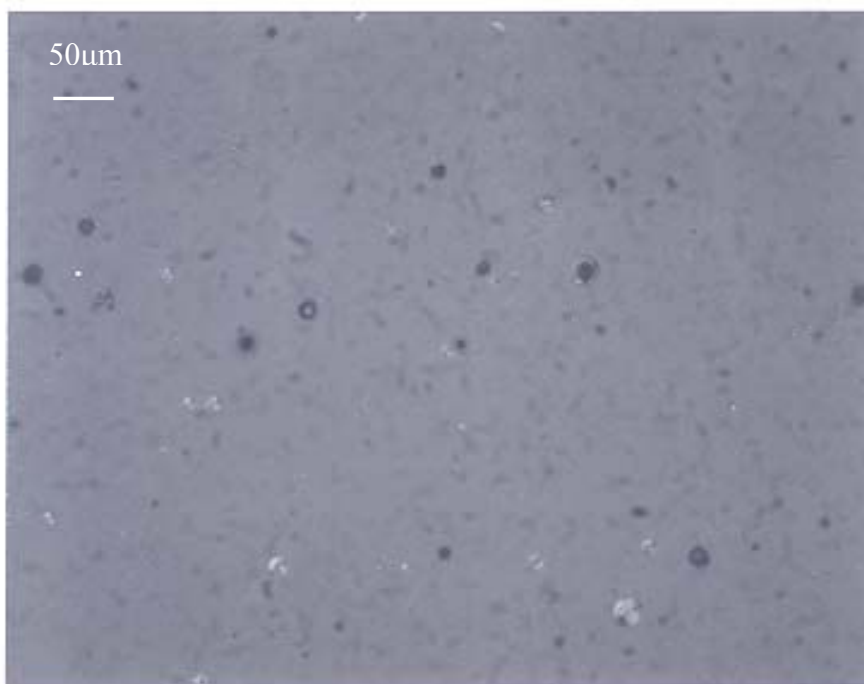


Fig. 4. 17:
Silicon film deposited on a glass substrate placed at $12.5 cm$ above the target.

The

film thickness was measured with a profilometer and was found to be of the order of 800\AA after 25000 laser pulses. This yields about 0.03\AA per laser pulse, a value lower than typical PLD rates [4.2, 4.3] due to the higher substrate to target distance than those usually employed in PLD. Given the lattice constant at room temperature of silicon, which equals 5.4\AA , the atom density is found to be $5 \times 10^{22} \text{ cm}^{-3}$. Per unit surface the number of atoms deposited at 12.5 cm above the target is equal to $1.6 \times 10^{13} \text{ cm}^{-2}$. At the reflector plate, which is located at 11.5 cm above the target, the number of atoms per unit area becomes $1.9 \times 10^{13} \text{ cm}^{-2}$. The reflector area is equal to 36 cm^2 , which leads to approximately 7×10^{14} atoms per pulse reaching the reflector. The number of ions collected by the reflector was approximately equal to 1×10^{14} .

Taking the grid transparency into account leads to 2.5×10^{14} ions arriving in front of the reflector, which gives an ionization fraction, that is number of ions collected to number of atoms deposited, of the order of 35%. This means that the ionization degree of the plasma as measured at distances far from the target is quite high. This value lies within the range of typical ionization coefficients already reported to exist in laser ablation plasmas, as mentioned in paragraph 1.6.

Let us use the number of ions collected by the reflector per pulse to make an order of magnitude estimation for the Debye length. According to

eq.(2.3) the Debye length is given by $\lambda_D = (\epsilon_0 k T_e / e^2 n)^{1/2}$.

In order to estimate λ_D we need the electron temperature and the density. As mentioned in §1.5, typical values for the electron temperature lie in the range of some eV , i.e. $2eV$ [2.33]. The total number of ions per pulse arriving in front of the reflector was found to be of the order of 1×10^{14} ions. Dividing by the grid transparency yields the total number of ions arriving in front of the reflector. Taking into account the volume of the cone from the laser spot on the target up to the reflector, which equals $132 cm^3$, an initial estimation of the ion density is $3 \times 10^{12} cm^{-3}$.

This value is consistent with these reported in [2.33]. Inserting these in the equation for the Debye length gives $\lambda_D = 6 \mu m$, a value much smaller than the plume dimensions, in agreement with [4.4], and also much smaller than usual grid spacings. In [4.4] it was found that the ratio of the Debye length to the plume size, after the plasma has expanded, increases only slightly from its initial value, which was found to be of the order of 10^{-4} . However, the portion of the plasma that enters the reflector has lower density, due to the grid, and hence longer Debye length, than that estimated above, by a factor of about 1.6.

To summarize, using this set-up the reflection of the plasma ions using a positively biased surface was verified. The arrival of the ions at the detector shifted to earlier times as the reflecting potential increased, indicating the reflection of the ions by an

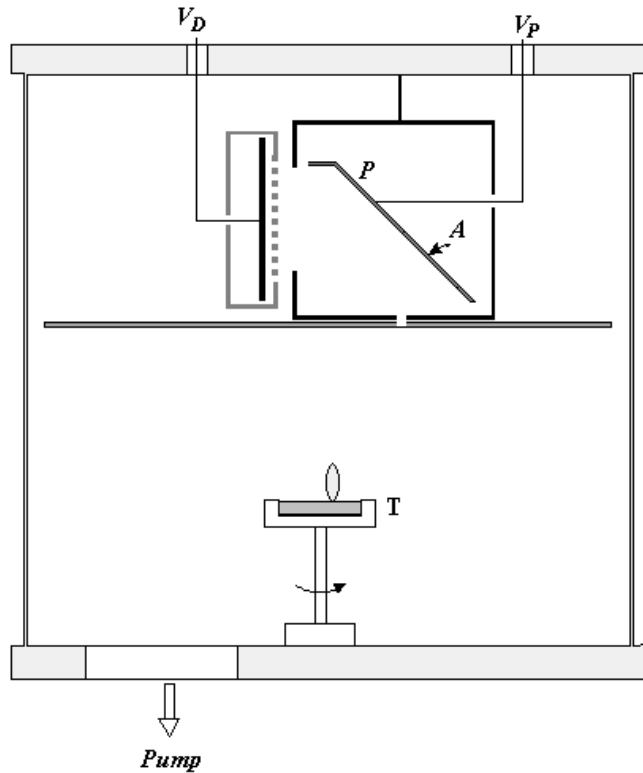
increased barrier. Also the number of detected ions increased, consistent with the reflection of more energetic ions. Moreover estimations of the ion and neutral densities, of the Debye length and of the ionization degree were made. The total number of ions arriving at the detector increased linearly with the reflector voltage. In the following we will examine the ion yield using a different geometry set-up, which has larger angle between the target normal and the reflecting electrode normal, to increase the reflection efficiency at lower voltages.

4.2.2 45° Angle-reflection

Experimental set-up

In this part the second auxiliary set-up for ion reflection is presented. The angle between the ion reflecting plate and the expansion axis of the plume is smaller than the one in the previous set-up. This is expected to increase ion reflection at lower reflection bias, since in this way the ion velocity component perpendicular to the plate is decreased. Another difference with respect to the previous set-up is that the reflected ions do not have to travel through a region where plasma is present. So scattering of reflected ions is expected to decrease.

The reflecting plate was placed in a metal box whose bottom had a rectangular opening, the entrance aperture, 5mm wide and 25mm long, through which a part of the plume could enter the box and reach the plate. At the side opposite to the plate, the box had a circular opening of 55mm diameter as shown in Fig. 4. 18. The detector, D, used was the same one as in the previous set-up and was mounted outside the box.



Both the detector and the plate were isolated from the metal box, which was at ground potential. In front of the box, at 94mm above the target, a metal plate was mounted. This plate was held at ground potential and was used to protect the detector from the part of the plume that could arrive there directly from the target. The plate had two openings, one for the laser beam and a second one, below the entrance aperture of the box, for the plume.

The laser beam entered the vacuum chamber through the window at the top of the chamber, in the direction normal to the page, and passed through an aperture opened at the plate in front of the box. The angle of incidence and the spot dimensions on the target were the same as in the previous part.

Fig. 4. 18: View of the experimental set-up. *T* is the target, *D* the detector, *G* are the strings, *P* the plate. The laser beam entered through the window, on the top of the vacuum chamber, in the direction normal to the page, thus it is not shown.

Measurements

Effect of secondary electron emission

In order to apply the desired voltage on the plate and to measure the corresponding current during the arrival of the plume, the circuit, shown in Fig. 4. 19, was used. The plate current was calculated by measuring the voltage drop on R_4 using the oscilloscope probe.

Fig. 4. 19: Plate bias and current measurement circuit. $R_1=500\Omega$, $R_2=1k\Omega$, $R_3=R_4=1\Omega$, $C=150\mu F$ and V_P is the voltage supply.

At the beginning we will examine how much the measured detector signals are altered in the case where the secondary electrons emitted from the detector plate during the impingement of ions are not suppressed. The current of the grid in front of the detector plate was measured as well. In the case where the secondary electron emission is not an important component of the measured signal this will permit the biasing of the whole detector (plate and cup) at the same voltage and the measurement of the total ion current exiting the box.

To discriminate the detector plate from the plate used for reflecting the ions, in the following we will use the term detector for the detector plate and



the term screen for the grid covering the detector entrance.

For these measurements the detector was held at either positive or zero potential with respect to the screen and the corresponding signals were measured. The electric circuits used at the detector and the screen were identical and utilized a capacitor in parallel to the voltage supply, to stabilize the applied voltage, and a resistance to ground, as shown below. The current was calculated by measuring the voltage drop on R , again using the oscilloscope probe.

Fig. 4. 20: Detector bias and current measurement circuit. $R = 47\Omega$, $C = 220\mu F$ and V_d is the voltage supply.

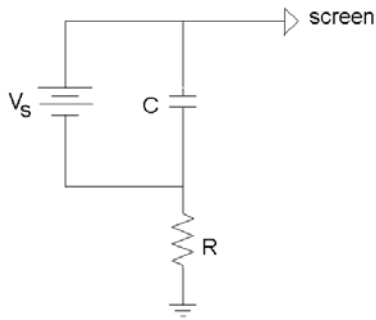
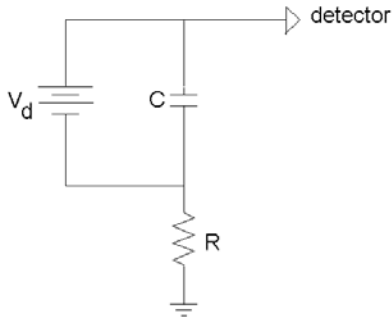
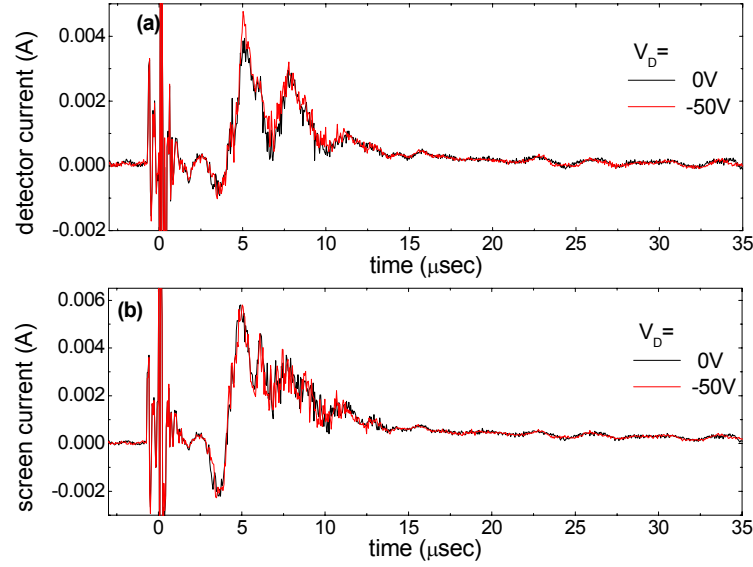


Fig. 4. 21: Screen bias and current measurement circuit. $R = 47\Omega$, $C = 220\mu F$ and V_s is the screen voltage.

Keeping the plate voltage at $V_p = 200V$ and the screen voltage at $V_s = -50V$ the measured detector and screen signals are shown in Fig. 4. 22. These measurements

were performed at a vacuum chamber pressure of $3 \times 10^{-5} \text{ mbar}$ and laser fluence of 4.1 J/cm^2 . As can be seen both detector and screen signals do not change upon applying the detector the same negative bias as the screen.

Fig. 4. 22: (a) Detector signals for different detector voltages (b) corresponding screen signals. For all waveforms $V_S = -50 \text{ V}$, $V_P = 200 \text{ V}$ and $W.A. = 50$.



With the screen biased at $V_s = -200 \text{ V}$ and $V_s = -300 \text{ V}$, the detector signals are slightly modified when suppressing the secondary electrons as can be seen from Fig. 4. 23 and Fig. 4. 24. The observed change in the detector signal is of the order 20% at $V_s = -300 \text{ V}$ and of the order of 13% in the case where $V_s = -200 \text{ V}$. It is expected that as the screen and plate voltages are increased the secondary electron emission coefficient will increase [4.5], due to more energetic ions impinging on the plate. This is the reason why the signals of Fig. 4. 23 and Fig. 4. 24 change when suppressing secondary electron emission.

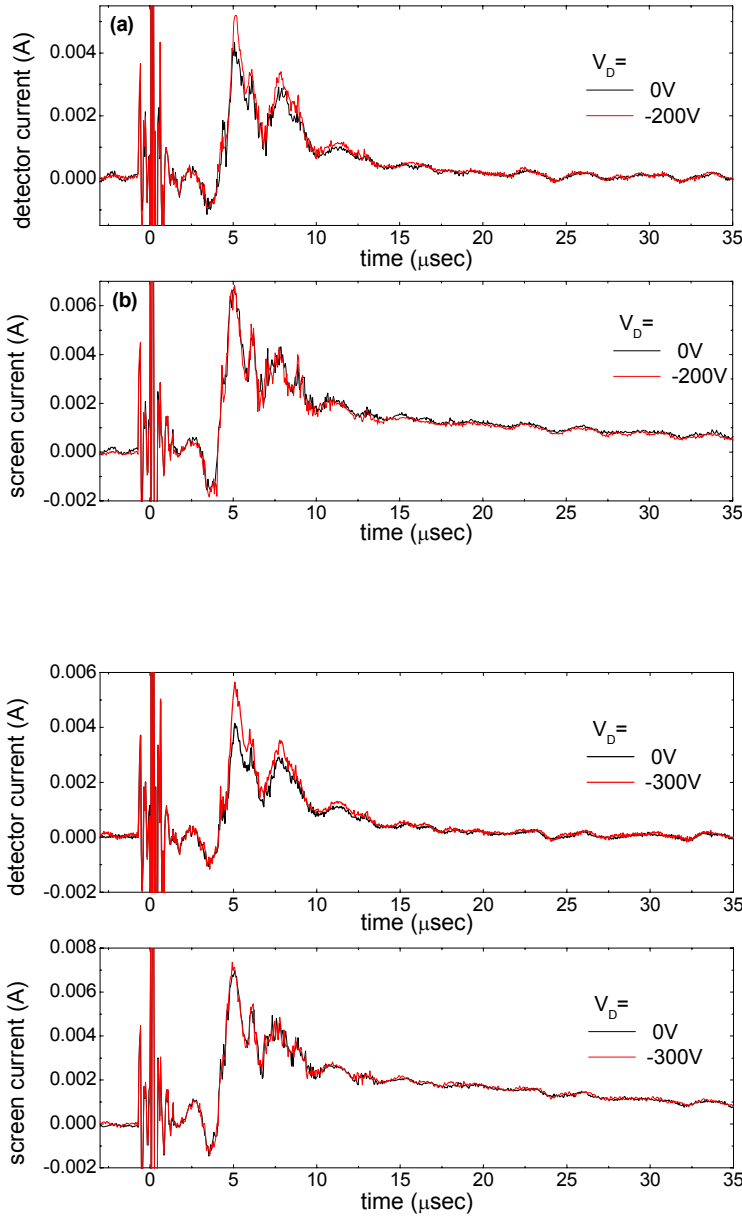


Fig. 4. 23: (a) Detector signals measured for two different detector voltages and screen voltage $V_s = -200V$ and (b) the corresponding screen signals. $V_P = 200V$, $W.A. = 50$.

Fig. 4. 24: Same as in Fig. 4. 23 with screen bias $V_s = -300V$. $W.A. = 50$.

From the above measurements it can be seen that secondary electron emission does not contribute significantly to the measured detector signals so, in the following, where the performance of this setup will be tested, the whole detector (plate and cup) will be biased at the same voltage, which will be referred to as detector voltage hereafter.

Let us examine the effect of the plate and the detector bias on the corresponding signals as well as how they influence each other. For this reason the grid, G, was grounded and only the plate and the detector voltages were varied. The vacuum chamber pressure was approximately $3.5 \times 10^{-5} \text{ mbar}$, the laser fluence was 4.3 J/cm^2 and W.A was 50.

Effect of plate voltage

With the detector biased at $V_D = -100 \text{ V}$, the plate and detector signals were recorded versus plate voltage. These are shown below in Fig. 4. 25 and Fig. 4. 26. The plate signal shows a strong increase with the plate voltage especially up to 100 V , while at higher voltages it continues increasing, exhibiting at the same time a change in shape with the discrimination of four peaks. These peaks become sharper and shift to smaller times as the voltage is increased. The detector signal also increases with the reflecting voltage and at high voltages sharp peaks also appear. Also the arrival of the first ions at the detector shifts to shorter times as the plate voltage is increased. The detector current however is about three orders of magnitude lower than the plate current.

Fig. 4. 25: Plate signals for various bias voltages. In (b), (c) the same signals as in (a) are shown, separated, for clarity. $W.A.=50$.

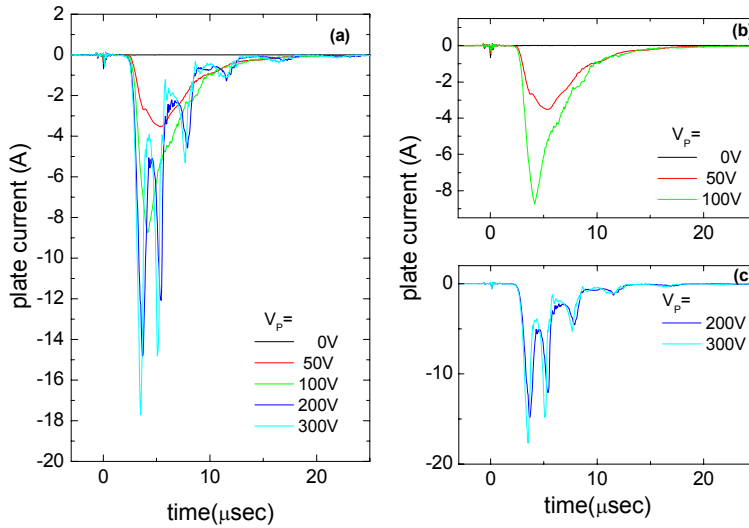


Fig. 4. 26: Detector signals obtained with $V_D = -100V$ and varying plate voltage. In (b), (c) the signals of (a) are shown, on a smaller time scale. $W.A.=50$.

Effect of detector voltage

Next, the plate voltage was kept fixed at $V_p = 100V$ and $V_p = 300V$ and the detector voltage was varied. Changing the detector voltage had no effect on the plate signal, as can be seen from Fig. 4. 27, where the recorded plate signals are shown. The detector signal, on the other, showed an increase, which was more pronounced at longer times, more than $10\mu s$. The detector signals are shown in Fig. 4. 28 and Fig. 4. 29.



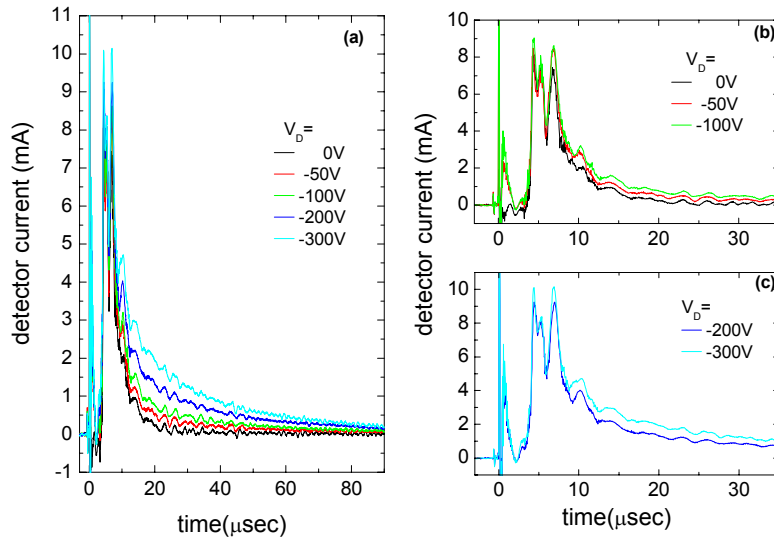


Fig. 4. 27: Plate signals obtained under for various detector voltages. (a) $V_P = 100V$ and (b) $V_P = 300V$. $W.A.=50$

Fig. 4. 28: Detector signals obtained for different detector voltages and $V_P = 100V$. In (b), (c) the signals of (a) are shown, on a shorter time scale. $W.A.=50$.

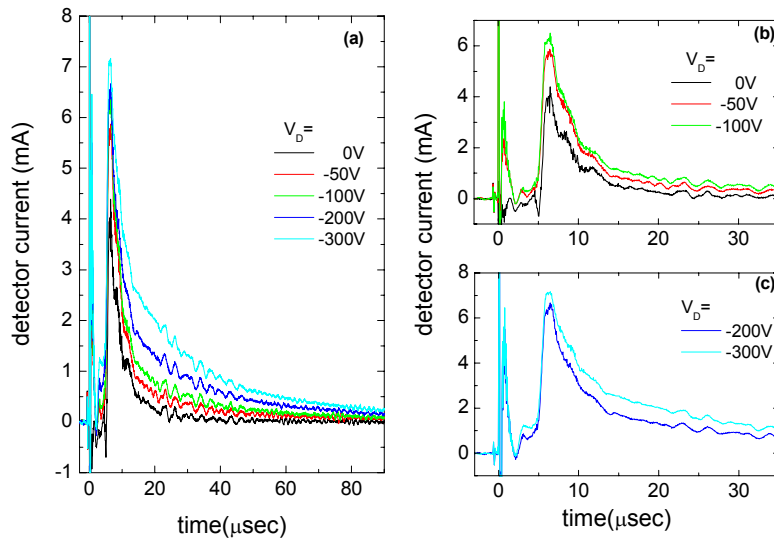


Fig. 4. 29: Same measurements as in Fig. 4. 28 with $V_P = 300V$. $W.A.=50$.

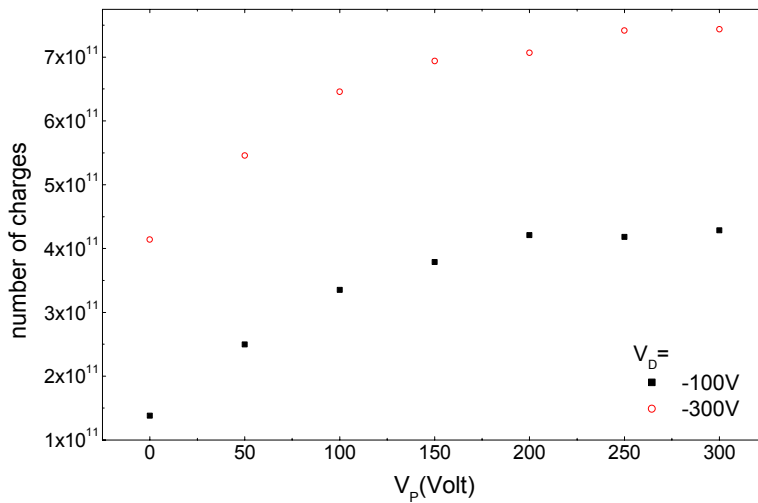
The total charge collected by the detector can be obtained by integrating the detector signals, as in the previous part. In Fig. 4. 30 the detector charge versus the

plate voltage, for two different detector voltages, is shown. For both voltages the integrated charge increases with V_p , however at a smaller rate as the plate voltage is raised above $V_p > 200V$. In the case where the plate voltage remains constant and the detector voltage is varied, a linear increase in the total charge with the detector voltage is observed,

Fig. 4. 31.

The number of charges arriving at the plate as a function of the plate voltage is shown in Fig. 4. 32. The number of charges collected by the plate is about two orders of magnitude higher than the corresponding number of charges arriving at the detector.

Fig. 4. 30: Number of charges collected by the detector, versus plate voltage, for different detector voltages. The values were obtained by integrating the signals for times longer than $2.3\mu s$.



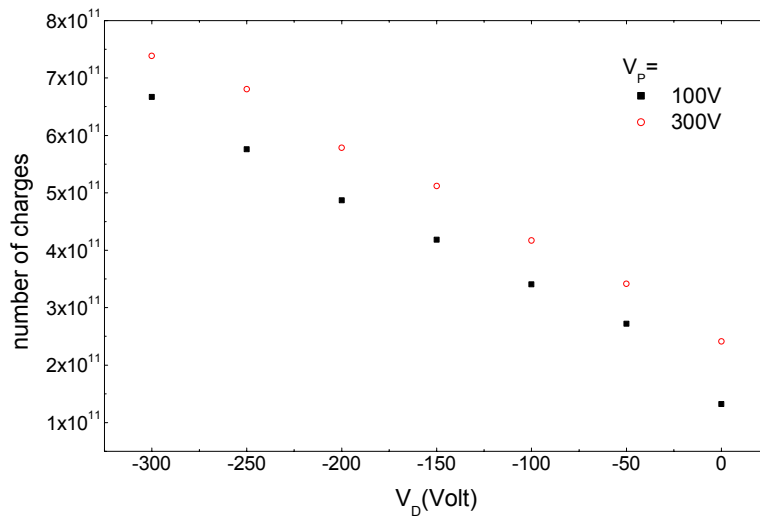


Fig. 4. 31:
Number of charges collected by the detector, versus detector voltage, for different plate voltages. The values were obtained by integrating the signals for times longer than $2.3 \mu s$.

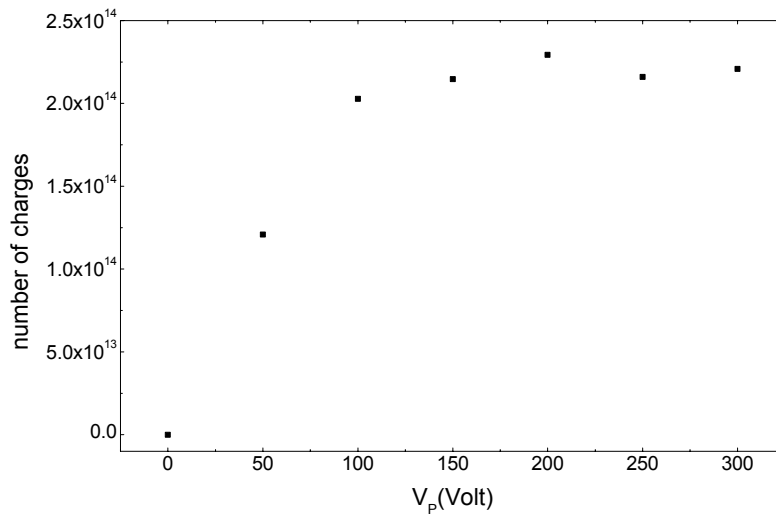


Fig. 4. 32:
Number of charges collected by the plate versus plate voltage. Calculated by integrating the signals of Fig. 4. 25 for times

longer than $1.6 \mu s$.

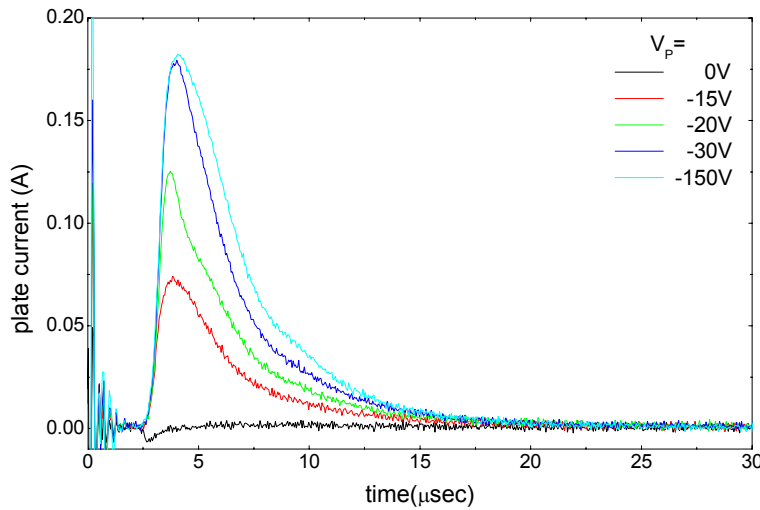
Total positive charge

In order to evaluate the ion reflection yield the number of ions collected by the plate is required. Therefore the plate was negatively biased, so that the electrons were repelled and the plate collected the net positive charge. The vacuum

chamber pressure, when performing these measurements, was approximately $3.7 \times 10^{-5} \text{ mbar}$ and the laser fluence 4.8 J/cm^2 . The plate voltage necessary to repel all electrons, is of the order of 30 V , as can be seen from Fig. 4. 33, where the plate current versus time is plotted for different values of V_p . It is seen that the arrival time of the plasma at the plate is of the order of $2.5 \mu\text{sec}$ while the peak of the current occurs at $4.1 \mu\text{sec}$. Given that the distance from the target to the point A of Fig. 4. 18 is 14 cm , the first ions arriving at the plate have energies of the order of 450 eV , while the peak corresponds to ion energy of the order of 170 eV . These values are very close to those measured in the previous set-up Fig.

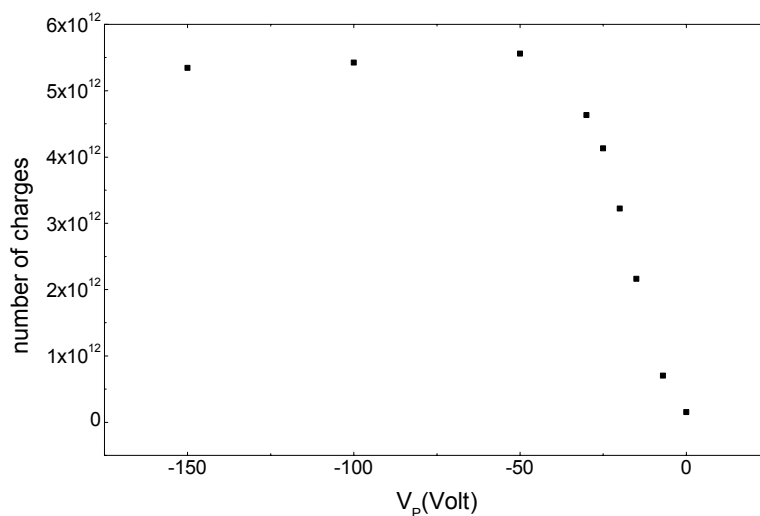
4. 12.

Fig. 4. 33: Plate current for negative values of plate voltage. $W.A.=50$.



Integrating the above signals yields the number of charges arriving at the

plate versus V_p , shown in Fig. 4. 34. The total number of ions arriving at the plate, which corresponds to signals measured with $V_p > 30V$, so that the plate signal has reached its saturation value, is of the order of $5.5 \times 10^{12} \text{ ions / pulse}$. In Fig. 4. 30 and Fig. 4. 31, we saw that the maximum number of



charges the detector could collect was of the order of

$7.5 \times 10^{11} \text{ ions / pulse}$

. This represents 13.6% of the positive charge entering the box.

Fig. 4. 34: Number of charges collected by the plate versus plate voltage.

Discussion

From the measurements presented above some conclusions can be drawn. First of all the efficiency of the reflection is seen to increase when using this set-up as can be seen from the plots of the total ion charge collected by the detector, Fig. 4. 30 and Fig. 4. 31, versus the total ion charge collected by the plate, Fig. 4. 34. This can be attributed to the small fraction of the plasma that enters the metal box and hence to the lower density close to the reflecting plate. The second observation that is made from Fig. 4. 30 is that the total ion charge collected by the detector exhibits a tendency for saturation when the plate voltage is increased above $150V$. On the contrary, when using the previous set-up, a linear increase of the detector charge versus the reflector voltage up to $V_R = 350V$ was observed, Fig. 4. 9. This difference can be attributed to the decreased component of the ion velocity, perpendicular to the plate surface and means that the plate can reflect ions that have higher energy than the plate's voltage. On the other, we observed a linear increase of the collected charge versus the detector voltage.

Another observation is the pronounced difference in the ion charge collected by the plate when it is negatively biased ($\sim 5 \times 10^{12}$ maximum number of ions) relative to the charge collected under positive bias ($\sim 2 \times 10^{14}$ maximum number of charges). This difference can be explained by the same argument that was used to interpret the

difference between the total positive and negative charge collected by the reflector (part C of paragraph 4.2.1). However, in the present case due to the small dimensions of the entrance aperture we expect that the number of charges collected by the plate under positive bias will far exceed those collected under negative bias. When compared to the measurements of the previous set-up, the total ion charge seems to scale with the ratio of the area of the entrance aperture, at the bottom of the box, to the area of the reflector.

Finally, the shape of the waveforms measured at the plate, under high positive bias $V_p > 200V$, is totally different from that of the reflector under comparable bias. A multi peak structure is observed in the former case in contrary to the two-peak waveform measured using the reflector. When the plate voltage exceeds $200V$ the shape of the waveform measured at the detector also changes, Fig. 4. 26, from singly, to doubly peaked. The origin of this multi peak structure is not known.

4.2.3 *10° Angle-reflection*

Experimental set-up

The setup presented in this section, shown in Fig. 4. 35, is a complete source design for ion implantation using PLA plasmas. It is based on the electrostatic ion reflection whose study is presented in the previous sections of chapter 4. The angle between the average incident ion trajectory and the reflecting surface is further decreased to 10° . The reflecting surface is the inside of a hollow cone and the grounded counter-electrode shielding the cone from the ablation target is a cylinder with a central rod that serves a dual purpose. 1) It blocks the optical contact between the ablation target with the exit orifice of the cone in order to prevent neutral matter from exiting the cone and 2) It increases the counter-electrode surface area which is necessary for increasing the voltage drop on the an anode sheath, a prerequisite for ion reflection to occur.

The total length of the cone is 122.5mm , while the bottom radius and the top radius of the cone are 31mm and 15mm , respectively. The cylinder has 51mm diameter, 43mm length and is placed at 82mm above the target. The rod in the center of the cylinder has 10mm radius and the detector's radius is 14mm . Secondary electron emission is not expected to constitute a serious component of the detector signal, for the range of voltages employed, and this is the reason why a singly biased plate is used for detection.

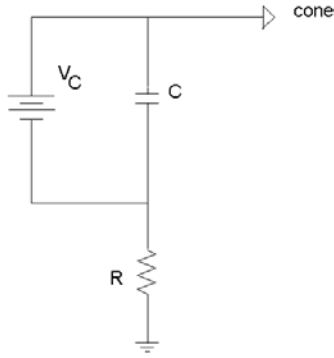


Fig. 4. 35: View of the experimental set-up. T is the target, V_C is the voltage applied to the cone and V_D is the voltage applied to the detector.

To apply a voltage V_C to the cone and to measure the current the circuit, shown in Fig. 4. 36, was used. As in the previous set-ups, a capacitor in parallel to a voltage supply, to stabilize the voltage during the arrival of the plume and a resistor to the ground to measure the number of charges impinging on the cone were used. As in the previous set-ups, the waveforms measured were the average of a sufficient number of successive waveforms.

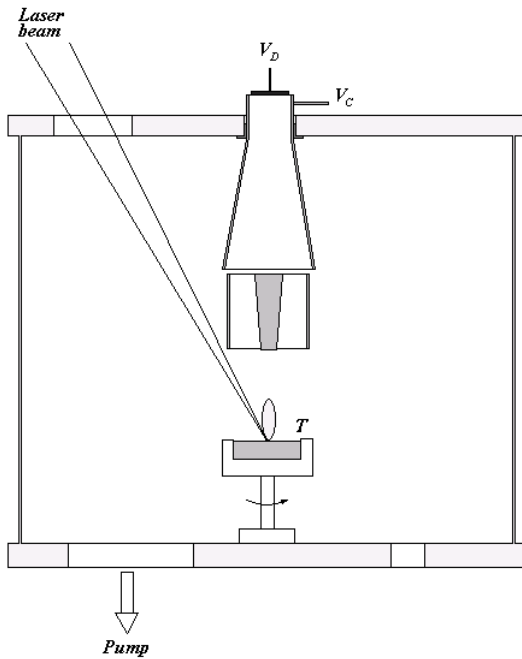


Fig. 4. 36: Cone bias and current measurement circuit. $C = 2200\mu\text{F}$, $R = 0.5\Omega$ and V_C is the voltage supply.

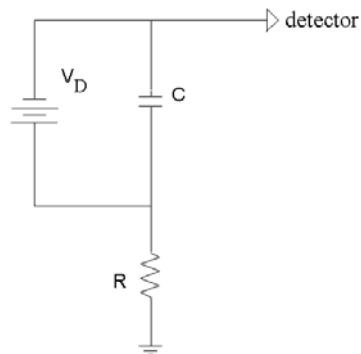
A similar circuit, however with different values for the capacitance and the resistance was used at the detection as seen from Fig. 4. 37.

Fig. 4. 37: Detector bias and current measurement circuit. $C = 1\mu F$, $R = 10\Omega$ and V_D is the voltage supply.

Measurements

The measurements presented in this section were performed with laser fluence of $4.4J/cm^2$ and vacuum chamber pressure approximately $6 \times 10^{-5} mbar$. The detector was biased at $V_D = -50V$ and this voltage was kept constant for all the measurements to follow. This value was chosen after performing some preliminary

measurements, which showed that the detector signal did not change upon increasing further V_D .

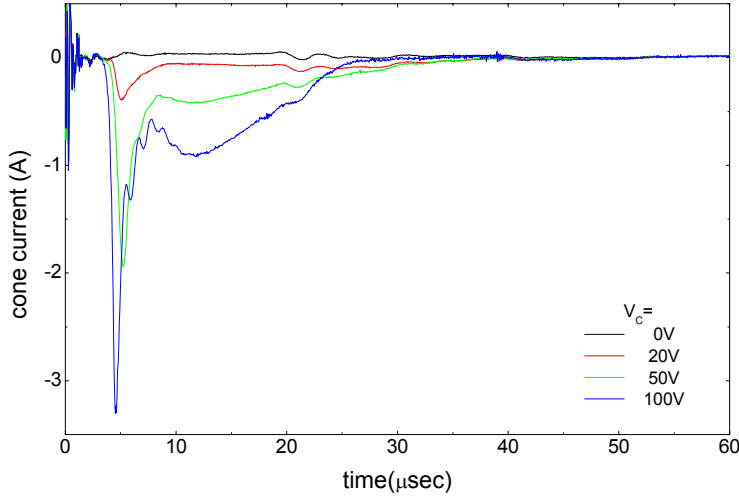


Positive cone bias

At the beginning the cone was biased positively, to repel the ions and the cone and detector current were recorded. The measured waveforms are shown below in Fig. 4. 38 and Fig. 4. 39.

Fig. 4. 38: Cone signals measured by changing the cone voltage. $W.A.=50$.

At $V_c = 30V$ the cone current exhibits a negative peak centered at $\sim 5\mu s$. This peak



shifts to shorter times as V_C increases and above $V_C = 50V$ a second peak appears centered at $\sim 11\mu s$. At the detector, on the other hand, a small magnitude signal, increasing with

V_C , appears. Its duration and time dependence do not change upon increasing V_C .

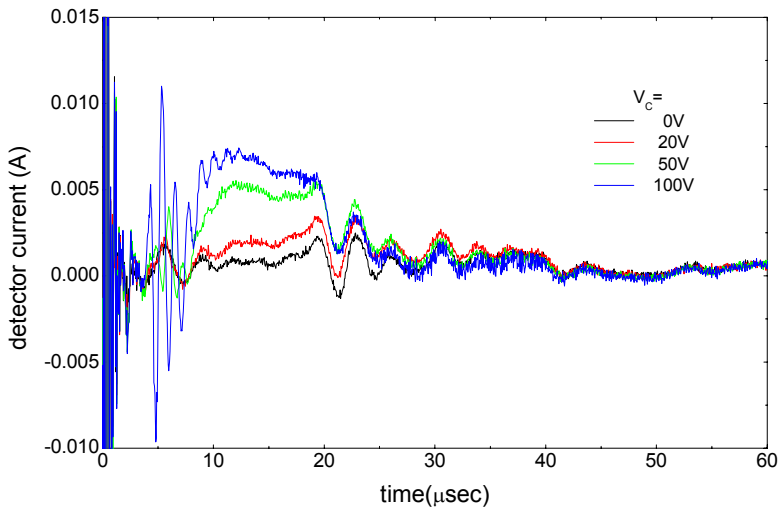


Fig. 4. 39: Detector signals measured by changing the cone voltage. $W.A.=50$.

The number of

charges arriving at the cone and the detector are obtained by integration of the signals shown in Fig. 4. 38 and Fig. 4. 39 and are shown in Fig. 4. 40 and Fig. 4. 41. The number of ions arriving at the detector is maximized when the cone voltage is set to $100V$ and is of the order of $6.4 \times 10^{11} \text{ ions}$. Given the detector radius and assuming that the ions are homogeneously distributed on the detector surface the dose of the ions collected by the detector equals $1 \times 10^{11} \text{ ions/cm}^2$. Under the same bias the number of electrons collected by the cone is of the order of 10^{14} .

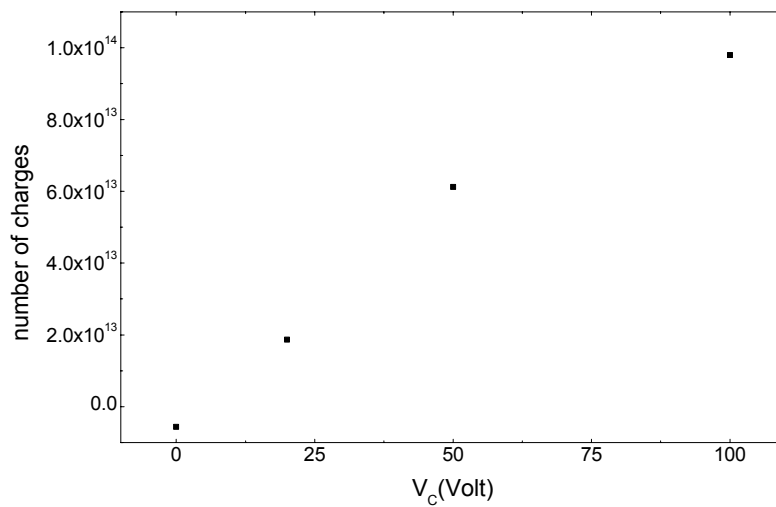


Fig. 4. 40: Number of electrons arriving at the cone versus V_C . Obtained by integrating the signals of Fig. 4. 38 for flight times longer than $2.7 \mu \text{sec}$.

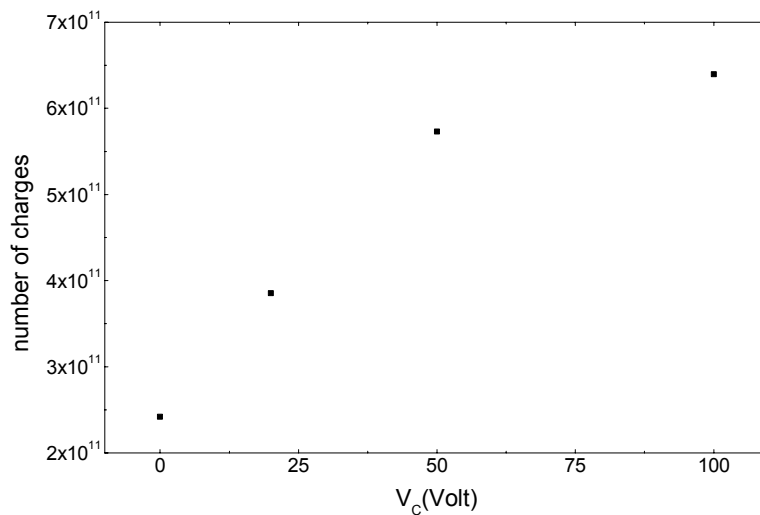
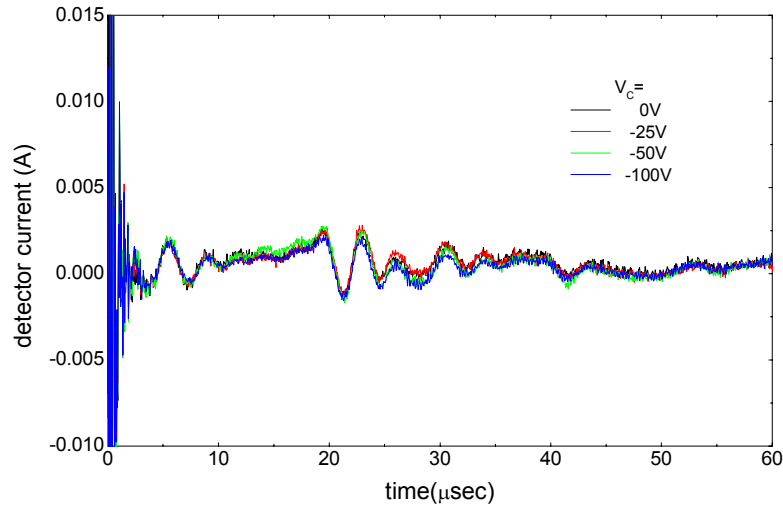
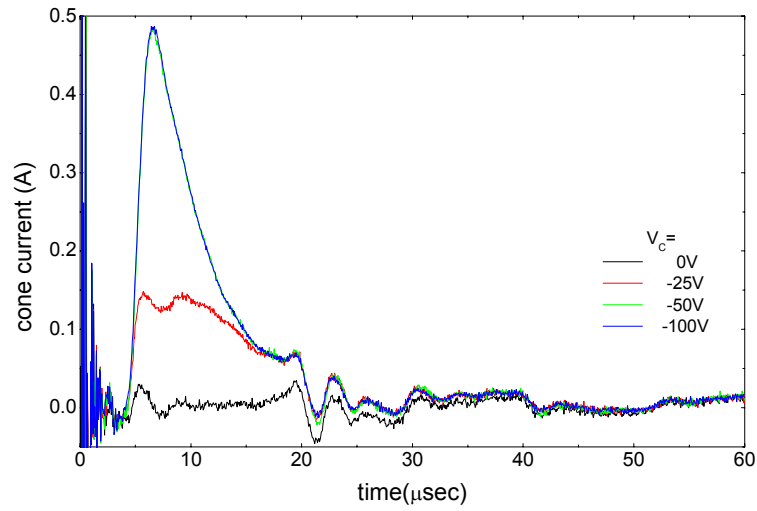


Fig. 4. 41: Number of ions arriving at the detector versus V_C . Obtained by integrating the signals of Fig. 4.

39 for flight times longer than $7.2\mu\text{sec}$.

Negative cone bias



Following the cone was negatively biased and the cone and detector waveforms were recorded, and are shown below in Fig. 4.42 and Fig. 4.43.

Fig. 4. 42: Cone signals measured for negative cone voltages. $W.A.=50$.

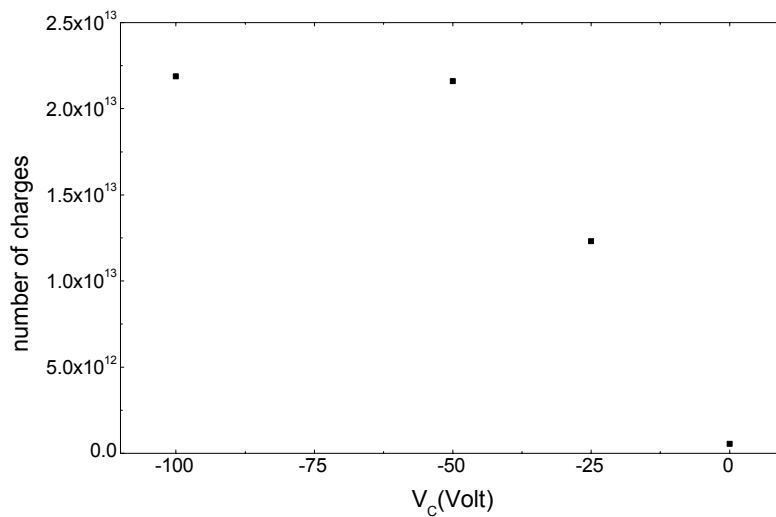


Fig. 4. 43:
Detector traces
for negative
cone voltages.
 $W.A.=50$.

The cone
signal is
shown to

saturate when biasing the cone more negative than $V_c = -50V$ and the maximum number of ions arriving there is of the order of 2.2×10^{13} . This can be seen from Fig. 4. 44, where the number of ions arriving at the cone is plotted, against V_c . At the detector a zero signal is measured in this case, as expected, since the ions are collected by the cone and the electrons are expelled due to the large negative bias applied.

Fig. 4. 44: Number of ions arriving at the cone versus the cone voltage.

Discussion

The $I(t)$ waveforms of the cone assembly are difficult to interpret because of the extend of this source along the z-axis. Roughly speaking, the flight times observed are consistent with our previous measurements. More detailed comparison is uncertain

and unnecessary. The simpler electrode arrangements are more appropriate for the study of PLA plasma plumes. The insertion of electrodes with various geometry and bias certainly affects the profile of the plasma as was also observed by Shinohara et al [4.6]. We were more interested to evaluate the performance of the cone assembly as an implantation source rather than understanding every feature of the current waveforms at its electrodes.

The total number of ions reaching the detector is increased with respect to that of the previous setups. This was expected as the cone assembly is the first complete source design collecting at its entrance the largest part of the PLA plume. However the reflection efficiency of this source is only 3% significantly reduced when compared to that of the previous setup, which was 13.6%. We define the reflection efficiency as the ratio of ions reflected and collected by the detector to those reaching the cone when the latter is at negative bias.

We have obtained with the previous setups good reflection efficiency by sacrificing a large fraction of the PLA plasma. As the cone assembly measurements show, the reflection efficiency for the entire PLA plume is low despite the two precautions we have taken in designing this source. These are the relatively large counter-electrode surface area intended to increase the voltage drop in the anode sheath and the small angle between the incident ion velocities and the reflecting surface, which allows for reflection of higher energy ions by a moderate barrier. In the next chapter we present results obtained with the cone assembly with the addition of a magnetic field parallel to the z-axis covering the entire region of the cone.

CHAPTER 5

MAGNETIC PLASMA GUIDING

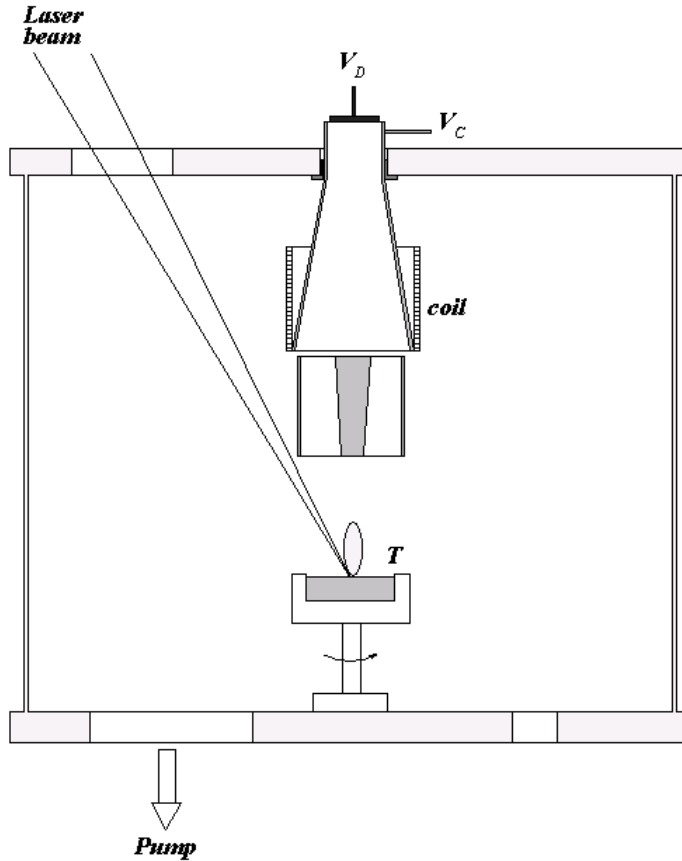
From the discussion of the previous chapter it becomes clear that the magnitude of the voltage drop in the anode sheath is of key importance in determining the efficiency of electrostatic reflection of ions. This drop can be increased by decreasing the ratio of anode to cathode surface area considerably [4.1] or by decreasing the electron mobility at the anode. The former proved to be impossible without sacrificing a large part of the PLA ions. This is not desirable since the output of the source is the product of efficiency and input flux. It makes no sense to improve one at the expense of the other. A moderate magnetic field can decrease the mobility of electrons moving in directions perpendicular to \vec{B} . In this way the electron collection by the cone under positive bias will be decreased since the electrons will be forced to follow helical orbits along the cone axis.

Magnetic fields are used in vacuum arc plasmas, for macroparticle filtering [5.1]. The presence of the magnetic field is found to be of crucial importance for efficient plasma transport through the duct. This is achieved by using magnetic field strengths high enough to ensure that the electron Larmor radius is much smaller than the duct radius, but not so strong as to lead to ion Larmor smaller than the duct radius. In this way the mobility and the diffusion of the electrons in the direction perpendicular to the magnetic field can be decreased. The electrons in this case, via ambipolar electric fields, determine the transport of the [5.2]

ions and guiding of the plasma parallel to the magnetic field is achieved.

1.15 Experimental

A. Experimental set-up



As can be seen from Fig. 5. 1 the magnetic field is created by a coil, wrapped around the lower part of the cone. This coil is 6cm long and has 400 turns, of insulated copper wire, 1mm in diameter. The magnetic field in the center of the coil is given by

$$B = \mu_0 \frac{N}{l} I$$

where

$\mu_0 = 4\pi \times 10^{-7} \text{ Tm/A}$ is the free space permeability, N is the

number of turns, l is the coil's length and I is the current in the coil. Using the above mentioned values and inserting them in the last equation yields

$$B = 8.38 \times 10^{-3} I$$

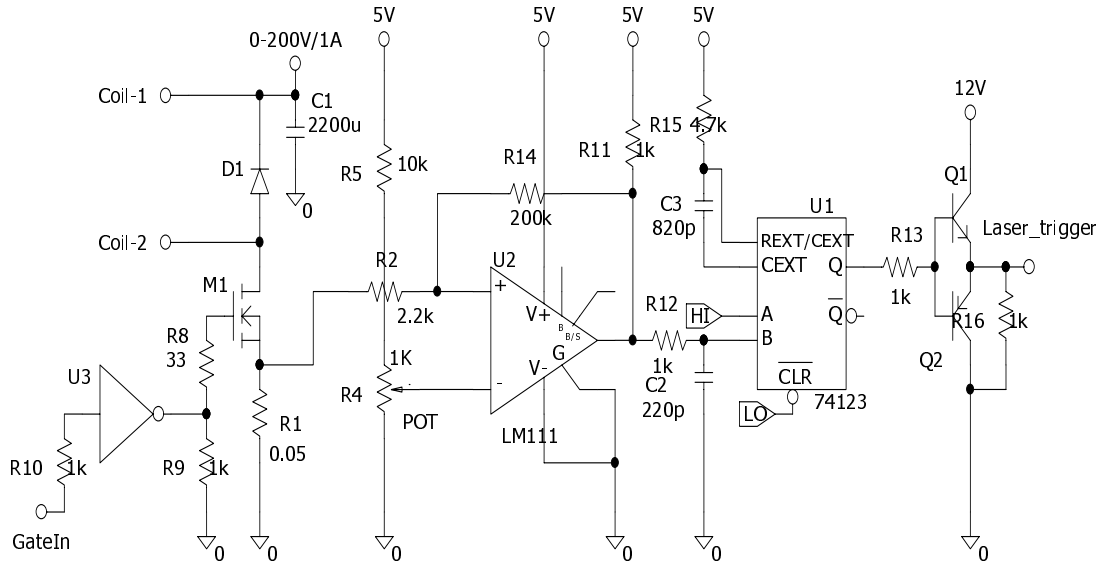
which is the equation relating the magnetic field created to the coil current.

Fig. 5. 1: View of the experimental set-up. T is the target, V_C is the voltage applied to the cone and V_D is the voltage applied to the detector. Throughout this chapter V_D is set to $-50V$. The position of the coil is also shown.

For a magnetic field strength of $100mT$ the current of the coil should be equal to $12A$, which would lead to coil heating. However, as the period of the laser pulses (the inverse of the repetition rate of the laser) is larger than $100ms$, B can be increased drastically during the ion flight time without excessive heat dissipation in the coil. In order to achieve this we have used a specially designed and constructed pulse supply whose basic schematic is presented in Fig. 5. 2. A large electrolytic capacitor ($2200\mu F$, $250V$) with low equivalent series resistance (ESR) is charged by a moderate current DC power supply. At a given repetition rate of the order of a few Hz, a voltage pulse at the gate of a power MOSFET closes the circuit through the coil producing a current rising at a rate determined by the coil's self inductance and the capacitor voltage of up to $200V$. The current through the coil is monitored with the help of a 0.05Ω resistor. When this current reaches an adjustable predetermined value, a trigger pulse for the laser is output. The duration of the coil current pulse is longer than the longest ion flight times, which are less than $30\mu s$. The monostable multivibrator (74123) has been added to the circuit, Fig. 5. 2, in order to meet the laser's trigger pulse requirements. Pulsed coil currents in excess of $20A$ have been achieved. The allowable DC current through the coil employed is $2A$.

Fig. 5. 2: Schematic of the pulse supply.

The voltage at the cone and the detector was applied by the same circuits as those used in the previous chapter, which are shown in Fig. 4.34 and Fig. 4.35.



B. Measurements

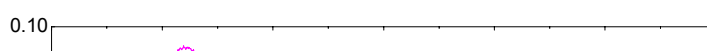
The duration and the period of the current pulses could be adjusted by programming a pulse generator to produce the desired waveform. However the duration used should be long enough for the current in the solenoid to reach the steady state value. This means that the pulse length should be longer than about four times the time constant of the solenoid, that is the ratio L/R , where L is the inductance and R resistance of the solenoid. The inductance of a coil of wire is given by $L = \mu_0 N^2 A / l$, A being the cross-sectional area of the solenoid. Specifically, for the solenoid used here, $A = 30.2 \text{ cm}^2$ which results in an inductance equal to $L = 10.1 \text{ mH}$. To calculate the resistance of the coil the resistivity, ρ , of copper is

required, which is $1.77\mu\Omega\text{cm}$. The resistance then is evaluated from the relation $R = \rho l'/s$, where l' is the total length and s is the cross section of the copper wire. Using this relation we find $R = 1.8\Omega$. The time constant is then found to be 5.6ms , which means that the current pulse should be longer than 20ms . In order to check this, different current pulse durations were used and for each of them the detector current was recorded. The corresponding signals are shown in Fig. 5. 3. Those signals were obtained with a maximum current of 15A and cone and detector voltages equal to 6V and to -50V , respectively. The laser fluence was $4.4\text{J}/\text{cm}^2$ and the pressure in the vacuum chamber was approximately $5 \times 10^{-5}\text{mbar}$. For the same reasons, as in the previous chapter, the detector voltage was set equal to -50V for all the measurements that were performed and will be presented here. From Fig. 5. 3 the detector current is seen to increase with increasing pulse width and to saturate for pulses with duration longer than 17ms , which corresponds to about three times the time constant of the solenoid. It was not possible to increase the pulse width above 25ms because the total charge in that case exceeded the charge available at the capacitor. Thereafter, current pulses of 25ms duration and 530ms period were used to create the magnetic field, since they were found to give the highest ion yield at the detector.

Fig. 5. 3: Current measured at the detector for different pulse duration, τ , of the current that creates the magnetic field. T is the period of the waveforms. Maximum current 15A and $W.A.=50$.

Positive cone-voltage

In this section we examine the effect of the cone voltage on the detector current for different values \vec{B} . At the beginning a magnetic field of 50mT was used. The vacuum chamber pressure was approximately $6 \times 10^{-5}\text{mbar}$ and the laser fluence was $4.4\text{J}/\text{cm}^2$. The measured current of the cone, shown in Fig. 5. 4 is positive at low values of the cone voltage, indicating that it collects ions and becomes increasingly negative as the cone voltage exceeds 30V . The initial effect of increased V_C is to



reduce the signal at longer flight times, while the positive first peak remains until the voltage is increased above $20V$. The detector current, Fig. 5. 5, is seen to increase at relatively low values of V_C , up to $6V$, whereas at higher voltages it decreases with increasing V_C . The reason for this is that increasing the cone voltage leads to increased number of electrons collected by the cone. These electrons contribute significantly to the plasma transport so the application of a large positive bias decreases the plasma transport efficiency. This effect is also observed in magnetic ducts, where the application of a large positive bias at the duct results in decreased ion number at the detector [5.3].

The same tendencies in the cone and detector current are observed when the magnetic field is increased, as can be seen from Fig. 5. 6 and Fig. 5. 7, which are the same measurements as Fig. 5. 4 and Fig. 5. 5, performed however, with a magnetic field of $125.7mT$.

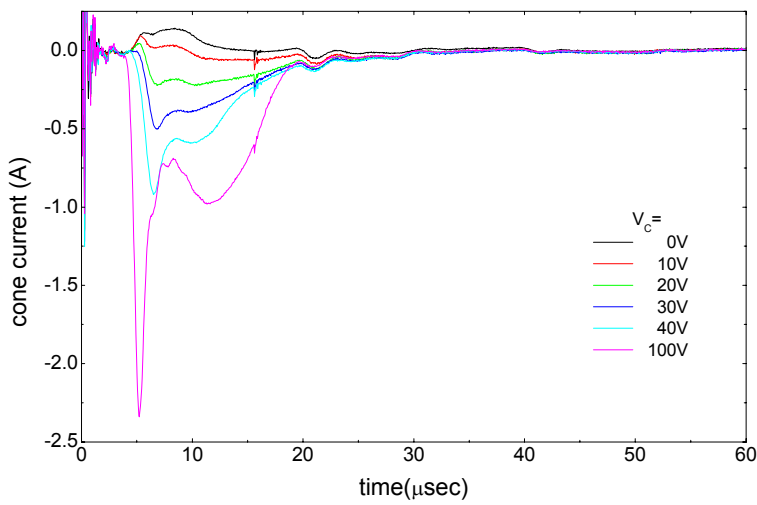


Fig. 5. 4: Cone current for different voltages applied on the cone. $B = 50mT$, $W.A. = 50$.

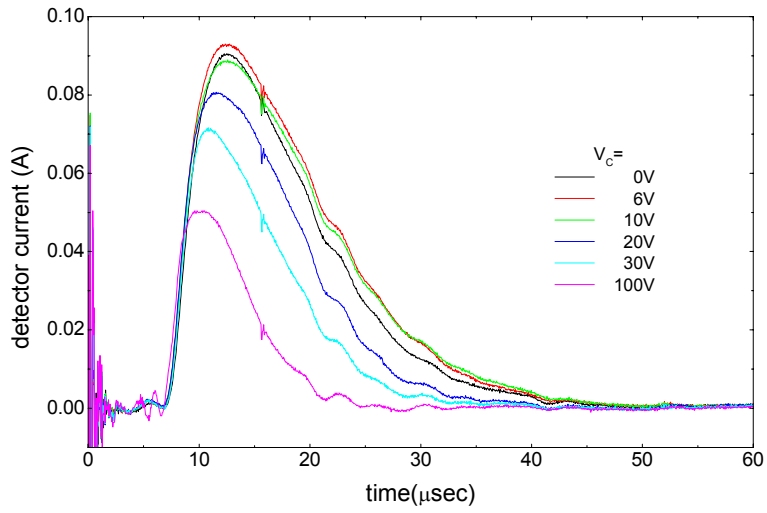


Fig. 5. 5: Detector current for different voltages applied on the cone. $B = 50\text{mT}$, $W.A.=50$.

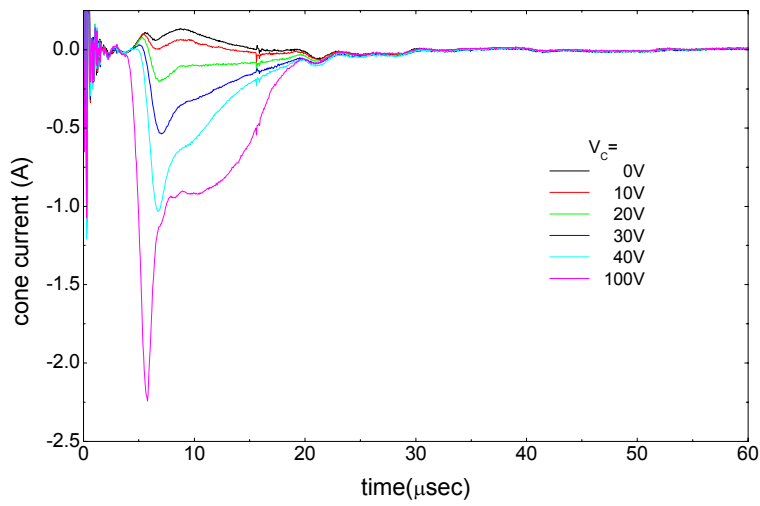


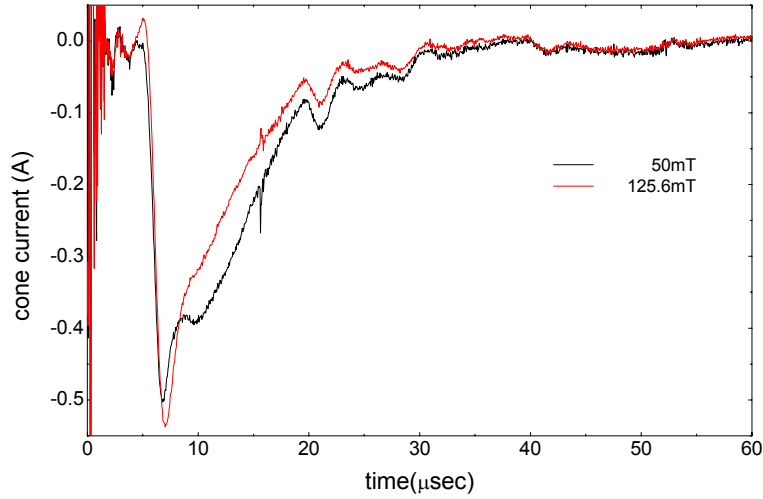
Fig. 5. 6: Cone current obtained by changing the voltage applied to the cone. $B = 125.7\text{mT}$, $W.A.=50$.

Fig. 5. 7: Current of the detector for different voltages



applied on the cone. $B = 125.7\text{mT}$, $W.A.=50$.

The time corresponding to the negative peak in the cone current shifts slightly to longer times when the magnetic field is increased, as can be seen from Fig. 5. 8, where the cone current waveforms measured with $V_C = 30\text{V}$, for both strengths of the magnetic field used, are plotted for comparison in the same graph. At the detector the current measured using the 125.7mT field is slightly increased with respect to the current measured at 50mT magnetic field, for cone voltages up to 10V . Increasing, however, further the cone voltage results in the opposite situation that is the detector current measured with 50mT field is higher than that measured when the magnetic



field equals 125.7mT .

Fig. 5. 8: Comparison of the cone current measured for the two different magnetic strengths. $V_C = 30\text{V}$.

The total number of electrons collected by the cone is seen to decrease when the magnetic field strength increases, Fig. 5. 9. This is expected, since increasing the field results in increased electron confinement [5.4] and hence to decreased electron collection by the cone at a given voltage.

By integrating the signals of Fig. 5. 7 and Fig. 5. 5 the number of ions arriving at the detector as a function of the voltage applied to the cone is obtained and is shown at Fig. 5. 10.

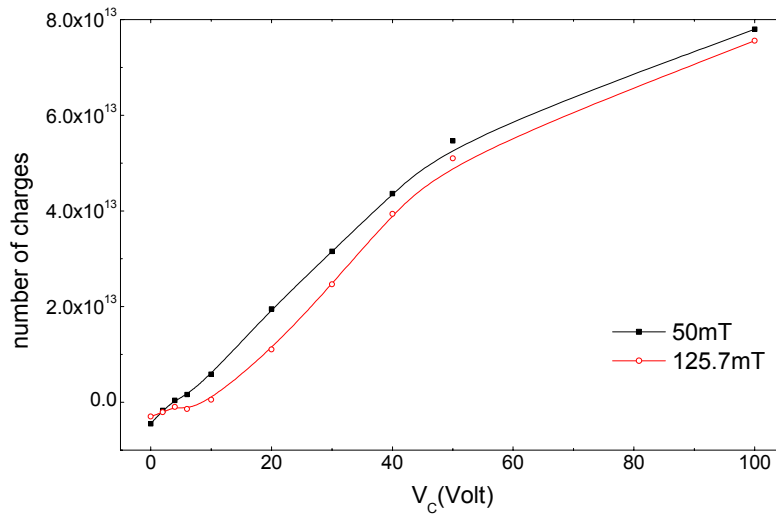


Fig. 5. 9:
Number of
electrons
collected by the
cone. The lines
are guide to the
eye.

The maximum number of ions collected by the detector is of the order of 9×10^{12} when the cone voltage is set to $4V$ and the magnetic field is $125.7mT$. This number equals an ion dose of the order of $1.5 \times 10^{12} ions / cm^2$, which is much higher than that obtained with no magnetic field.

Fig. 5. 10: Number of ions collected by the detector versus cone voltage for the two different magnetic field strengths. The lines are guide to the eye.

Negative cone-voltage

Following the voltage applied to the cone was made negative and the same measurements were performed to see the effect of the negative cone bias on the cone and detector current under different magnetic field strength. In the case where the lower magnetic field was used, the cone current, Fig. 5. 11, increased up to $V_C = 50V$, reaching $0.36A$ and then remained constant. At the higher magnetic field strength the cone current, Fig. 5. 12, increased slightly after $V_C = -50V$, reaching $0.45A$ at $V_C = -100V$.

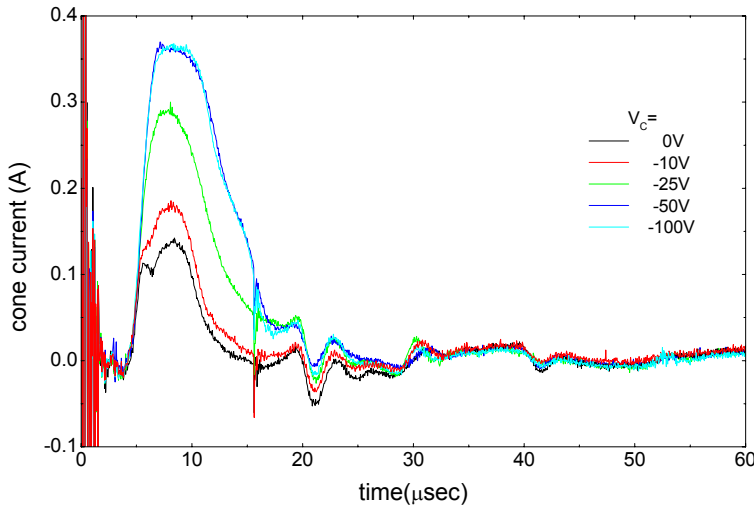


Fig. 5. 11: Variation of the cone current for negative cone biasing. $B = 50mT$, $W.A. = 50$.

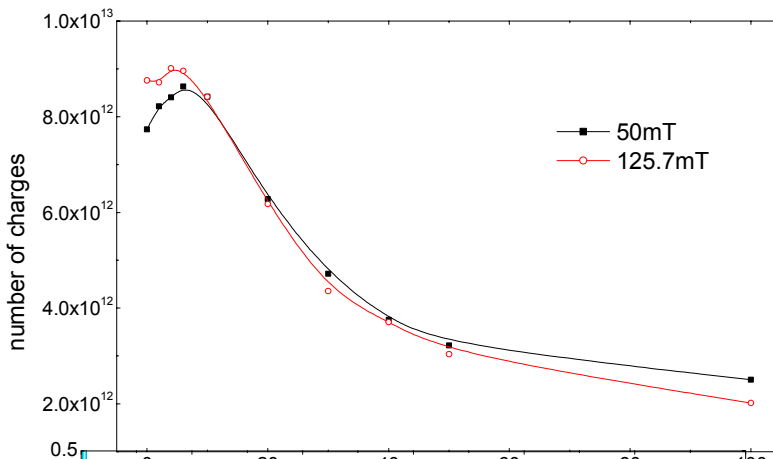
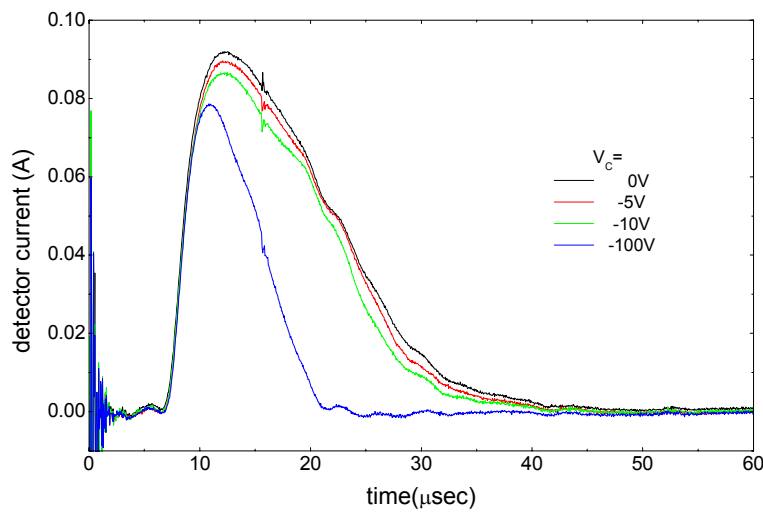
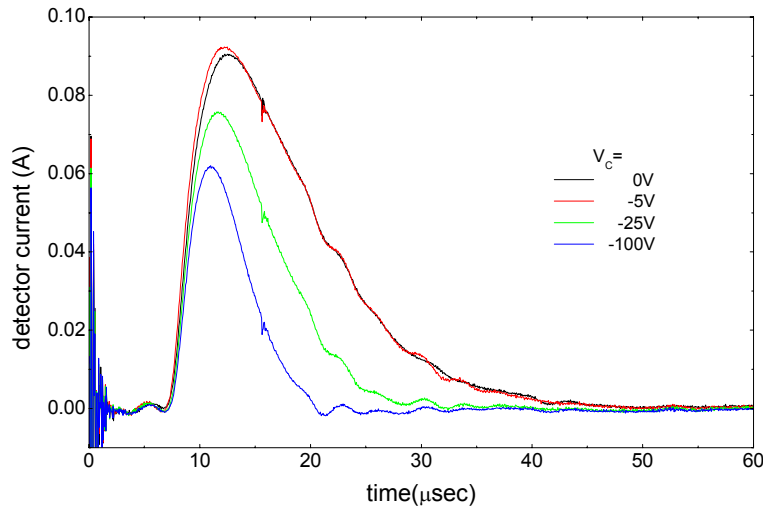


Fig. 5. 12: Same as the previous graph but for the

higher magnetic field strength used. $B = 125.7\text{mT}$, $W.A.=50$.



At the detector, on the other, the current decreases with increased cone voltage, for both magnetic field strengths used. However, the decrease is more pronounced in the case of 50mT , as can be seen from Fig. 5. 13 and Fig. 5. 14 where the detector current for different cone voltages is plotted for

$B = 50\text{mT}$ and 125.7mT respectively.

By integrating the above signals the number of ions collected by the cone and detector can be calculated. It is interesting at this point to plot the total charge collected by the cone for the positive and negative bias, in the same graph Fig. 5. 15. In order to see the overall effect of the magnetic field the total charge collected in the absence of the magnetic field is also be included.

Fig. 5. 13: Detector current measured for different cone voltages. $B = 50\text{mT}$, $W.A.=50$.

Fig. 5. 14: Same as the previous graph but for magnetic field strength equal to 125.7mT . $B = 125.7\text{mT}$, $W.A.=50$.

Fig. 5. 15: Total charge collected by the cone versus cone voltage for different magnetic field strengths. The lines are guide to the eye.

The more pronounced differentiation in the cone charge, caused by the magnetic field, is at the higher positive cone voltages, where the magnetic field strongly reduces the number of the collected electrons. Also at zero cone voltage the magnetic field restricts the electrons from reaching the cone, resulting in the collection of a net positive charge.

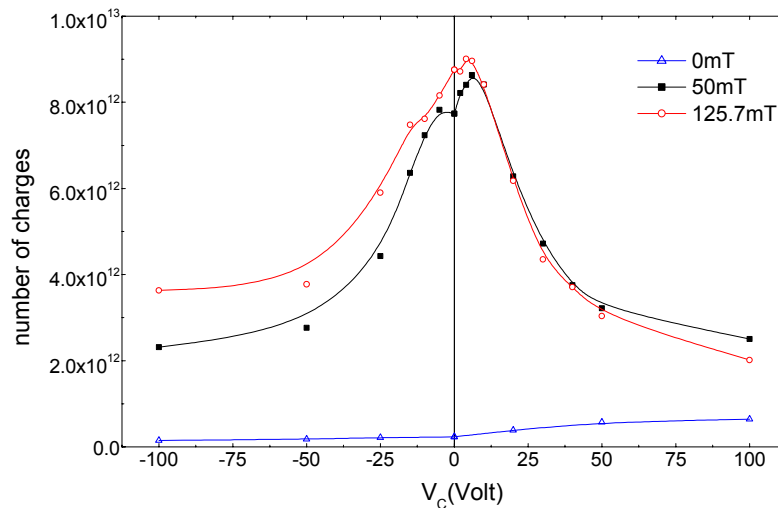
At the detector the presence of a magnetic field is of great importance in achieving efficient plasma guiding to the detector, as can be seen from Fig. 5. 16. The presence of a magnetic field results in the collection of a large number of ions by the detector even at zero cone voltage. The effect of the cone voltage is to further enhance

plasma guiding by creating a barrier that reflects the ions back to the plasma. Increasing the cone voltage further than $V_C = (4-6)V$, results in decreased guiding efficiency, since electrons are drawn from the plasma by the cone voltage. To decreased guiding efficiency results and the negative bias of the cone.

Fig. 5. 16: Number of ions collected by the detector versus cone voltage for different magnetic field strengths. The lines are guide to the eye.

C. Discussion

In the previous set-up, $B = 0T$ case, the number of ions collected by the detector, under $V_C > 0V$, was of the order of $1 \times 10^{11} \text{ ions/cm}^2$ and only 3% of the



total number of

ions that entered the cone finally reached the detector. In the present set-up under a magnetic field of $125.7mT$ and a positive cone voltage of $4V$, the ion flux at the detector was $1.5 \times 10^{12} \text{ ions/cm}^2$ about fifteen times higher than that previously obtained. The presence of the magnetic field increased the ratio of the number of ions detected to the ions that entered the cone to 38%. This behavior has also been observed in magnetic ducts [5.5].

Let us estimate the electron and ion Larmor radius for the magnetic field strengths used. From eq.(2.9) the Larmor radius is $r_L = v_{\perp} / \omega_c$. Where the cyclotron

frequency is given by eq.(2.8). In the case of electrons the cyclotron frequency equals $8.8 \times 10^9 \text{ sec}^{-1}$ and $2.2 \times 10^{10} \text{ sec}^{-1}$, for $B = 50 \text{ mT}$ and 125.7 mT , respectively. For the ions the corresponding values are $1.7 \times 10^5 \text{ sec}^{-1}$ and $4.3 \times 10^5 \text{ sec}^{-1}$ for the lowest and the highest magnetic field strengths. Assuming electrons of 2 eV , the Larmor radius in the 50 mT field is $116 \mu\text{m}$ and becomes $47 \mu\text{m}$ in the 125.7 mT field. Both values for the electron Larmor radius are much smaller than the cone radius. For a 150 eV silicon ion, on the other hand, entering the magnetic field lines at 10° , the Larmor radius is 32 mm for the 50 mT field and 13 mm for the 125.7 mT field. These values are higher or, in the case of the highest magnetic field, of the order of the cone radius.

Using the last set up the maximum ion dose measured was of the order of $1.5 \times 10^{12} \text{ ions} / \text{cm}^2$. This means that the time required to perform an implantation with a typical dose of $1 \times 10^{16} \text{ cm}^{-2}$, under a laser repetition rate of 10 Hz , is about 11 min . This time can be further decreased if an inhomogeneous magnetic field is employed, to provide focusing of the ions at the detector [2.1]. This can be achieved if the density of the wire loops (number of loops/unit length) that form the coil, is constantly increasing, towards the detector region, resulting in increased magnetic field line density there. To additional increase of the ion flux at the detector can lead the use of a second magnetic field, a focusing field, located close to the ablating target. This will provide the possibility of controlling the expansion of the plume and thus “injecting” into the cone the major part of the plasma that can lead to increased ion flux at the detector. “Focused injection” of plasma has been used in vacuum arcs by S. Anders et. al. [5.6] and it was found to maximize the output, by a factor of $1.4 - 2$, with relatively low focusing field strengths, of the order of $20 - 40 \text{ mT}$, while higher focusing field strengths resulted in decreasing output to below the $B = 0 \text{ T}$ value. The maximum output was found to depend on both fields. Specifically, at a high guiding field strength, a low focusing field strength was required, while a high focusing field strength maximized the output at low guiding field strength. A final modification that can be made, for higher ion yield, is to increase the ionization fraction of the plume. Choosing a laser with the proper wavelength and pulse duration can lead to increased plasma ionization. This modification will not create problems with the performance of the cone, since the set-up used did not impose any restrictions neither to the laser used nor to the target material being ablated.

D. Conclusion

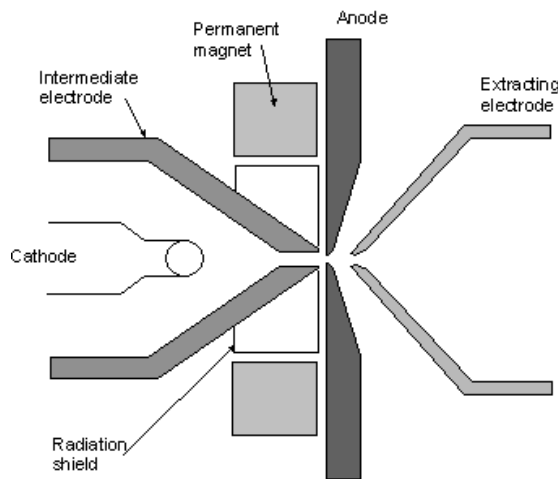
As verified by our experiments, moderate magnetic fields can guide the plasma very effectively even without electrostatic reflection. This is due to an interesting double feedback effect. The electrostatic attraction between the positive and the negative space charge drags the electrons along the forward directed motion of the ion matrix instead of their purely random thermal motion in stationary plasmas. The magnetic field guides charges, of both polarities, along its field lines but this guiding is tighter for the electrons with much lower mass. The tight guiding of the electron cloud is followed by the ion matrix thanks to the electrostatic binding between the ion and the electron space charges.

APPENDIX

A.1 Duoplasmatron

The duoplasmatron [3.2, 3.3], shown in Fig.

A. 1 consists of a cathode, an intermediate electrode, an anode and the extracting electrode, as already mentioned in ch.2. An arc is developed between the cathode and the anode and the



presence of the intermediate electrode and magnetic field serve to concentrate the plasma at a region

near the intermediate electrode, creating a plasma sphere. A double sheath bounds this plasma sphere. Electrons emitted from the cathode are accelerated across the double sheath to form a beam in the

anode volume that is focused electrostatically by the sheath and magnetically by the shaped field.

This beam is primarily responsible for the ionization and the arc forms around it.

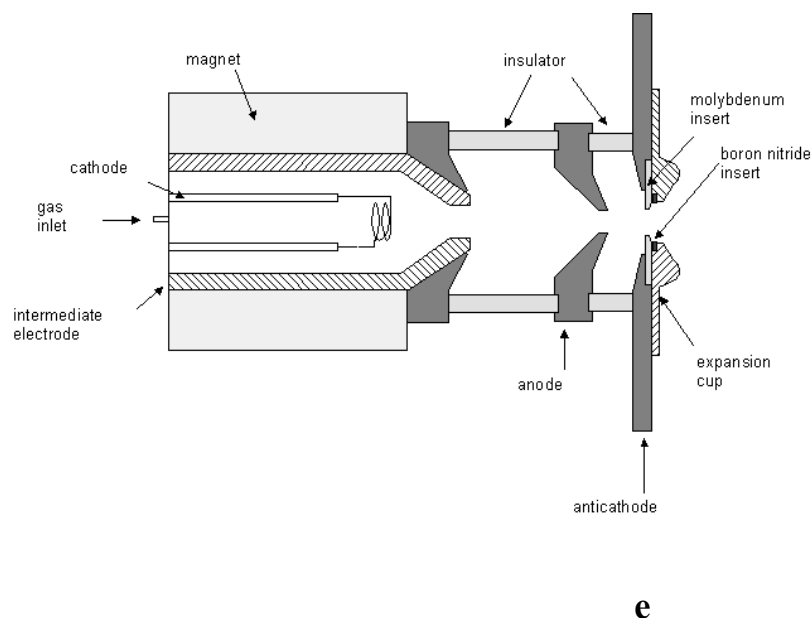
Fig. A. 1: Duoplasmatron type ion source with a permanent magnet. (after [3.2]).

The ions are extracted through a small aperture in the anode. The high density at the anode creates problems at the extraction and the following ion optics, so an expansion cup is often used after the extraction electrode, to reduce the divergence angle of the extracted beam.

A.2 Duopigatron

A typical design for the duopigatron [3.3, 3.4] is shown in Fig. A. 2. Due to the magnetic field electrons emitted from the cathode move in helical paths towards the anticathode. By increasing the magnetic field intensity, the Larmor radius can be decreased and can be made much smaller than the anode's radius. This restricts the electrons from reaching the anode. Moreover the electrons cannot reach the anticathode since when traversing the plasma they lose energy. In this way they become trapped between the cathode and the anticathode. Finally when they have lost most of their energy they diffuse towards the anode. The oscillation of the electrons between the cathode and the anticathode increases the ionization efficiency and consequently the extracted current, which can reach values of the order of $300mA$ to $1A$.

Fig. A. 2: *The duopigatron (after [3.4]).*

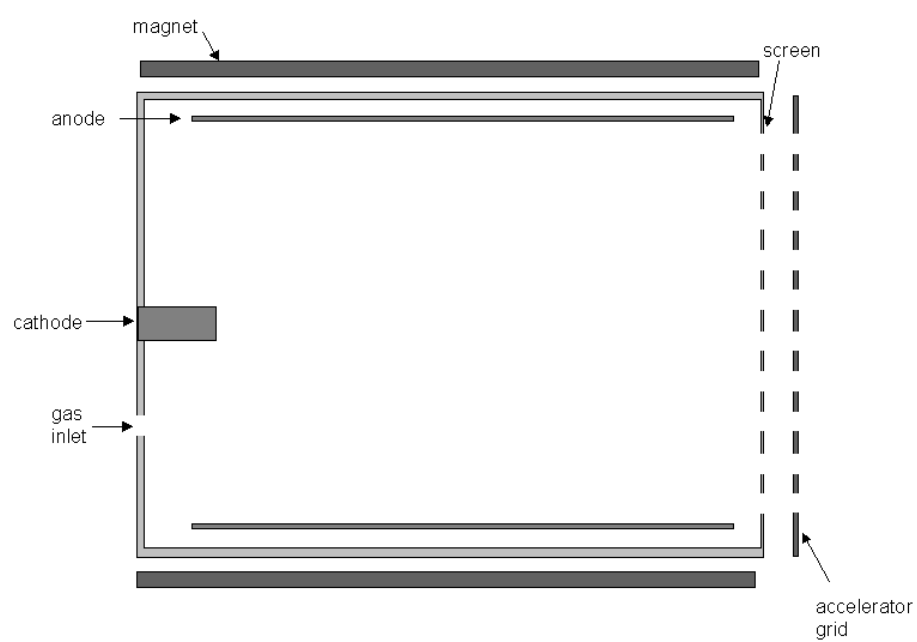


A.3 Hot cathode electron impact ion source

As shown in Fig. A. 3 the ionization chamber is a cylinder with the cathode located near the axis at the one end of the cylinder and the anode forming the cylindrical outer boundary to the discharge region [3.1, 3.5]. Ions are extracted from

the sheath formed at a multi aperture screen electrode located at the other end of the cylinder, by applying a high voltage to the acceleration electrode. To match the ion production to the current capacity of the ion optics the source is normally operated in low pressure. A magnetic field is used to prevent electrons from going directly to the anode. Instead they follow helical trajectories around the magnetic field lines ionizing more efficiently the gas atoms. As a result the plasma, which fills the entire chamber, is continuously supplied with electrons and ions.

Fig. A. 3: *Electron impact-type ion source (after [3.1]).*



References

Introduction

[I.1] P. Normand, D. Tsoukalas, E. Kapetanakis, J. A. Van Den Berg, D. G. Armour and J. Stoemenos, *Micr. Eng.* **36**, 79 (1997).

[I.2] P. Normand, D. Tsoukalas, E. Kapetanakis, J. A. Van Den Berg, D. G. Armour, J. Stoemenos and C. Vieu , *Electrochem. Sol. St. Lett.* **1**, 88 (1998).

[I.3] S. Tiwary, F. Rana, H. Hanafi, A. Hartstein, E. F. Crabbé and K. Chan, *Appl. Phys. Lett.* **68**, 1377 (1996).

[I.4] H. Ohno, *Science* **281**, 951 (1998).

Chapter 1

- [1.1] J. F. Friichtenicht, Rev. Sci. Instrum. **45**, 51 (1974).
- [1.2] D. B. Chrisey and G. K. Hubler, *Pulsed Laser Deposition of Thin Films*, John Willey and Sons, 1994.
- [1.3] D. Bäuerle, *Laser Processing and Chemistry*, Springer, 2000.
- [1.4] B. Qi, R. M. Gilgenbach, Y. Y. Lau, M. D. Johnston, J. Lian, L. M. Wang, G. L. Doll and A. Lazarides, Appl. Phys. Lett. **78**, 3785 (2001).
- [1.5] J. Hasegawa, M. Yoshida, Y. Oguri, M. Ogawa, M. Nakajima and K. Horioka, Nucl. Instr. Meth. Phys. Res. B **161-163**, 1104 (2000).
- [1.6] M. Yoshida, J. Hasegawa, S. Fukata, Y. Oguri, M. Ogawa, M. Nakajima, K. Horioka, S. Maebara and M. Shiho, Nucl. Instr. Meth. Phys. Res. A **464**, 582 (2001).
- [1.7] Yu. K. Al'tudov, Yu. A. Bykovskii and V. N. Nevolin, Sov. Phys. Tech. Phys. **25**, 105 (1980).

- [1.8] R. K. Singh and J. Narayan, Phys. Rev. B **41**, 8843 (1990).
- [1.9] S. Amoroso, R. Bruzzese, N. Spinelli and R. Velotta, J. Phys. B **32**, R131 (1999).
- [1.10] B. N. Chichkov, C. Momma, S. Nolte, F. von Alvensleben and A. Tünnermann, Appl. Phys. A **63**, 109 (1996).
- [1.11] R. K. Singh, O. W. Holland and J. Narayan, J. Appl. Phys. **68**, 233 (1990).
- [1.12] S. Fahler and H. U. Krebs, Appl. Surf. Sci. **96-98**, 61 (1996).
- [1.13] X. Mao and R. E. Russo, Appl. Phys. A **64**, 1 (1997).
- [1.14] G. B. Shinn, F. Steigerwald, H. Stiegler, R. Sauerbrey, F. K. Tittel and W. L. Wilson, Jr., J. Vac. Sci. Technol. B **4**, 1273 (1986).
- [1.15] R. Jordan, D. Cole, J. G. Lunney, K. Mackay and D. Givord, Appl. Surf. Sci. **86**, 24 (1995).
- [1.16] J. G. Lunney and R. Jordan, Appl. Surf. Sci. **127-129**, 941 (1998).

- [1.17] S. Amoruso, Appl. Surf. Sci. **138-139**, 292 (1999).
- [1.18] D. I. Rosen, J. Mitteldorf, G. Kothandaraman, A. N. Pirri and E. R. Pugh, J. Appl. Phys. **53**, 3190 (1982).
- [1.19] S. Amoruso, Appl. Phys. A **69**, 323 (1999).
- [1.20] R. Kelly and R. W. Dreyfus, Surf. Sci. **198**, 263 (1988).
- [1.21] A. Miotello, A. Peterlongo and R. Kelly, Nucl. Instr. Meth. Phys. Res. B **101**, 148 (1995).
- [1.22] B. R. Finke and G. Simon, J. Phys. D **23**, 67 (1990).
- [1.23] J. C. S. Kools, T. S. Baller, S. T. De Zwart and J. Dieleman, J. Appl. Phys. **71**, 4547 (1992).
- [1.24] D. Sibold, H. M. Urbassek, Phys. Rev. A **43**, 6722 (1991).
- [1.25] I. NoorBatcha, R. Lucchese and Y. Zeiri, Phys. Rev. B **36**, 4978 (1987).
- [1.26] F. Antoni, F. Fuchs and E. Fogarassy, Appl. Surf. Sci. **96-98**, 50 (1996).

- [1.27] A. Mele, A. Giardini Guidoni, R. Kelly, A. Miotello, S. Orlando and R. Teghil, *Appl. Surf. Sci.* **96-98**, 102 (1996).
- [1.28] C. Cali, F. La Rosa, G. Targia and D Robba, *J. Appl. Phys.* **78**, 6265 (1995).
- [1.29] ch.7 of ref [1.2].
- [1.30] T. N. Hansen, J. Schou and J. G. Lunney, *Appl. Phys. A.* **69**, S601 (1999).
- [1.31] J. F. Friichtenicht, N. G. Utterback and J. R. Valles, *Rev. Sci. Instrum.* **47**, 1489 (1976).
- [1.32] P. E. Dyer, *Appl. Phys. Lett.* **55**, 1630 (1989).
- [1.33] R. J. von Gutfeld and R. W. Dreyfus, *Appl. Phys. Lett.* **54**, 1212 (1989).
- [1.34] J. Dieleman, E. van de Riet and J. C. S. Kools, *Jpn. J. Appl. Phys.* **31**, 1964 (1992).
- [1.35] R. P. van Ingen, *J. Appl. Phys.* **76**, 8055 (1994).

- [1.36] V. N. Anisimov, V. Yu. Baranov, V. G. Grishina, O. N. Derkach, A. Yu. Sebrant and M. A. Stepanova, *Appl. Phys. Lett.* **67**, 2922 (1995).
- [1.37] R. P. van Ingen, *J. Appl. Phys.* **76**, 8065 (1994).
- [1.38] S. Amoroso, M. Armenante, V. Berardi, R. Bruzzese and N. Spinelli *Appl. Phys. A* **65**, 265 (1997).
- [1.39] Y. Franghiadakis, C. Fotakis and P. Tzanetakis, *Appl. Phys. A* **68**, 1 (1999).
- [1.40] S. Metev, M. Ozegowski, G. Sepold and S. Burmester, *Appl. Sur. Sci.* **96-98**, 122 (1996).
- [1.41] R. M. Gilgenbach and P. L. G. Ventzek, *Appl. Phys. Lett.* **58**, 1597 (1991).
- [1.42] J. M. Hedron, C. M. O. Mahony, T. Morrow and W. G. Graham, *J. Appl. Phys.* **81**, 2131 (1997).
- [1.43] Y. Franghiadakis, C. Fotakis and P. Tzanetakis, *J. Appl. Phys.* **84**, 1090 (1998).

Chapter 2

[2.1] Francis F. Chen *Introduction to Plasma Physics and Controlled Fusion, Vol.1: Plasma Physics 2nd edition*, Plenum Press, 1984.

[2.2] M. Mitchner, Charles H. Kruger, Jr *Partially Ionized Gases*, John Willey and Sons, 1973.

[2.3] I. H. Hutchinson *Principles of Plasma Diagnostics*, Cambridge University Press, 1987.

Chapter 3

[3.1] R. G. Wilson and G. R. Brewer *Ion Beams with Applications to Ion Implantation*, Robert E. Krieger publishing company, 1979.

[3.2] L.Vályi *Atom and Ion Sources*, John Willey and Sons, 1977.

[3.3] T. S.Green, Rep. Prog. Phys. **37**, 1257 (1974).

[3.4] F. M. Bacon, R. W. Bickes, Jr. and J. B. O'Hagan, Rev. Sci. Instrum. **49**, 435 (1978).

- [3.5] H. R. Kaufman, J. J. Cuomo and J. M. E. Harpe, J. Vac. Sci. Tech. **21**, 725 (1982).
- [3.6] I. G. Brown, J. E. Gavin and R. A. MacGill, Appl. Phys. Lett. **47**, 358 (1985).
- [3.7] M. J. Kofoed, G. M. Braans and P. Zieske, Rev. Sci. Instrum. **36**, 1415 (1965).
- [3.8] Yu. K. Al'tudov, T. A. Basova, Yu. A. Bykovskii, V. G. Degtyarev, Yu. N. Kolosov, I. D. Laptev and V. N. Nevolin, Sov. Phys. Tech. Phys. **24**, 1077 (1979).
- [3.9] J. R. Conrad, J. L. Radtke, R. A. Dodd, F. J. Worzuala and N. C. Tran, J. Appl. Phys. **62**, 4591 (1987).
- [3.10] P. K. Chu, S. Qin, C. Chan, N. W. Cheung and L. A. Larson, Mat. Sci. Eng. Rep. **R17**, 207 (1996).
- [3.11] J. R. Conrad, J. Appl. Phys. **62**, 777 (1987).
- [3.12] M. A. Lieberman, J. Appl. Phys. **66**, 2926 (1989).

[3.13] J. T. Scheuer, M. Shamim and J. R. Conrad
J. Appl. Phys. **67**, 1241 (1990).

[3.14] B. Qi, Y. Y. Lau and R. M. Gilgenbach,
Appl. Phys. Lett. **78**, 706 (2001).

Chapter 4

[4.1] A. Belkind and F. Jansen, Surf. Coat. Tech.
99, 52 (1998).

[4.2] R. del Coso, A. Perea, R. Serna, J. A. Chaos,
J. Gonzalo and J. Solis, Appl. Phys. A **69**, S553
(1999).

[4.3] A. A. Voevodin and S. J. P. Laube, Surf. Coat. Tech. **76-77**, 670 (1995).

[4.4] N. M. Bulgakova, A. V. Bulgakov and O. F. Bobrenok, Phys. Rev. E **62**, 5624
(2000).

[4.5] H. D. Hagstrum, Phys. Rev. **89**, 244 (1953).

[4.6] S. Shinohara, H. Tsuji, T. Yoshinaka and Y. Kawai, Surf. Coat. Tech. **112**, 20
(1999).

Chapter 5

[5.1] A. Anders, Surf. Coat. Tech. **93**, 158 (1997).

[5.2] T. Zhang, B. Y. Tang, Q. C. Chen, Z. M Zeng, P. K. Chu, M. M. M. Bilek and I.
G. Brown, Rev. Sci. Instrum. **70**, 3329 (1999).

[5.3] T. Zhang, Z. M Zeng, X. B. Tian, B. Y. Tang, P. K. Chu, I. G. Brown and H. X.
Zhang, J. Vac. Sci. Technol. **17**, 3074 (1999).

- [5.4] R. Jordan, D. Cole and J. G. Lunney, Appl. Surf. Sci. **109/110**, 403 (1997).
- [5.5] A. Anders, S. Anders and I. G. Brown, J. Appl. Phys. **75**, 4900 (1994).
- [5.6] S. Anders, A. Anders and I. Brown, J. Appl. Phys. **75**, 4895 (1994).

